Open Research Online

The Open University's repository of research publications
and other research outputs

A deep ATCA 20cm radio survey of the AKARI Deep Field South near the South Ecliptic Pole

Journal Item

For guidance on citations see FAQs.

oro.open.ac.uk

A deep ATCA 20cm radio survey of the AKARI Deep Field South near the South Ecliptic Pole

Glenn J. White[1,2], Bunyo Hatsukade[3], Chris Pearson[2,1,6],Toshinobu Takagi[4],
Chris Sedgwick[1], Shuji Matsuura[4], Hideo Matsuhara[4], Stephen Serjeant[1],
Takao Nakagawa[4], Hyung Mok Lee[5], Shinki Oyabu[13], Woong-Seob Jeong[10],
Mai Shirahata[4,12], Kotaro Kohno[7,8], Issei Yamamura[4], Hitoshi Hanami[9],
Tomotsugu Goto[11], Sin'itirou Makiuti[4], David L. Clements[14], Malek, K.[15],
Sophia A. Khan[16]

[1] *Department of Physics and Astronomy, The Open University, Walton Hall, Milton Keynes, MK7 6AA, UK*

[2] *RAL Space, STFC Rutherford Appleton Laboratory, Chilton, Didcot, Oxfordshire, OX11 0QX, UK*

[3] *Department of Astronomy, Kyoto University, Kyoto 606-8502, Japan*

[4] *Institute of Space and Astronautical Science, JAXA, 3-1-1 Yoshinodai, Chuo, Sagamihara, Kanagawa 252-5210, Japan,*

[5] *Astronomy Program, Department of Physics and Astronomy, Seoul National, University, Seoul 151-747, Korea*

[6] *Institute for Space Imaging Science, University of Lethbridge,, Lethbridge, Alberta T1K 3M4, Canada*

[7] *Institute of Astronomy, the University of Tokyo, 2-21-1 Osawa, Mitaka, Tokyo 181-0015, Japan*

[8] *Research Center for the Early Universe, University of Tokyo, 7-3-1 Hongo, Bunkyo, Tokyo 113-0033, Japan*

[9] *Physics Section, Faculty of Humanities and Social Sciences, Iwate University, Morioka 020-8550, Japan*

[10] *KASI, 61-1, Whaam-dong, Yuseong-gu, Deajeon, 305-348, South Korea*

[11] *Institute for Astronomy, University of Hawaii, 2680 Woodlawn Drive, Honolulu, HI, 96822, USA*

[12] *Subaru Telescope, National Astronomical Observatory of Japan, 650 North A'ohoku Place, Hilo, HI, 96720, U.S.A*

[13] *Graduate School of Science, Nagoya University, Furo-cho, Chikusa-ku, Nagoya, Aichi 464-8602, Japan*

[14] *Imperial College, London, Blackett Lab, Prince Consort Road, London SW7 2AZ, UK*

[15] *Center for Theoretical Physics of the Polish Academy of Sciences, Al. Lotnikow 32/46, 02-668 Warsaw, Poland*

[16] *Shanghai Key Lab for Astrophysics, Shanghai Normal University, Shanghai 200234, China*

31 October 2012

ABSTRACT

The results of a deep radio survey at 20 cm wavelength are reported for a region con-

taining the AKARI Deep Field South (ADF-S) near the South Ecliptic Pole (SEP), using the Australia Telescope Compact Array telescope, ATCA. The survey (hereafter referred to as the ATCA-ADFS survey) has 1σ detection limits ranging from 18.7–50 μJy beam^{-1} over an area of $\sim$ 1.1 degree^2, and $\sim$ 2.5 degree^2 to lower sensitivity. The observations, data reduction and source count analysis are presented, along with a description of the overall scientific objectives, and a catalogue containing 530 radio sources detected with a resolution of 6.2″ × 4.9″. The derived differential source counts show a pronounced excess of sources fainter than $\sim$ 1 mJy, consistent with an emerging population of star forming galaxies. Cross-correlating the radio with AKARI sources and archival data we find 95 cross matches, with most galaxies having optical R-magnitudes in the range 18-24 magnitudes, similar to that found in other optical deep field identifications, and 52 components lying within 1″ of a radio position in at least one further catalogue (either IR or optical). We have reported redshifts for a sub-sample of our catalogue finding that they vary between galaxies in the local universe to those having redshifts of up to 0.825. Associating the radio sources with the Spitzer catalogue at 24 μm, we find 173 matches within one Spitzer pixel, of which a small sample of the identifications are clearly radio loud compared to the bulk of the galaxies. The radio luminosity plot and a colour-colour analysis suggest that the majority of the radio sources are in fact luminous star forming galaxies, rather than radio-loud AGN. There are additionally five cross matches between ASTE or BLAST submillimetre galaxies and radio sources from this survey, two of which are also detected at 90 μm, and 41 cross-matches with submillimetre sources detected in the *Herschel* HerMES survey Public Data release.

radio continuum: galaxies; surveys

1   INTRODUCTION

A fundamental challenge in contemporary astrophysics is to understand how the galaxies have evolved to their current form. To address this issue, wide area surveys are required to accumulate large statistical samples of galaxies. To study this question, the Japanese AKARI infrared satellite (Murakami et al. 2007) carried out two deep infrared legacy surveys close to the North and South Ecliptic Poles (Matsuhara et al. 2006, Matsuura et al. 2011), which are notable because their sight-lines to the distant Universe have the advantages of low extinction and correspondingly small Hydrogen column densities. To support the two AKARI Deep Fields, sensitive radio surveys have been made of both ecliptic pole regions to study and compare the global properties of the extragalactic source populations (White et al. 2009, White et al. 2010a [hereafter 'Paper 1']). In the

present paper the results are reported of a sensitive radio survey at 1.4 GHz using the Australia Telescope Compact Array (ATCA) of a region that includes both the ADF-S field (Matsuhara et al. 2006, Wada et al. 2008, Shirahata et al. 2009, White et al. 2009, Matsuura et al. 2009, 2011), as well as a more extended region around it. The ADF-S is the focus of a major multi-wavelength observing campaign conducted across the entire spectral region. The combination of these far-infrared data and the depth of the radio observations will allow unique studies of a wide range of topics including the redshift evolution of the luminosity function of radio sources, the clustering environment of radio galaxies, the nature of obscured radio-loud Active Galactic Nuclei (AGN), and the radio/far-infrared correlation for distant galaxies.

2 MULTI-WAVELENGTH OBSERVATIONS

The AKARI ADF-S field is a region located close to the South Ecliptic Pole (Matsuura et al. 2009, 2011) with a very low cirrus level ≤ 0.5 MJy sr^{-1} (Schlegel et al. 1998, Bracco et al. 2011), and correspondingly low Hydrogen column density $\sim 5{\times}10^{19}$ cm^{-2}. This field is similar to the well known Lockman Hole and Chandra Deep-Field South regions, and has half of the cirrus emission of the well studied COSMOS field at 24μm. The ADF-S field is therefore one of the best 'cosmological windows' through which to study the distant Universe (Malek et al. 2009, Matsuura et al. 2011, Hajian et al. 2012), and is now of high priority for astronomers to build ancillary data sets that can be compared with the AKARI data, and to prepare lead on to the next set of deep cosmological surveys, such as those that will be provided by *Herschel* (Pilbratt et al. 2010) and SPICA (Eales et al. 2009, Swinyard et al. 2009).

The AKARI ADF-S survey was primarily made in the far-infrared at wavelengths of 65, 90, 140, 160 μm over a 12 deg^2 area with the AKARI Far-Infrared Surveyor (FIS) instrument (Kawada et al. 2007), with shallower mid-infrared coverage at 9, 18μm using the AKARI Infrared Camera (IRC) instrument (Onaka et al. 2007). In addition to the wide survey, deeper mid-infrared pointed observations, using the IRC, covering ~ 0.8 deg^2 and reaching 5σ sensitivities of 16, 16, 74, 132, 280 and 580 μJy at 3.2, 4.6, 7, 11, 15, 24 μm were also carried out. At other wavelengths, the region has recently been mapped by Spitzer's Multi-band imaging photometer (MIPS) at 24 and 70 μm (Scott et al. 2010, Clements et al. 2011); by the Balloon-borne Large Aperture Submil-limeter Telescope (BLAST) at 250, 350 and 500 μm (Valiante et al. 2010), the latter revealing $\sim$200 sub-millimetre galaxies over an 8.5 deg^2 field; and in the ground-based submillimetre band by Hatsukade et al. (2011) revealing 198 potential sub-millimetre galaxies in an $\sim$0.25 square de-

Table 1. Summary of ancillary observations available for the ATCA-ADFS deep field

Wavelength (1)	Telescope (2)	Area (3)	Beam size (4)	Depth (5)
FUV, NUV	GALEX	Central 1 degree^2	6″	25.5-26.5 mag (AB)
R	CTIO MOSAIC-II	7.2 degree^2	1″	R 25 mag
U, B, V, I	CTIO / MOSAIC	Central 1 degree^2	1″	U 25, B 26, V 26, I 25 mag
3-24 μm (6 bands)	AKARI / IRC	Central 0.8 degree^2	4.2 - 5.5″	10 μJy @3.5μm 300uJy @15m
24 μm & 70 μm	*Spitzer*-MIPS	11 degree^2	6″ -18″	200 μJy @24μm 20 mJy @70μm
65 μm, 90 μm, 140 μm, 160 μm	AKARI / FIS	12 degree^2	37″ $-$ 50″	30mJy (3σ) @90μm
110-500 μm	*Herschel* (HerMES GT)	7 degree^2	8″ $-$ 36″	30 mJy (5σ)
250 μm, 350 μm, 500 μm	BLAST	9 degree^2	36″ $-$ 60″	45mJy (3σ) all bands
870 μm	APEX / LABOCA	Central 20′×20′	19″	6 mJy (3σ)
1.1 mm	ASTE / AzTEC	Central 0.25 degree^2	30″	1.2-2.4 mJy (3σ)
20 cm	ATCA	Central 1 degree^2	10″	17 μJy
Spectroscopy	AAT AAOmega	Central 3.14 degree^2	-	R~21 mag
Spectroscopy	IMACS Magellan	Central 0.2 degree^2	-	I~22 mag

gree area. The ancillary data sets summarised in Table 1 will be used in calibration of the radio positional reference frame, and for cross-identifications later in this paper. The AKARI sensitivity limits correspond approximately to being able to detect starburst galaxies and AGN with a luminosity of 10^{12} $L_\odot$ at $z = 0.5$, or ultraluminous infrared galaxies (ULIRGS) with luminosities 10^{12-13} $L_\odot$ at $z = 1$–2 respectively. Note that the ADF-S has also been observed by the *Herschel* Space Observatory (HSO) (Pilbratt et al. 2010) as part of the Herschel Multi-tiered Extragalactic Survey (HerMES) guaranteed time key program (Oliver et al. 2010).

Optical, radio, X-ray and infrared surveys provide essential support to the interpretation of deep extragalactic radio surveys. The ADF-S has been the focus of recent multi-wavelength survey coverage by our team, with optical imaging with the CTIO 4m telescope (MOSIAC-II detector) to an R-band sensitivity of 25 magnitudes, and at near-IR wavelengths to K ~18.5 magnitudes with the IRSF/SIRIUS instrument already completed. To support the ADF-S and ATCA surveys, we have separately obtained wide field imaging in the optical and near-IR at ESO (using WFI and SOFI), at the AAT (using WFI and IRIS2), for fields of 0.5 - 1 square degree, and spectroscopic observations using AAOmega on the AAT (Sedgwick et al. 2009, 2011).

3 RADIO OBSERVATIONS

3.1 ATCA observations

The radio observations were collected over a 13 day period in July 2007 using the ATCA operated at 1.344 and 1.432 GHz. The total integration time for the 2007 observations was 120 h, spread between 26 overlapping pointing positions to maximise the uv coverage and to mitigate the effects

of sidelobes from nearby radio-bright sources. Two of the pointing positions were observed on each night, by taking one five minute integration at each of the two target fields, followed by a two minute integration on the nearby secondary calibrator 0407-658. This cycle was repeated for the different pointing positions, which were observed over ~10 hour tracks each night, giving similar uv-coverage for each target field. The amplitude scaling was bootstrapped from the primary calibrator PKS 1934-638, which was observed for 10 min at the start of each observing night, and which was assumed to have a flux density of 15.012 Jy at 1.344 GHz and 14.838 Jy at 1.432 GHz respectively. The 2007 data were augmented with a further deep observation made in December 2008 over 5 nights toward a single pointing position at the ADF-S, which lay just off centre of the larger ATCA-ADFS field reported here. This added a further 50 hours of integration time. The data were processed in exactly the same way as that from the 2007 observing sessions.

3.2   Calibration

In the following sub-sections the calibration and data reduction methodology are presented. Since much of this is in common with our recent North Ecliptic Pole (NEP) radio survey with the Westerbork Synthesis Radio Telescope (WSRT) telescope discussed in Paper 1, we will not repeat the detailed discussion of this earlier paper, but instead just focus on those parts of the calibration methodology that differed from Paper 1.

   The data were calibrated using the ATNF data reduction package *MIRIAD* (Sault et al. 1995) using standard procedures. The raw data come in RPFITS format, and were converted into the native *MIRIAD* format using ATLOD. ATLOD discards every other frequency channel (since they are not independent from one another, hence no information is lost), and additionally flagged out one channel in the higher frequency sideband which contained a multiple of 128 MHz, and thus was affected by self-interference at the ATCA. Channels at either end of the sidebands where the sensitivity dropped significantly were also not used. The resulting data set contained two sidebands, with 13 and 12 channels respectively, each 8 MHz wide, which resulted in a total bandwidth of 200 MHz. The lower frequency sideband was mostly free of RFI and required little editing apart from flagging of bad data. However, the higher frequency sideband suffered from occasional local RF interference, and the affected data were flagged out using the ATNF automated noise flagger PIEFLAG (Middelberg 2006), which eliminated virtually all of the RFI-affected data which would have been flagged in a visual inspection. A visual inspection of the visibilities after using PIEFLAG, led to the removal of a few other small sections of RFI-affected data. In total, approxi-

mately 3% and 15% of the data were flagged out in the lower and higher bands respectively. Phase and amplitude fluctuations throughout the observing run were then corrected using the interleaved secondary calibrator data, and the amplitudes were scaled by bootstrapping to the primary calibrator. The data were then split by pointing position and each field was individually imaged, before mosaicing to form a master image, sensitivity and noise maps.

3.3   Imaging

The data for each of the target pointings were imaged separately using uniform weighting and gridded to a pixel size of 2.0″ to a common reference frame (to minimise geometrical issues in the mosaicing process). The twenty-five 8 MHz wide frequency channels across the ATCA passband were reduced using *MIRIAD*'s implementation of multi-frequency clean, MFCLEAN, which accounts for variation in the spectral index of the calibration sources across the observed bandwidth. After a first iteration of MFCLEAN, model components with flux densities ≥ 1 mJy beam^{-1} were used to phase self-calibrate, and to correct residual phase errors. The data were then re-imaged and CLEANED for 5000 iterations, at which point the sidelobes of strong sources were generally found to be comparable with the thermal noise, except for a few cases adjacent to bright sources. The individual pointings were then mosaiced together using the *MIRIAD* task LINMOS, which additionally divides each image by a model of the primary beam attenuation, and uses a weighted average of positions contained in more than one pointing. As a result, pixels at the mosaic edges have a higher noise level. Regions beyond the point where the primary beam response drops below 50% (this occurs at a radius of 35.06′ from the centre of a pointing) were blanked, which resulted in a total survey area of 1.04 deg.^{2} (to the limit of the half power beam width at the edges of the master image). The synthesised beam size in the final mosaiced image was 6.2″ × 4.9″ at a position angle of 0 degrees. The sensitivity varies across the image due to primary beam attenuation and the mosaicing strategy as shown in Figure 1, although the noise level achieved across the map is ~35% higher than expected for a thermal noise limited survey, which is due to difficulties in removing the sidelobes of strong sources at the edge of the survey field. This is a well known situation that has previously been seen both for ATCA and WSRT radio surveys, and probably results from both the non-circularity of the telescope beam, and small movements of the primary beam on the sky caused by random single dish pointing errors (i.e. due to wind/thermal loading) that cause the intensity of bright sources near the edge of the primary
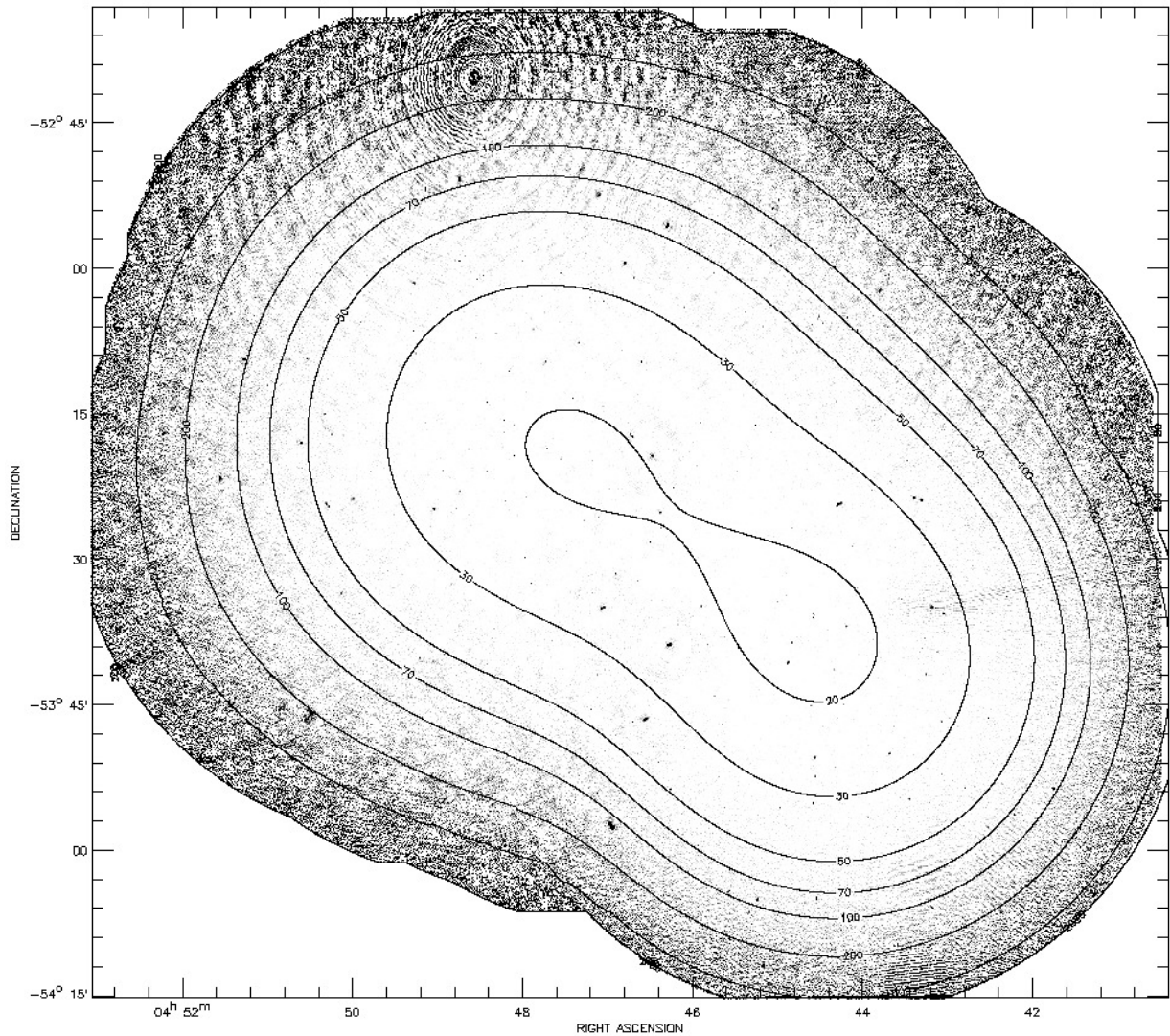
Figure 1. The central area of the ATCA 20 cm map, corrected for the primary beam of the antenna. The contours show the rms noise levels in μJy beam^{-1} estimated locally from the noise map by binning the data into 40×40 pixel regions.

beam to vary significantly during an integration, making it difficult to efficiently CLEAN those areas.

4 SOURCE COMPONENT CATALOGUE

The mosaiced region achieves wide-field coverage and good sensitivity at the price of having an unavoidably non-uniform noise distribution. Statistical characterisation of the completeness of detection at various flux levels is therefore a complex procedure that requires accounting for the observing time, mosaic overlap, and primary beam attenuation. Our source detection was made using locally determined noise levels derived from the noise map (Figure 2) - an approach that has already been used in other studies to improve the efficacy of their source detection catalogues (e.g.
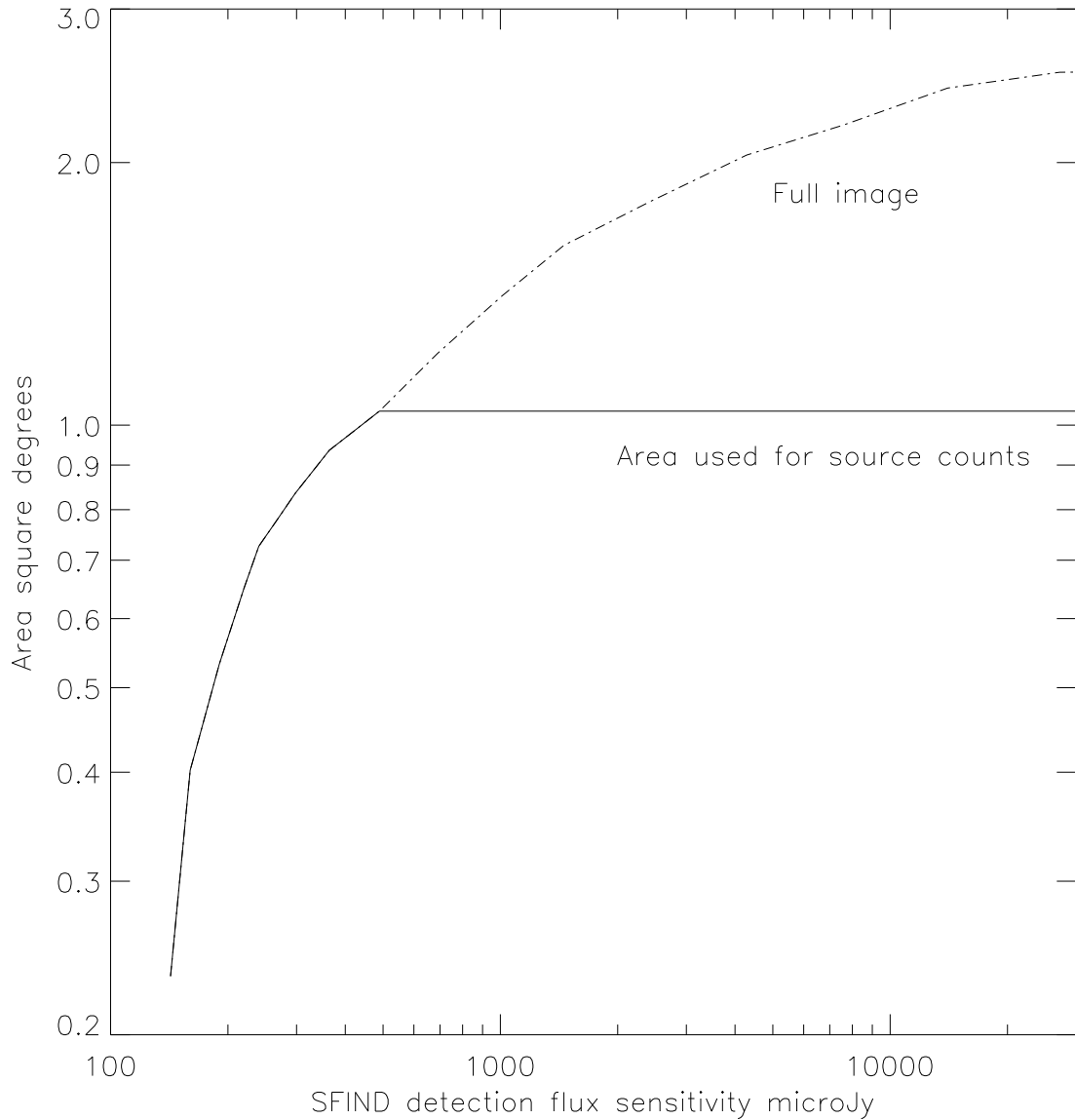
Figure 2. The horizontal axis shows the *SFIND* detection threshold as a function of areal coverage. The area used for the differential source count estimation in Section 5 is shown as a solid line, and has a maximum value of 1.04 degree^2, whereas that of the full image (whose radio components are listed in Table 2) is indicated by the dot-dash line and has a maximum value of 2.55 degree^2.

Hopkins et al. 1998, Morganti et al. 2004, Paper 1, and the associated NEP component catalogue presented in White et al. 2010b).

The component catalogue in this paper was built using the *MIRIAD* task *SFIND* in a similar way to that described in Paper 1. However, briefly *SFIND* uses a statistical technique, the false discovery rate (FDR), which assigns a threshold based on an acceptable rate of false detections (Hopkins et al. 2002). For the ATCA-ADFS data the approach of Hopkins et al. (2002) was followed by adopting an FDR value of 2%. The components identified by *SFIND* were visually inspected to remove any obvious mis-identifications (e.g. a few residual sidelobe structures imme-

Table 2. The component catalogue (the full version is available as Supplementary Material in the on-line version of this article). The component parameters listed in the catalog are: (1) a short form running number (components that are believed to be parts of multi-component sources are listed with a † sign next to the running number (for example 47†), with more details about these multi-component sources being presented in Table 3, (2) the component name, referred to in this paper as ATCA-ADFS followed by the RA/Dec encoding (e.g. ATCA-ADFS J045243-533127), (3,4) the component Right Ascension and Declination (J2000) referenced from the self-calibrated reference frame, (5,6) the RA and Dec errors in arc seconds, (7,8) the peak flux density, S_{peak}, and its associated rms error, (9,10) the integrated flux densities, S_{total} and their associated errors, (11, 12, 13) the size along the major and minor axes of the fitted Gaussian component profile and its orientation (the major and minor axes refer to the full width at half maximum component size deconvolved from the synthesised beam, and position angle was measured east of north. Component sizes are shown in columns 11 or 12 only for the cases where $S_{total}/S_{peak} \geq 1.3$, as an indicator of a resolved component. Components where $S_{total}/S_{peak} < 1.3$ were considered to be unresolved, and therefore component sizes are not individually reported for these here. All components were additionally checked visually to mitigate against artefacts that might have slipped through the various checks.

No	Component name	RA h:m:s.s	DEC d:m:s.s	ΔRA ″	ΔDEC ″	S_{peak} mJy beam^{-1}	ΔS_{peak} mJy beam^{-1}	S_{total} mJy	ΔS_{total} mJy	θ_{maj} ″	θ_{min} ″	PA °
(1)	(2)	(3)	(4)	(5)	(6)	(7)	(8)	(9)	(10)	(11)	(12)	(13)
1	ATCA-ADFS J044041-534043	4:40:41.5	-53:40:43.5	0.14	0.03	2.951	0.286	7.392	0.368	12.1	2.7	-84.0
2	ATCA-ADFS J044116-532554	4:41:16.4	-53:25:54.0	0.00	0.00	1.498	0.153	4.427	0.206	8.7	6.6	-48.1
3	ATCA-ADFS J044116-531845	4:41:16.9	-53:18:45.8	0.07	0.31	1.568	0.260	5.310	0.317	13.5	3.5	-9.3
4	ATCA-ADFS J044117-531853	4:41:17.9	-53:18:53.5	0.03	0.02	1.866	0.260	2.632	0.274	6.7		-40.6
5	ATCA-ADFS J044120-533214	4:41:20.1	-53:32:14.9	0.03	0.02	1.603	0.116	5.893	0.137	14.1	4.9	-53.8
6	ATCA-ADFS J044120-531626	4:41:20.7	-53:16:26.3	0.79	0.16	1.626	0.260	6.553	0.359	14.8	5.8	-87.5
7	ATCA-ADFS J044121-531637	4:41:21.9	-53:16:37.9	0.17	0.05	1.966	0.260	7.431	0.361	12.6	6.6	-88.1
8	ATCA-ADFS J044122-534349	4:41:22.0	-53:43:49.1	0.01	0.01	0.686	0.096	1.051	0.100			
9	ATCA-ADFS J044123-534402	4:41:23.8	-53:44:02.8	0.07	0.01	0.932	0.096	2.413	0.121	10.3	4.4	-86.0
10	ATCA-ADFS J044124-531600	4:41:24.1	-53:16:00.1	0.32	0.13	1.677	0.260	4.353	0.340	8.6	5.5	86.1
11	ATCA-ADFS J044141-533707	4:41:41.9	-53:37:07.6	0.00	0.00	6.011	0.116	11.775	0.178	7.5	3.6	-80.4
12	ATCA-ADFS J044145-535304	4:41:45.5	-53:53:04.4	0.00	0.00	11.728	0.187	23.327	0.210	8.7	2.0	59.2
13	ATCA-ADFS J044156-531452	4:41:56.5	-53:14:52.4	0.00	0.01	4.390	0.507	10.187	0.521	9.8	2.5	-38.7
14	ATCA-ADFS J044203-534302	4:42:03.9	-53:43:02.1	0.00	0.00	0.639	0.050	0.726	0.050			
15	ATCA-ADFS J044205-533253	4:42:05.0	-53:32:53.3	0.25	0.02	0.356	0.071	1.363	0.074	20.9		-79.4
16	ATCA-ADFS J044208-535941	4:42:08.4	-53:59:41.2	0.41	0.04	0.584	0.080	0.923	0.095	12.2		-73.9
17	ATCA-ADFS J044212-531047	4:42:12.6	-53:10:47.9	0.01	0.03	1.184	0.190	1.974	0.197	6.6		-18.2
18	ATCA-ADFS J044212-535551	4:42:12.6	-53:55:51.6	0.01	0.01	1.374	0.080	2.291	0.087	7.8		47.6
19	ATCA-ADFS J044212-530209	4:42:13.0	-53:02:09.8	0.04	0.11	2.977	0.399	3.947	0.484	6.6		3.7
20	ATCA-ADFS J044213-530802	4:42:13.6	-53:08:02.5	0.06	0.11	1.166	0.190	2.322	0.216	9.4		-23.0

diately adjacent to the brightest components in the mapped region). Comparison with independent catalogues derived using the *MIRIAD* task *IMSAD* (with a 7 σ clip), and with one derived using *SExtractor* (Bertin & Arnouts 1996) with a locally defined background *rms* were almost identical with the *SFIND* catalogue. Hopkins et al. (1998) show that using *SFIND* in this way provides a very robust estimate of the noise level above which there are almost no spurious positive candidates, with the completeness being robustly set by the choice of FDR, and the locally determined background noise level. An understanding of source confusion, spurious components, sensitivity and completeness are important in any survey that is analysed to its limit, but as this becomes difficult to rigorously establish for mosaiced images with non-uniform noise properties of our mosaic and the fact that some but not all of the components are resolved, it was decided for the source counts analysis in Section 5 to stop the calculation at the very conservative level of 200 μJy, which corresponds to in excess of 10σ signal to noise in the most sensitive parts of the mapped region.

A sample from the final component catalogue is presented in Table 2, and the entire catalogue is included in the electronic on-line version of this paper.
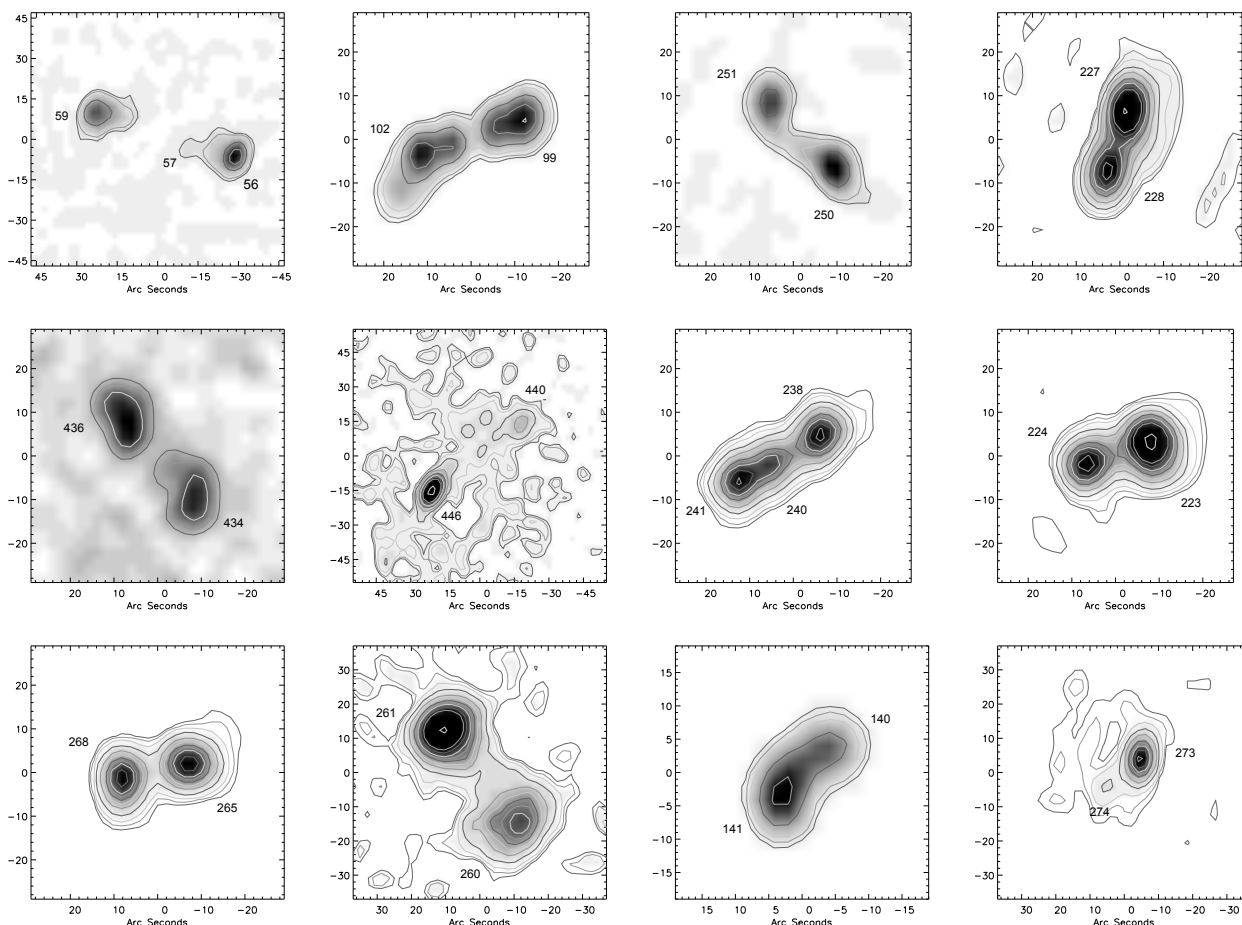
Figure 3. Regions showing complex or extended structure. The vertical scale is Declination. The contours are at 0.0001, 0.0003, 0.0005, 0.001, 0.003, 0.006, 0.012, 0.024, 0.048 and 0.096 Jy beam^{-1} respectively. The Right Ascension/Declination scales can de derived using the component locations in Table 2.

The positional accuracy listed in the Table 2 is relative to the self-calibrated and bootstrapped reference frame described in Section 3. Other effects that bias the positions or sizes of sources in radio surveys have already been presented in Paper 1, to which the reader is referred. An estimate of component dimensions calculated by deconvolving the measured sizes from the synthesised beam is also presented, with Table 2 reporting only those more than double the synthesised beam size.

4.1   Component extraction

In the terminology of this paper, a radio component is described as a region of radio emission represented by a Gaussian shaped object in the map. Close radio doubles are represented by two Gaussians and are deemed to consist of two components, which make up a single source. A selection of radio sources with multiple components is shown in Figure 3.

4.2   Complex sources

Radio sources are often made up of multiple components, as seen in Figure 3. The source counts need to be corrected for the multi-component sorces, so that the fluxes of physically related components are summed together, rather than being treated as separate sources. Magliocchetti et al. (1998) have proposed criteria to identify the double and compact source populations, by plotting the separation of the nearest neighbour of a component against the summed flux of the two components, and selecting components where the ratio of their fluxes, f_1 and f_2 is in the range $0.25 \leq f_1/f_2 \leq 4$. In Figure 4 the sum of the fluxes of nearest neighbours are plotted against their separation.

The dashed line marks the boundary satisfying the separation criterion defined by Magliocchetti et al. (1998):

$$\theta = 100 \left[\frac{S_{\text{total}}(\text{mJy})}{10} \right]^{0.5} \tag{1}$$

where θ is in arc seconds. Therefore 53 radio sources in the present survey (i.e. 10% of the 530 catalogued entries) should be considered to be a part of double or multiple sources according to the Magliocchetti et al. (1998) criterion, and this will be taken account of in the source counts discussed later. These components, and their suggested associations are listed in Table 3.

4.3   Flux density and positional accuracy

The flux density and positional accuracy are presented in Table 2, and the method for calculating the positional accuracy are described in Hopkins et al. (2002), and the intensity scales are derived and fully described in Equations 1–5 of Hopkins et al. (2003). Since the methods for measuring the positional and intensity scale accuracy form part of the methodology of the *SFIND* technique, the reader is referred to the papers presenting this technique, rather than repeating them here. However, to check the positional accuracy, the ATCA data were cross correlated against the SUMSS survey (Mauch et al. 2003), where 8 of the bright ATCA sources were found to be within 10″ of a SUMSS source (the SUMSS half-power beam width is 45″ × 57″). After eliminating three components which are resolved and appear as double radio sources in the ATCA data, the average offset between the positions in the two catalogues (ATCA-SUMSS) was (ΔRA,ΔDec) = (+0.43″ ± 2.31″ , -2.57″ ±2.56″), which are consistent with the absolute and systematic errors reported in the SUMSS Catalogue. The ATCA component catalogue was also cross-correlated with the positions of bright compact optical galaxies from our CTIO MOSAIC-II survey (see Table 1), which was astrometrically referenced against HST guide stars, and sources from the DENIS database. The
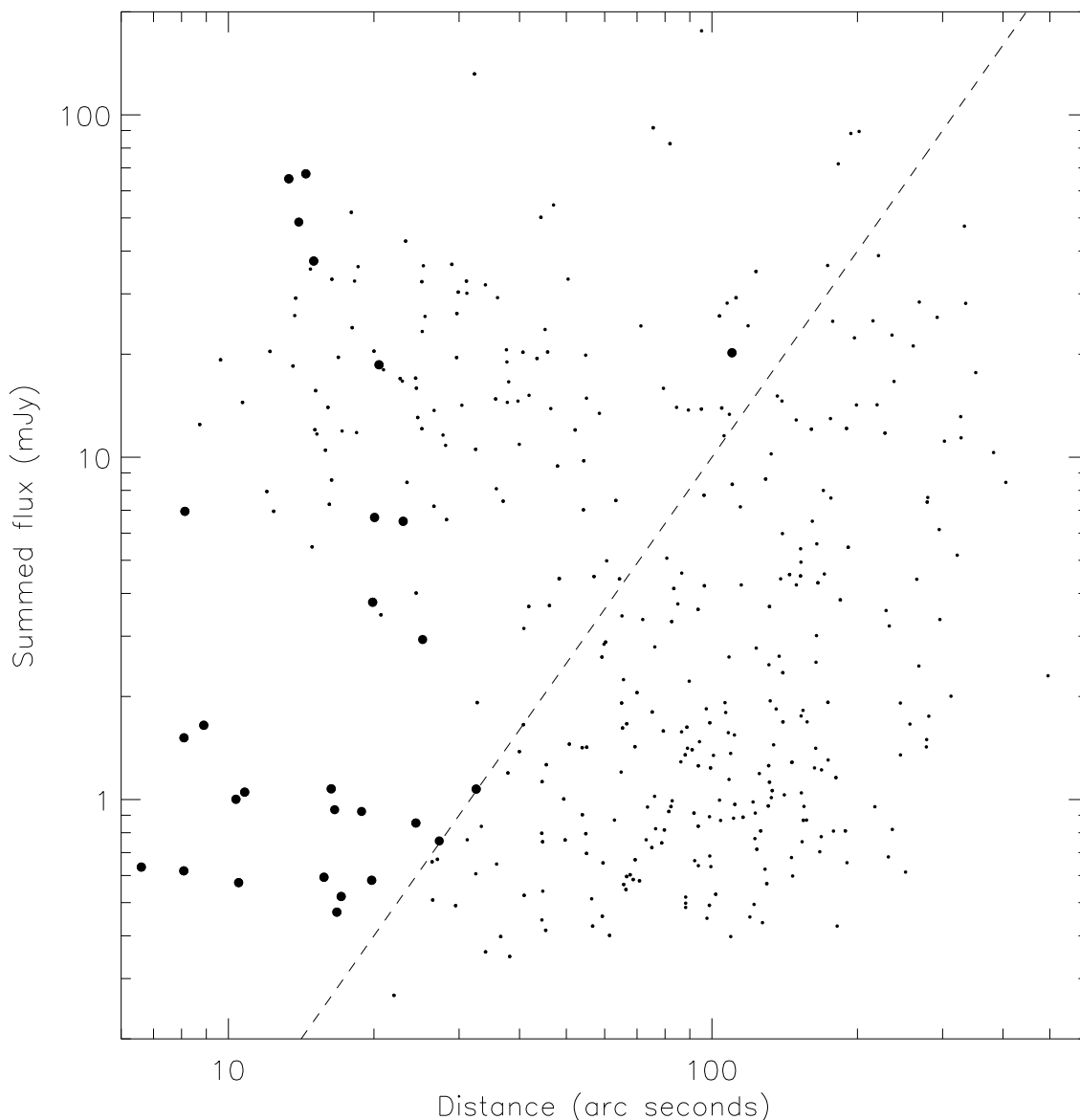
Figure 4. This Figure shows the sum of the flux densities of the nearest neighbours between components in the detection catalogue. Following Magliocchetti et al. (1998) points to the left of the dashed line are possible double sources. The likelihood that two sources in a pair are related is further constrained (Magliocchetti et al. 1998) by requiring that the fluxes of the two components f_1 and f_2 should be in the range $0.25 \leq f_1/f_2 \leq 4$. Sources in the Figure whose components satisfying this additional criterion are shown as bold circles.

mean of the offsets to the 166 bright galaxies shown in Figure 5 was Δ RA = -0.16″ ± 0.37″ and Δ Dec = -0.05″ ± 0.46″ , which is also consistent with the SUMSS result.

4.4   Summary of flux density corrections for systematic effects

There are two main systematic effects which have been taken into account to estimate the ATCA flux densities, specifically clean bias and bandwidth smearing effects. Bandwidth smearing is the radio analog of optical chromatic aberration, resulting from the finite width of the receiver chan-

Table 3. The multi-component source catalogue for components satisfying the Magliocchetti et al. (1998) criterion. The proposed multi-component sources listed in this Table are: (1) the components identified according to their Running Numbers in the main catalogue, (2,3) mean Right Ascension and Declination (J2000) taken and the average of the positions of the individual components, (4) the distance between the components (rounded up to the nearest arc second), (5) the sum of the total flux density of the individual components, (6) the error on this, estimated by adding the total flux errors in quadrature.

Components	RA h:m:s.s	Dec d:m:s.s	Dist $''$	S_c mJy	ΔS_c mJy
(1)	(2)	(3)	(4)	(5)	(6)
47+49	4:43:09.2	-53:39:30.0	9	1.651	0.029
65+67	4:43:38.8	-53:47:24.1	17	0.521	0.026
69+70	4:43:43.3	-53:22:18.1	11	1.050	0.034
99+102	4:44:18.9	-53:24:38.8	20	18.617	0.241
122+123	4:44:35.9	-53:36:01.4	8	1.515	0.031
140+141	4:44:53.1	-53:41:00.4	8	6.949	0.058
166+169	4:45:19.3	-53:12:26.2	16	1.075	0.028
171+172+175	4:45:22.6	-53:09:09.4	20	1.450	0.021
179+180	4:45:25.8	-53:06:08.2	16	0.593	0.042
212+213	4:46:03.1	-53:44:41.6	17	0.469	0.026
223+224	4:46:16.6	-53:39:21.9	15	67.264	0.431
227+228	4:46:20.4	-52:56:23.8	13	65.058	0.445
238+240+241	4:46:32.6	-53:47:00.4	18	71.759	0.172
250+251	4:46:43.7	-53:17:59.8	20	6.669	0.062
248+253	4:46:46.0	-53:01:00.5	110	20.188	0.141
265+268	4:47:03.2	-53:35:39.4	15	37.415	0.181
284+286	4:47:16.2	-52:59:27.8	17	0.935	0.399
305+306	4:47:32.2	-53:20:22.8	10	1.102	0.020
318+320	4:47:44.0	-53:10:37.4	20	3.771	0.052
336+337	4:48:02.5	-53:26:14.4	7	0.635	0.031
371+373	4:48:40.6	-52:59:31.5	33	1.073	0.399
378+379+380	4:48:44.9	-53:00:04.8	30	3.712	0.043
410+411	4:49:28.5	-53:26:05.0	11	0.572	0.026
425+428	4:49:53.7	-53:12:02.8	28	0.854	0.036
434+436	4:50:14.7	-53:25:08.6	23	6.499	0.049

nels compared to the observing frequency. It reduces the peak flux density of a source while correspondingly increasing, or blurring, the source size in the radial direction such that the total integrated flux density is conserved, but the peak flux is reduced.

From Condon et al. (1998) the reduction in the peak flux from a compact radio source as a result of bandwidth smearing is given by:

$$\frac{S_{peak}}{S_{peak}^0} \cong \frac{1}{\sqrt{1 + \left[\frac{2\ln 2}{3}\right]\left[\left(\frac{\Delta \nu}{\nu}\right)\left(\frac{d}{\theta_b}\right)\right]^2}} \qquad (2)$$

where S_{peak} and S_{peak}^0 refer to the off-axis peak flux and the peak flux at the centre of axis of the primary beam, $\Delta \nu$ and ν are the bandwidth and observing frequency respectively, d is the off-axis distance, and θ_b is the synthesised beamwidth. Prandoni et al. (2000a) have made a detailed study of this for the ATCA telescope, finding similar behaviour.

Fortunately, the closely spaced mosaicing strategy used for the ATCA SEP observations allows the smearing effect to be measured directly, by monitoring peak and integrated flux densities of four bright compact sources that were present in virtually every one of the observed fields, but at different distances from the centre of the beam. Figure 6 shows the measured smearing factor k,
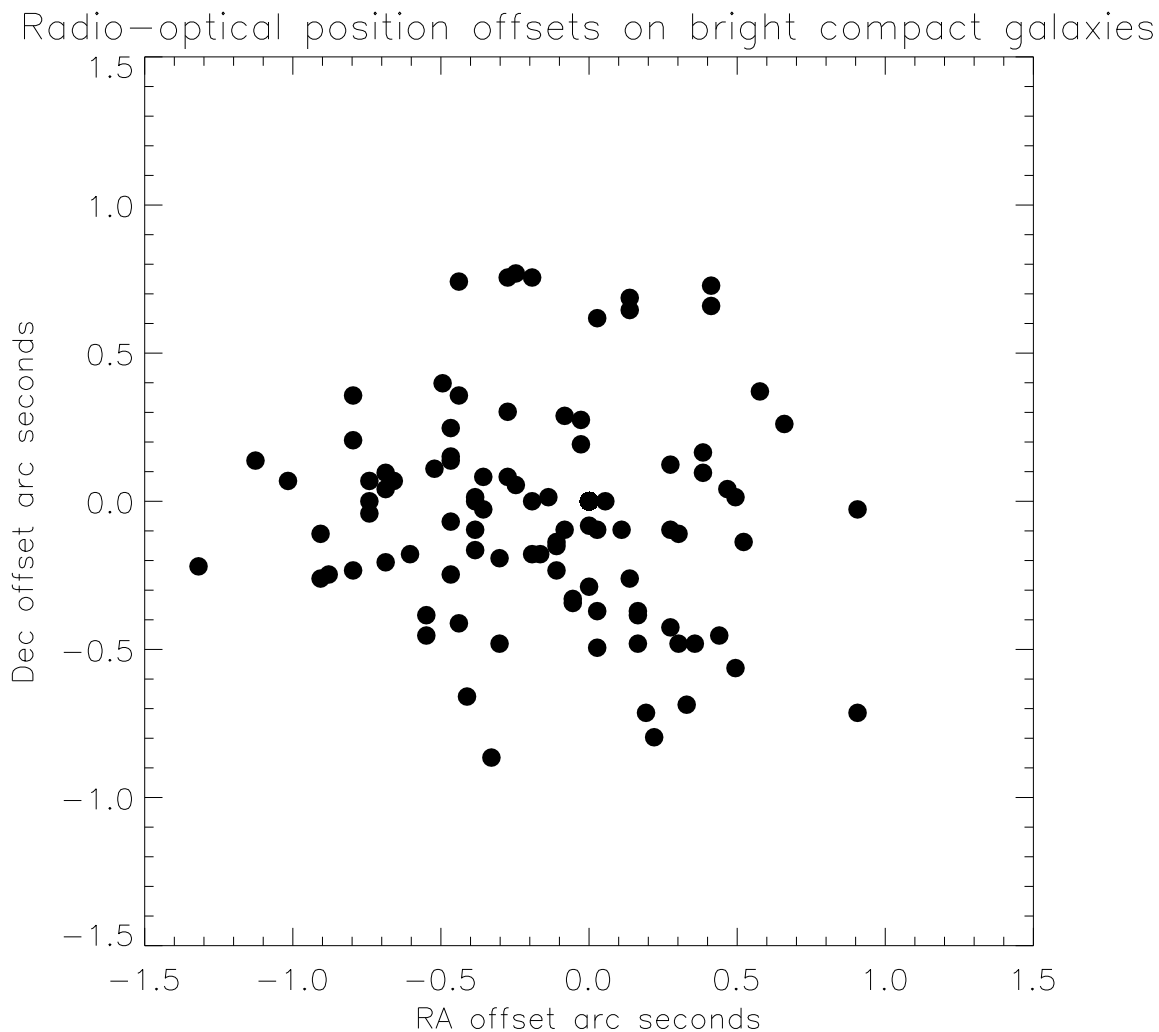
Figure 5. Positional offsets between bright (R-magnitude ≤ 22 mag) galaxies from the CTIO MOSAIC-II images and the DENIS database, and a sample of ATCA radio components detected at ≥ 10σ levels in Table 2.

which we define as the ratio of the peak flux of a compact source normalised to that which it has when at the centre of a beam, as a function of distance from the beam centre.

This Figure shows that the experimental data points are reasonably well fit by the theoretical relationship of Condon et al. (1998), which is overlaid as a solid line on Figure 6. This correction was taken into account when estimating the peak fluxes listed in Table 2.

It is well known that as well as needing to consider this effect for single pointings, large mosaiced fields and chromatic aberration, it can also act to reduce point source fluxes in a complex way (e.g. Bondi et al. 2008, White et al. 2010). **We have empirically examined the effect of bandwidth smearing on our mosaiced data by following the approach adopted by Bondi** et al. (2008) to compare the fluxes of bright sources observed close to the centres of individual pointings, with their fluxes determined after mosaicing together to form a merged image. Although
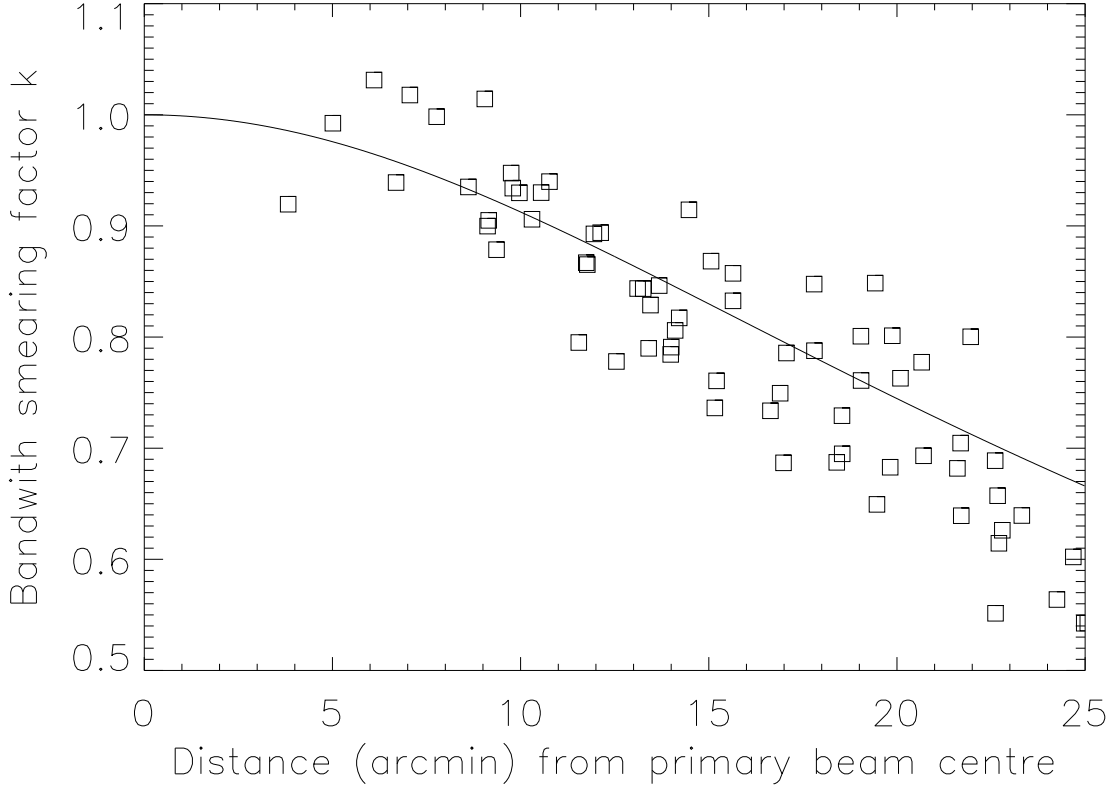
Figure 6. Variation of the smearing factor with distance from the centre of an individual field for a sample of components in common to many of the individual fields. The solid curve is the expected theoretical curve from Condon et al. (1998). which matches closely to that shown by Huynh et al. (2005) in their ATCA observation of the Hubble Deep Field South, and the squares show the .

the bandwidth smearing can be accounted for using the above equation from Condon et al. (1998), as Bondi et al. (2008) discuss, the contribution of this to measurements of the peak fluxes in radio surveys is more difficult to rigorously quantify for mosaiced data, where the smearing would need to be modelled with a more complicated function that represents the spacing pattern of the individual pointings. Due to the difficulty in rigorously calculating this, we have therefore followed the Bondi et al. (2008) approach to estimate the most probable reduction to the peak flux densities, as this correction will slightly modify estimates of the estimated source sizes.

Therefore, we ran the same procedure that was used to produce the final radio catalogue, on each of the individual pointings. For the strongest unresolved sources ($\gtrsim 1$ mJy) the peak and total flux densities measured from the final mosaiced image, were compared with the corresponding peak and total flux densities from the individual pointings, using sources that were no further than 5′ away from an individual pointing (this is consistent with the Bondi et al. 2008 approach for the VLA, which is supported for ATCA from our own results shown in Fig. 7). The total flux densities of each source in the mosaic were in good agreement (the median value was measured to be 1.01
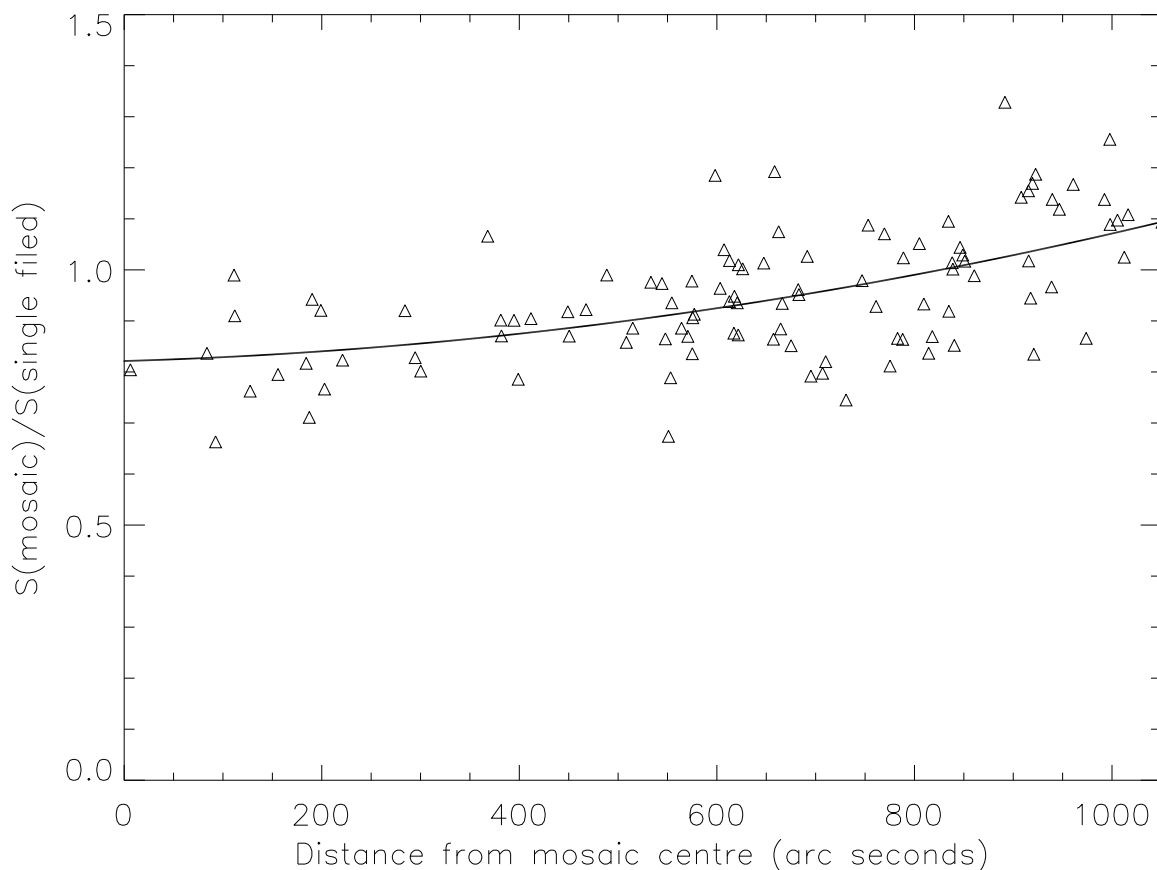
Figure 7. Ratio between the peak flux densities in the final mosaic and in the individual pointing where the source is within 5′ from the centre vs. the radial distance from the centre of the final mosaic. Only compact sources with flux densities greater than 1 mJy beam^{-1} are plotted. The fitted curve corresponds to a second order polynomial fit to the data represented by the relationship S(mosaic)/S(single field) = 0.82+5.64 10^{-5} d$_{centre}$ + 1.93 10^{-7} d$_{centre}^2$, whereS(mosaic)/S(single field) and d$_{centre}$, the distance in arc seconds from the centre of the mosaiced field, correspond to the vertical and horizontal axes.

with an rms dispersion of 0.02), as would be expected for complete recovery of the flux. However, for components whose peak fluxes are affected by bandwidth smearing, the peak fluxes could be underestimated in the final mosaic on average by up to 20%. The peak fluxes listed in Table 2 have all been corrected for this, according to the centre of the mosaiced image of Right Ascension (J2000) = 4^h 46^m 46^s.5, Declination (J2000) -53° 24′ 59″.0.

The other main effect that can influence fluxes is clean bias. Radio surveys, and in particular those consisting of short snapshot observations, have a tendency to be affected by the clean bias effect where the deconvolution process leads to a systematic underestimation of both the peak and total source fluxes. This is a consequence of the constraints on the cleaning algorithm due to sparse uv coverage (see Becker et al. 1995, White et al. 1997, Condon et al. 1998), and has the effect of redistributing flux from point sources to noise peaks in the image, reducing the flux density of the real sources. As the amount of flux which is taken away from real sources is independent of

the source flux densities, the fractional error this causes is most pronounced for weak sources. Prandoni et al. (2000a, b) have shown that it is possible to mitigate clean bias if the CLEANing process is stopped well before the maximum residual flux has reached the theoretical noise level. Consequently the cleaning limit was set at 5 times the theoretical noise, to ensure that the clean bias does not significantly affect the source fluxes in the present survey (Garrett et al. 2000). Gruppioni et al. (1999) adopted a similar strategy in an ATCA survey of the ELAIS N1 field, and found the effect to be insignificant (less than 2.5%) for the faintest sources (5σ detections) but had no effect on sources brighter than 10σ for similar numbers of CLEAN cycles as those performed on the present ATCA data. We therefore conclude that clean bias will have a negligible affect on the present data.

5 DIFFERENTIAL COUNTS

In Figure 8 the differential radio source counts are shown from the ATCA-ADFS field, normalised to a static Euclidean universe ($\mathrm{d}N/\mathrm{d}S\ S^{2.5}$ ($\mathrm{sr}^{-1}\mathrm{mJy}^{1.5}$)). These source counts are broadly consistent with previous results at 1.4 GHz (e.g. the compilation of Windhorst et al. (1993), the PHOENIX Deep Survey (Hopkins et al. 2003), and the shallow *NEP* survey of Kollgaard et al. (1994)).

The data from Figure 8 are given in Table 4, where the integrated flux bins and mean fluxes for each of the bin centres are listed in columns (1 and 2), the number of sources corrected for clean and resolution bias are shown in column (3), and the number of sources corrected for the area coverage and multi-component sources in Column 4, and in the final column (5) the differential source counts and their associated errors as defined by Kollgaard et al. (1994) are listed.

To model the observed source counts a two component model was used consisting of a classical bright radio loud population and a fainter star-forming population. It is well established that classical bright radio galaxies require strong evolution in order to fit the observed source counts at radio wavelengths (Longair 1966, Rowan-Robinson 1970). The source counts above 10 mJy are dominated by giant radio galaxies and QSOs (powered by accretion onto black holes, commonly joined together in the literature under the generic term AGN). Radio loud sources dominate the source counts down to levels of ~1 mJy, however, at the sub-mJy level the normalised source counts flatten as a new population of faint radio sources emerge (Windhorst et al. 1985). The dominance of starburst galaxies in the sub-mJy population is already well established (Gruppioni et al. 2008), where the number of blue galaxies with star-forming spectral signatures is seen to
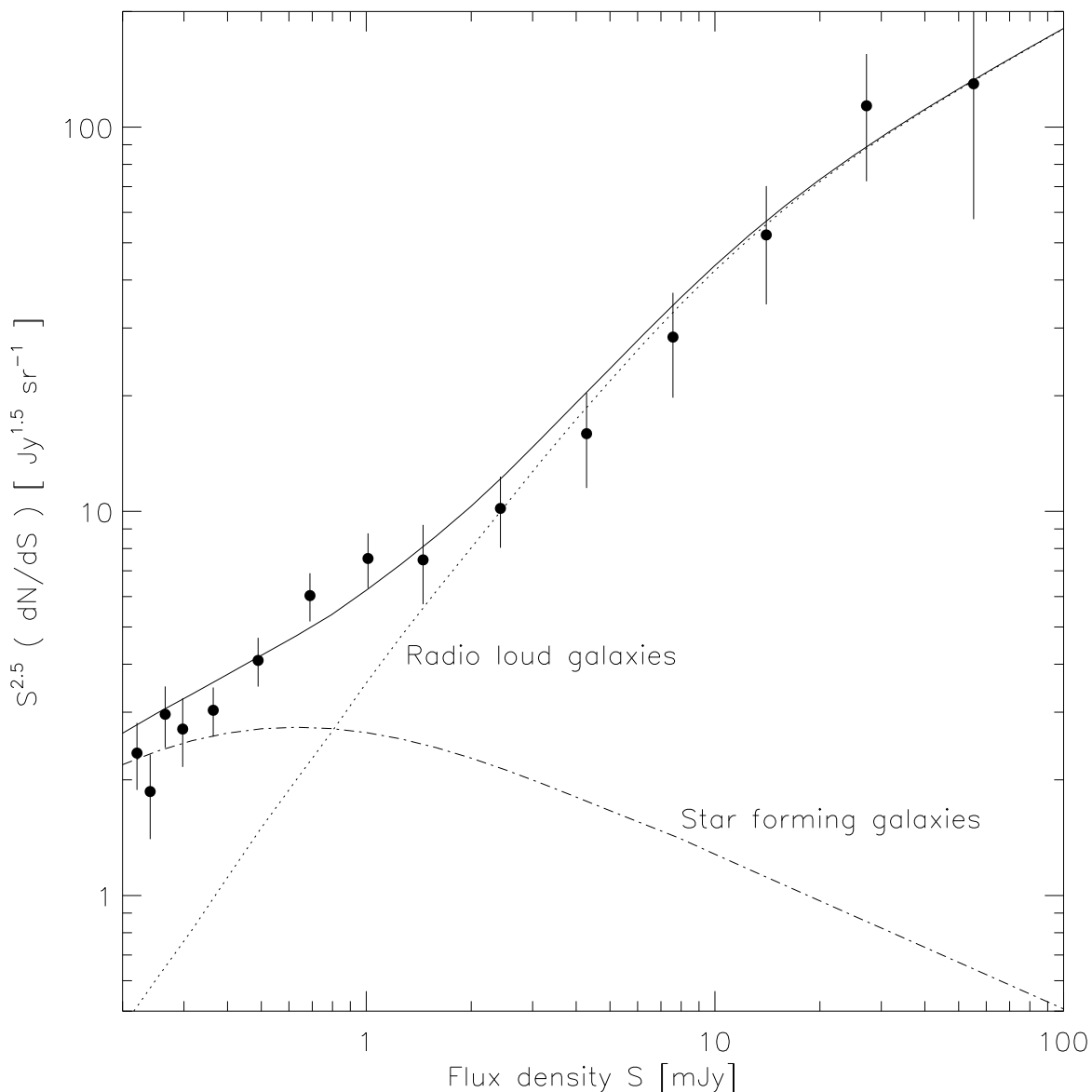
Figure 8. Differential counts determined from the AKARI ATCA-ADFS 20 cm deep field. The relationship for calculating the numbers in this plot and in Table 4 is the same as that used by Kollgaard et al. (1994).

increase strongly. Rowan-Robinson et al. (1980, 1993), Hopkins et al. (1998), and others have concluded that the source counts at these faintest levels require two populations, AGNs and starburst galaxies. This latter population can best be modelled as a dusty star-forming population, under the assumption that it is the higher redshift analogue of the IRAS star-forming population (Rowan-Robinson et al. 1993, Pearson & Rowan-Robinson 1996). In this scenario, the radio emission originates from the non-thermal synchrotron emission from relativistic electrons accelerated by supernovae remnants in the host galaxies.

To represent the radio loud population the luminosity function of Dunlop & Peacock (1990)

Table 4. 20 cm differential source counts for the ATCA-ADFS survey

flux bin mJy (1)	mean flux mJy (2)	N_0 (3)	N_c (4)	dN/dS sr^{-1} $Jy^{1.5}$ (5)
0.21–0.23	0.22	16	25.45	2.35±0.47
0.23–0.25	0.24	14	19.50	2.24±0.51
0.25–0.28	0.265	23	30.30	2.96±0.54
0.28–0.315	0.298	20	24.24	2.72±0.55
0.315–0.413	0.364	51	48.01	3.11±0.45
0.413–0.566	0.490	49	50.72	4.37±0.61
0.566–0.813	0.690	49	50.72	6.30±0.88
0.813–1.21	1.011	32	37.77	7.54±1.23
1.21–1.70	1.455	11	18.36	7.47±1.75
1.70–3.151	2.425	17	22.66	10.18±2.14
3.151–5.416	4.283	10	12.95	15.93±4.43
5.416–9.742	7.579	9	10.79	28.41±8.65
9.742–18.33	14.036	4	8.63	52.41±17.84
18.33–36.08	27.205	7	7.55	113.7±41.35
36.08–74.32	55.200	2	3.24	129.7±72.07

was used (parameters in Table C3 in their paper) to model the local space density with an assumption that the population evolves in luminosity with increasing redshift. The luminosity evolution follows a power law with redshift of $(1 + z)^{3.0}$, broadly consistent with both optically and X-ray selected quasars (Boyle et al. 1987). The spectrum of the radio loud population was obtained from Elvis, Lockman & Fassnacht (1994), assuming a steep radio spectrum source of ($S_\nu \propto \nu^{-\alpha}$, α=1).

To model the faint sub-mJy population we use the *IRAS* 60 μm luminosity function of Saunders et al. (2000), with the parameters for the star-forming population, defined by warmer 100 μm / 60 μm *IRAS* colours, given in Pearson (2001, 2005), and Sedgwick et al. (2012).

To convert the infrared luminosity function to radio wavelengths, we derive below the ratio of the 60 μm luminosity to the radio luminosity, from the well established correlation between the far-IR and radio flux (e.g. Helou, Soifer & Rowan-Robinson (1985), Yun, Reddy & Condon (2001), Appleton et al. (2004)).

Helou et al. (1985) defined this relation between the far-infrared flux, FIR/Wm^{-2} and the 1.4 GHz radio emission, $S_{1.4GHz}/\text{Wm}^{-2}\text{Hz}^{-1}$ in terms of the q factor given by,

$$q = \log\left(\frac{FIR}{3.75 \times 10^{12}\text{Hz}}\right) - \log\left(\frac{S_{1.4\ GHz}}{\text{Wm}^{-2}\ \text{Hz}^{-1}}\right) \tag{3}$$

The far-infrared flux defined by Condon (1991) in terms of the 60 μm and 100 μm emission can be written as,

$$\left(\frac{FIR}{\text{Wm}^{-2}}\right) = 1.26 \times 10^{12}\left(\frac{2.58\ S_{60} + S_{100}}{\text{Wm}^{-2}\ \text{Hz}^{-1}}\right) \tag{4}$$

where the spectrum between 60 μm and 100 μm is defined by a spectral index α,

$$\frac{S_{100}}{S_{60}} = \left(\frac{\nu_{100}}{\nu_{60}}\right)^{-\alpha} \Rightarrow S_{100} = 1.67^\alpha S_{60} \tag{5}$$

such that,

$$\left(\frac{FIR}{\text{Wm}^{-2}}\right) = 1.26 \times 10^{12} \left(\frac{2.58 + 1.67^{\alpha}}{\text{Wm}^{-2}\,\text{Hz}^{-1}}\right) S_{60} \tag{6}$$

substituting the above relation into Equation 3, assuming a value of q=2.3 (Condon 1991,1992) and a value of α=2.7 (Hacking et al. 1987), it is then easy to show that:

$$S_{60} \approx 90\,S_{1.4\,\text{GHz}} \tag{7}$$

To convert the infrared luminosity function to radio wavelengths we adopt the above $S_{60\,\mu\text{m}}/S_{1.4\,\text{GHz}}$ ratio. We utilise the spectral template of the archetypical starburst galaxy of M82 from the models of Efstathiou, Rowan-Robinson & Siebenmorgen (2000) for the spectral energy distribution of the star-forming population. The radio and far-infrared fluxes are correlated due to the presence of hot OB stars in giant molecular clouds that heat the surrounding dust producing the infrared emission. These stars subsequently end their lives as supernovae with the radio emission powered by the synchrotron emission from their remnants. The radio spectrum is characterised by a power law of ($S_{\nu} \propto \nu^{-\alpha}$, α=0.8).

Pure luminosity evolution for the star-forming population is assumed with a best fit power law $\propto (1 + z)^{3.2}$. This infrared representation of the star-forming population was preferred over using the radio luminosity function directly, since it creates a phenomenological link between the radio emission and the infrared which is responsible for the bulk of the emission in the star-forming population. The observed number counts at fainter fluxes (<1mJy) vary widely from survey to survey resulting in a distribution of the best fitting evolution parameterisation. Huynh et al. (2005) used the radio luminosity function of Condon et al. (2002) and derived a best fitting evolution parameterisation $\propto (1 + z)^{2.7}$, slightly lower than the work presented here. Hopkins (2004) and Hopkins et al. (1998) used radio and infrared luminosity functions respectively obtaining evolution in the sub-mJy population $\propto (1 + z)^{2.7}$ and $\propto (1 + z)^{3.3}$ respectively. Comparing our observations and assumed evolution with the results of our survey in the *AKARI* deep field at the North Ecliptic Pole (Paper 1) we find that our derived evolution for the AGN and star forming components ($(1 + z)^{3.0}$, $(1 + z)^{3.2}$ respectively) are consistent with the values arrived at for the survey at the North Ecliptic Pole ($(1 + z)^{3.0}$ for both components). Both of our surveys at both ecliptic poles (each covering areas of $\gtrsim 1$ deg^2, similar to the VLA-COSMOS survey of Bondi et al. (2008) and larger than the other surveys depicted in Figure 9) result in number counts at the lower end of the emerging picture on excess sub-mJy radio counts, as shown in Figure 9.
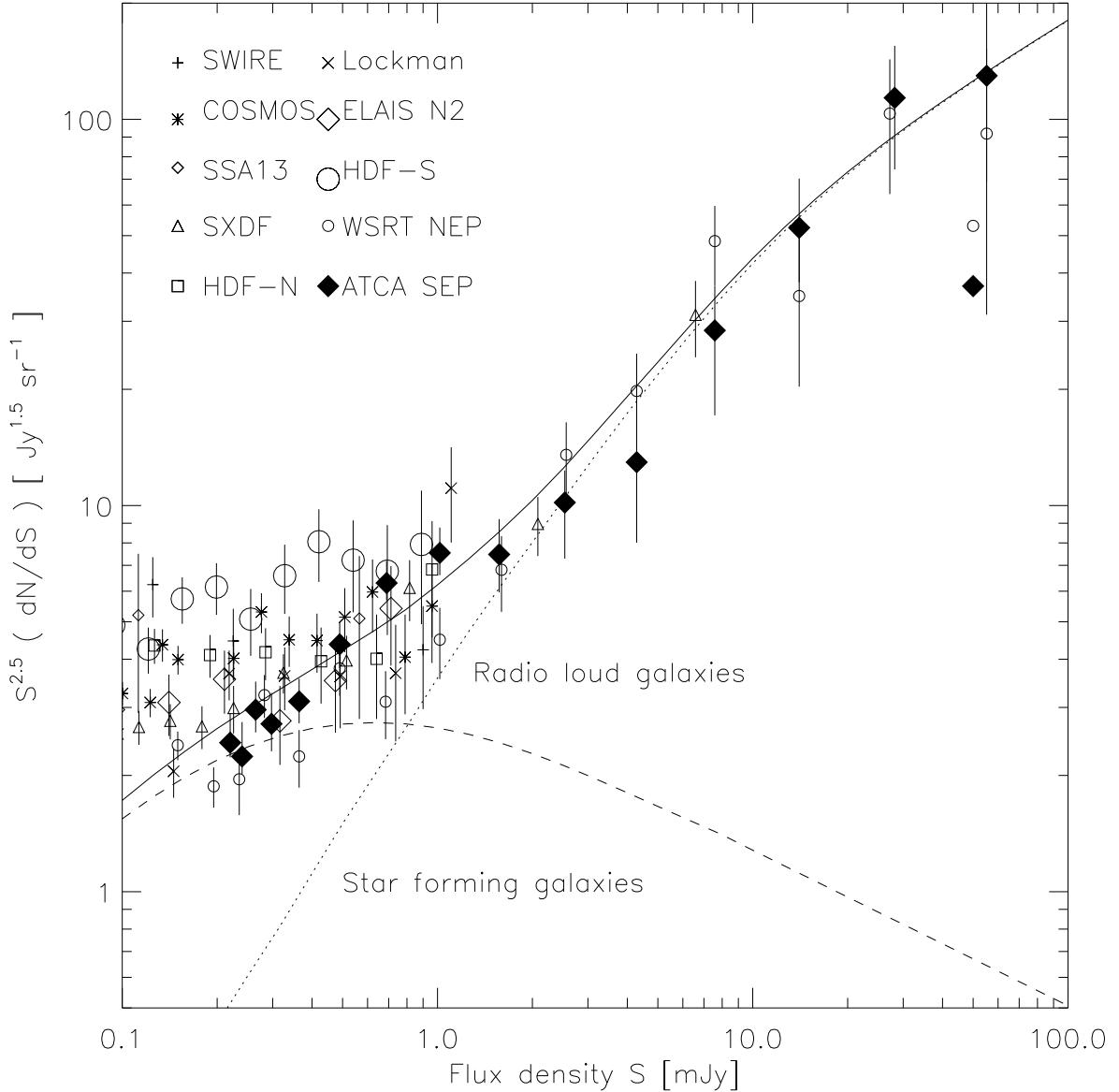
Figure 9. A compilation of the differential source counts of a number of deep 20 cm radio surveys taken from: SWIRE (Owen & Morrison 2008); COSMOS (Bondi et al. 2008); SSA13 (Fomalont et al. 2006); SXDF (Simpson et al. 2006); HDF-N, LOCKMAN and ELAIS N2 (Biggs & Ivison 2006), and the HDF-S (Huynh et al. 2005). The solid curve is the best fit to the present data taken as described in Figure 8. There are however differences in the instrumental and systematic corrections that have been made for the different survey results shown here (see detailed discussion by Prandoni et al. 2000 a,b), that make quantitative comparison at the faintest flux levels somewhat uncertain.

6 CROSS-MATCHES WITH DEEP FIELD CATALOGUES AT OTHER WAVELENGTHS

To compare the ATCA radio catalogue with the AKARI FIS 90 μm ADF-S catalogue (Shirahata et al. *in preparation*), we have cross-matched AKARI sources and radio components to search for positional coincidences $\leq 6''$ based on the AKARI positional uncertainty as defined in Verdugo et al. (2007) and the radio components reported in this paper. In the case of the possible double

or complex radio sources (see Figures 4 and 3) we have also searched for candidate identification along a line joining the presumed associated radio components. The AKARI FIS catalogue covers the entire 12 deg^2 of the ADF-S and contains 391, 2282, 315 and 216 sources at 65 μm, 90 μm, 140 μm, 160 μm above 5σ detection sensitivities of 28.47 mJy, 12.81 mJy, 121.03 mJy and 372.68 mJy respectively. From this cross matching we recovered 35 sources in common to both catalogues, twenty-five of which are also reported in the *Spitzer* 70 μm catalogue (Clements et al. 2011). We list the ATCA-AKARI cross-matched sources in Table 5, along with R-band detections from our CTIO MOSAIC-II survey (or in a few cases that are marked with a *dagger* symbol from DENIS R-band fluxes), and redshifts from the AAT/AAOmega redshift survey. The *Herschel* data are described in the Figure caption of Table 5. The 41 cross matched sources, all of which lay within a 5″ error circle, the mean positional agreement was 1.93±1.25″, showing very good agreement of the coordinate systems.

6.1   Infrared cross matches (*AKARI*, *Spitzer*)

Figure 10 shows the comparison between the fluxes of matched ATCA radio – 90 μm sources detected in our survey as well as a larger sample of radio and 90 μm fluxes taken by cross-correlating with the AKARI All-Sky Survey FIS catalogue (Yamamura et al. 2010, Oyabu et al. 2009, 2010) with the compilation of radio sources given by Dixon (1970). Although this Figure does not apply a *K*-correction to the measured fluxes, it does show us that although many of the ATCA-ADFS sources fall on an extrapolation of sources from Dixon's list to lower fluxes, several of them may be radio loud compared to the majority (in other words lie significantly to the right of the trend line), and which therefore may have active nuclei. Of these, the two most extreme are the following. Firstly, ATCA component 18 (J04421266-5355520) at redshift 0.044 appears on the NED extragalactic database as a bright edge-on spiral galaxy with DENIS Blue and Red magnitudes of 14.6 and 14.1 respectively, and in the GALEX FUV and NUV bands with 22.39 and 21.03 mag respectively. Secondly, ATCA component 187 is a bright radio source previously detected in the SUMSS survey (SUMSS J044532-540211) with a radio flux of 1.22 mJy at 834 MHz, suggesting that it may have brightened considerably (assuming a normal spectral index), and associated with an object having DENIS Blue and Red magnitudes of 18.4 and 17.7 mag respectively and a magnitude of 21.68 in the GALEX NUV band.

The radio identifications in Table 2 were cross-correlated with the *Spitzer* 24 μm and 70 μm catalogues (Scott et al. 2010), finding 173 and 31 matches at 24 μm and 70 μm respectively, using

Table 5. AKARI, *Spitzer* and *Herschel* associations with radio sources in the ATCA-ADFS survey. The *Herschel* (referenced as HSO in this Table) HerMES fluxes were extracted from the *Herschel* HerMES Public data release available from the LEDAM server at http://hedam.oamp.fr/HerMES/release.php, where we have used the band-merged StarFinder catalogues with the xID multi-band (250, 350 and 500 micron) fluxes measured at the positions of the StarFinder 250 micron sources.

No	S_{20cm} mJy	CTIO R mag	J mag	H mag	K mag	*Spitzer* 24 μm mJy	*Spitzer* 70 μm mJy	AKARI 65 μm mJy	AKARI 90 μm mJy	AKARI 140 μm mJy	HSO 250 μm mJy	HSO 350 μm mJy	HSO 500 μm mJy	Redshift z
18	2.291	14.1[†]	13.7	13.2	12.0	12.8	118.1	84.0	126.8	-	-	-	-	0.044
55	0.317	15.9[†]	14.9	14.0	13.9	5.4	43.3	41.6	58.2	-	91.9	39.6	8.4	0.092
63	0.335	17.9[†]	-	-	-	0.7	35.8	-	53.4	-	115.9	63.7	29.5	-
72	0.257	-	-	-	-	-	-	-	-	-	-	-	-	0.423
77	0.419	20.6	-	-	-	1.1	-	-	15.5	-	84.8	52.3	28.8	-
83	0.321	18.9	-	-	-	-	-	-	-	-	64.6	42.1	23.6	-
84	0.234	18.9	-	-	-	-	-	-	-	-	-	-	-	0.329
100	0.476	22.0	-	-	-	0.8	44.1	-	51.2	-	77.9	39.4	8.6	-
112	0.890	-	-	-	-	1.1	49.3	-	90.1	-	69.1	38.3	23.4	-
120	0.203	21.4	-	-	-	-	-	-	-	-	58.4	40.4	32.4	0.825
125	0.415	16.9	16.4	15.8	14.9	5.2	91.5	-	91.2	-	115.9	63.6	29.5	0.164
132	0.257	23.6	-	-	-	3.0	-	-	37.4	-	104.5	74.7	37.6	-
138	0.464	18.6	-	-	-	-	-	-	-	-	-	-	-	0.472
143	0.381	21.5	-	-	-	-	-	-	19.1	-	-	-	-	0.732
146	0.401	-	-	-	-	2.1	38.8	-	45.6	-	85.7	42.2	11.0	0.393
159	0.210	20.5	-	-	-	-	-	-	-	-	-	-	-	0.577
164	0.258	17.6	16.6	15.8	15.2	1.5	-	-	22.8	-	-	-	-	-
168	0.273	-	-	-	-	-	-	-	-	-	58.9	37.4	8.3	-
170	0.312	21.3	-	-	-	3.1	69.2	-	77.8	-	86.3	48.2	20.9	-
184	0.457	19.2	-	-	-	-	-	-	-	-	-	-	-	0.327
187	8.675	17.9[†]	16.4	-	-	22.0	35.4	-	19.3	-	-	-	-	0.121
194	0.510	19.2	-	-	-	5.4	88.8	44.8	96.9	-	64.1	22.2	1.8	0.290
195	0.492	17.9	16.5	-	-	6.0	49.2	-	48.1	-	-	-	-	0.237
203	0.361	-	-	-	-	-	-	-	-	-	64.8	47.3	26.4	-
206	0.952	17.5	-	-	-	-	-	-	-	-	75.1	45.2	18.6	0.361
214	0.276	14.3	13.4	-	12.2	3.7	105.5	-	115.9	-	145.9	58.4	13.7	-
225	0.177	-	-	-	-	-	-	-	-	-	-	-	-	0.181
235	0.942	23.1	-	-	-	2.5	-	-	24.7	-	86.2	59.2	31.5	-
252	0.350	22.3	-	-	-	6.7	36.7	-	36.4	-	-	-	-	0.154
255	0.295	22.3	-	-	-	-	-	-	-	-	62.9	39.7	22.4	-
266	0.929	-	-	-	-	-	-	-	-	-	55.5	45.1	31.9	-
277	0.798	15.3	14.5	-	13.3	2.6	80.0	-	103.2	245.0	158.7	68.6	20.4	-
283	0.300	-	-	-	-	0.2	-	-	15.3	-	-	-	-	-
284	0.594	-	-	-	-	3.8	67.2	-	65.9	-	75.3	39.8	24.6	-
290	1.182	-	-	-	-	-	-	-	-	-	59.2	45.3	22.1	-
297	0.270	17.8	16.6	15.8	15.5	3.3	45.8	49.4	63.0	-	-	-	-	0.069
301	0.154	18.8	-	-	-	-	-	-	40.5	-	-	-	-	0.223
302	0.273	21.2	-	-	-	-	-	-	13.6	-	-	-	-	0.760
309	0.215	-	-	-	-	1.3	-	-	25.7	-	-	-	-	-
330	0.263	-	-	-	-	7.7	53.3	-	40.2	-	-	-	-	0.181
333	0.184	-	-	-	-	-	-	-	27.2	-	64.3	32.7	11.1	0.108
336	0.301	-	-	-	-	-	-	-	-	-	191.2	83.9	10.1	-
337	0.334	17.1	13.6	12.8	12.3	-	112.1	91.9	161.5	439.0	186.4	82.8	52.8	0.0463
341	0.166	-	14.7	13.8	13.6	5.0	69.6	-	101.3	-	87.8	39.0	16.2	-
346	0.269	-	-	-	-	0.6	-	-	29.2	-	-	-	-	-
350	0.282	-	-	-	-	1.5	37.9	-	48.9	-	-	-	-	-
358	0.798	-	-	-	-	-	-	-	143.0	-	110.7	48.9	12.6	0.1140
359	0.397	-	-	-	-	-	-	-	-	-	59.6	46.7	28.0	-

the *Spitzer* single pixel size (2.45″ and 4.0″ at 24 μm and 70 μm respectively) as the search radius. The results of the 24 μm cross-matches are shown in Figure 11, and the large scatter of the plots highlights the difficulties of using the 24 μm fluxes as indicators of the radio flux.

This plot resembles that of Norris et al. (2006) showing a wide dispersion. To check for chance

Table 6. Table continues from above: AKARI, *Spitzer* and *Herschel* associations with radio sources in the ATCA-ADFS survey. The *Herschel* fluxes were extracted from the *Herschel* HerMES Public data release available from the LEDAM server at http://hedam.oamp.fr/HerMES/release.php, where we have used the band-merged StarFinder catalogues with xID multi-band (250 μm, 350 μm and 500 μm) fluxes measured at the positions of the StarFinder 250 μm sources.

No	S_{20cm} mJy	CTIO R mag	J mag	H mag	K mag	*Spitzer* 24 μm mJy	*Spitzer* 70 μm mJy	AKARI 65 μm mJy	AKARI 90 μm mJy	AKARI 140 μm mJy	HSO 250 μm mJy	HSO 350 μm mJy	HSO 500 μm mJy	Redshift z
410	0.301	16.3[†]	16.5	16.0	15.3	2.2	45.2	-	46.8	-	88.7	35.4	25.1	0.413
419	0.409	17.7[†]	-	-	-	3.6	66.7	48.9	71.7	-	72.7	34.1	-	0.346
421	0.617	16.5[†]	15.9	15.3	14.5	5.0	79.3	62.1	92.1	-	64.5	32.3	12.3	0.145
426	0.370	-	-	-	-	-	-	-	30.1	-	65.3	33.2	16.9	0.159
452	0.578	10.3[†]	12.4	11.6	11.4	-	-	20.8	355.9	618.9	101.9	78.8	-	0.0393
482	3.386	-	-	-	-	0.7	-	-	39.1	-	55.9	62.5	54.5	-
487	5.249	17.2[†]	16.8	15.9	15.1	8.1	70.5	-	81.9	-	62.4	33.8	16.7	0.064
491	14.68	-	-	-	-	0.7	-	-	39.3	-	71.4	31.2	-	-

associations, the radio coordinates were incremented by 60″ in both RA and Dec, and this new list of positions was cross-correlated with the *Spitzer* data to simulate what should be blank fields, resulting in 5 matches. Assuming that these are chance associations, the majority of the matched components ($\geq$ 97%) are likely to be real associations. The brightest *Spitzer* source shown in Figure 11 is ATCA component 187, which is associated with an R = 17.7 magnitude galaxy, and has a redshift of 0.121 (see Table 5). The ATCA components with *Spitzer* detections which have flux densities $\geq$ 10 mJy are 11, 12, 155, 160, 236, 446, 448, 458, 530.

6.2   Radio luminosity

The radio luminosity of the sources listed in Table 5 was calculated, assuming a cosmology of H_0 = 70 km s^{-1} Mpc^{-1}, with matter and cosmological constant density parameters of $\Omega_M = 0.3$, $\Omega_\Lambda =$ 0.7. The redshifts were measured using AAOmega, the fibre-fed optical spectrograph at the Anglo Australian Observatory as described by Sedgwick et al. (2011), and the resultant plot of the radio luminosity against redshift is shown in Figure 12, where we assume a mean radio spectral index of α = -0.7 (where $S \propto \nu^\alpha$) and apply the usual form of the *k*-correction $\kappa(z) = (1+z)^{-(1+\alpha)}$ at redshift *z*.

From studies of the local 1.4 GHz luminosity function, Sadler et al. (2002) and Mauch & Sadler (2007) have shown that the low luminosity population with radio luminosity $\sim 10^{23}$ W Hz^{-1} will mostly be luminous star-forming galaxies rather than radio-loud AGN (Eales et al. 2009, Jarvis et al. 2010, Hardcastle et al. 2010). Although most of the cross-matched ATCA/AKARI sources shown in Fig. 10 fall on the trend shown from the wider sample of cross matches between AKARI and Dixon's catalogue, ATCA components 18 and 187 appear to be radio-loud, although at the lower end of the luminosities reported from the local luminosity function for this class. However,
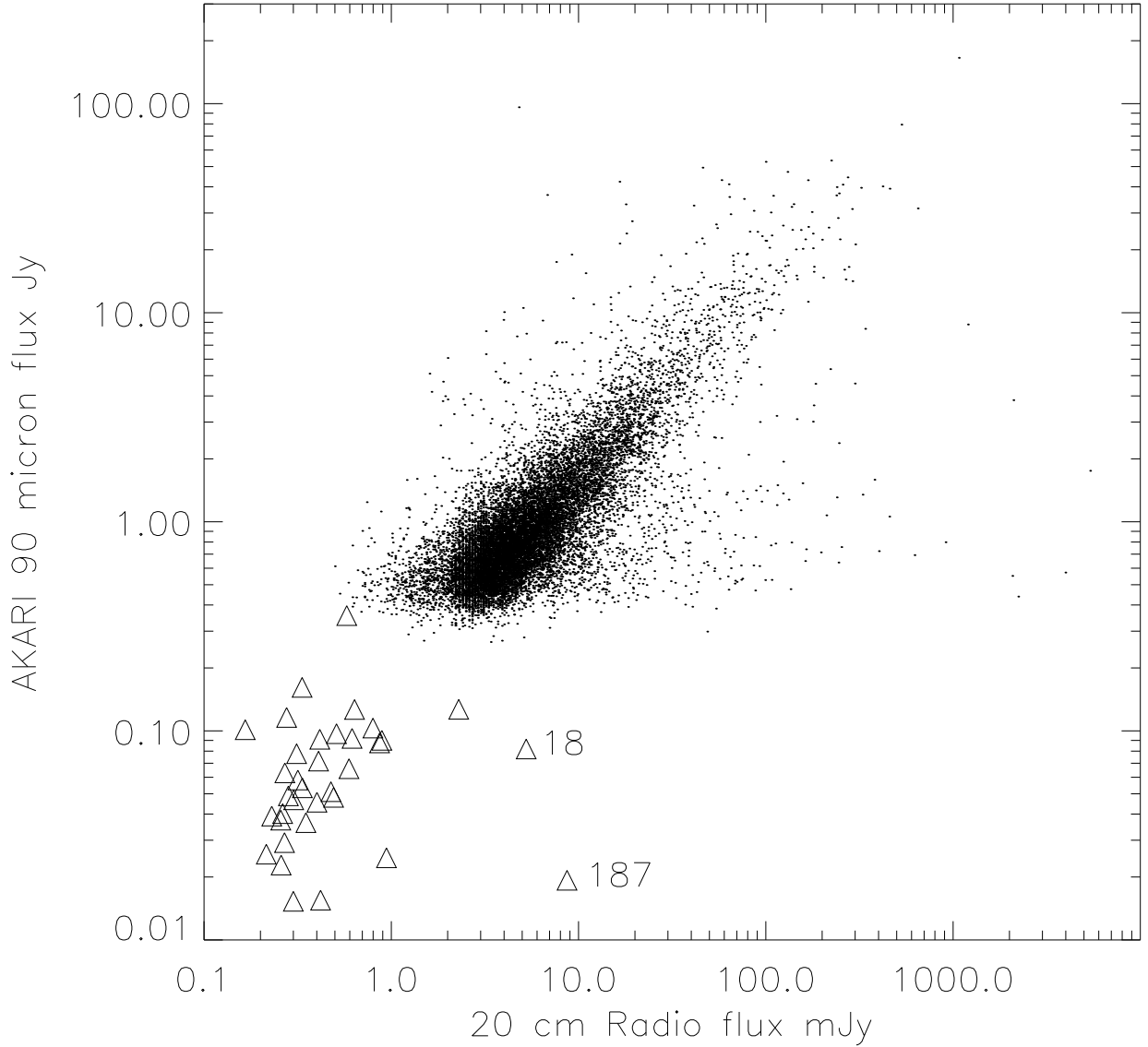
Figure 10. Radio flux against AKARI 90 μm flux (shown as triangles), compared to 20,000 matches between the AKARI All-Sky Bright Source Catalogue (Yamamura et al. 2010), and Dixon's Master list of radio sources (shown as dots). The reason for the break between the All-Sky Survey and ADF-S FIS survey points is because of the lower sensitivity of the All-Sky survey($\sim$ 0.4 Jy) by comparison to the deeper observations discussed here.The correlation between both FIS catalogues and Dixon's Master list of radio sources at 20 cm was made be searching for components that lay within $\pm 3''$ of each other. This conservative limit was chosen to enable secure detections, although the official AKARI FIS Bright source catalogue is $6''$ as described in Yamamura et al. (2010). Radio components 18 and 187 discussed in the text are marked in the Figure.

since most of the other cross-matches fit the trend-line, we conclude that the ATCA/AKARI cross identifications primarily trace the star-forming galaxy population.

6.3 Infrared Colours

To further investigate the nature of the ATCA/AKARI population we compare the infrared colours of our components from our ATCA survey with cross matches in both the AKARI 90 μm and *Spitzer* 24 μm & 70 μm bands. In Figure 13 we plot the 24 μm /90 μm – 90 μm /70 μm colour
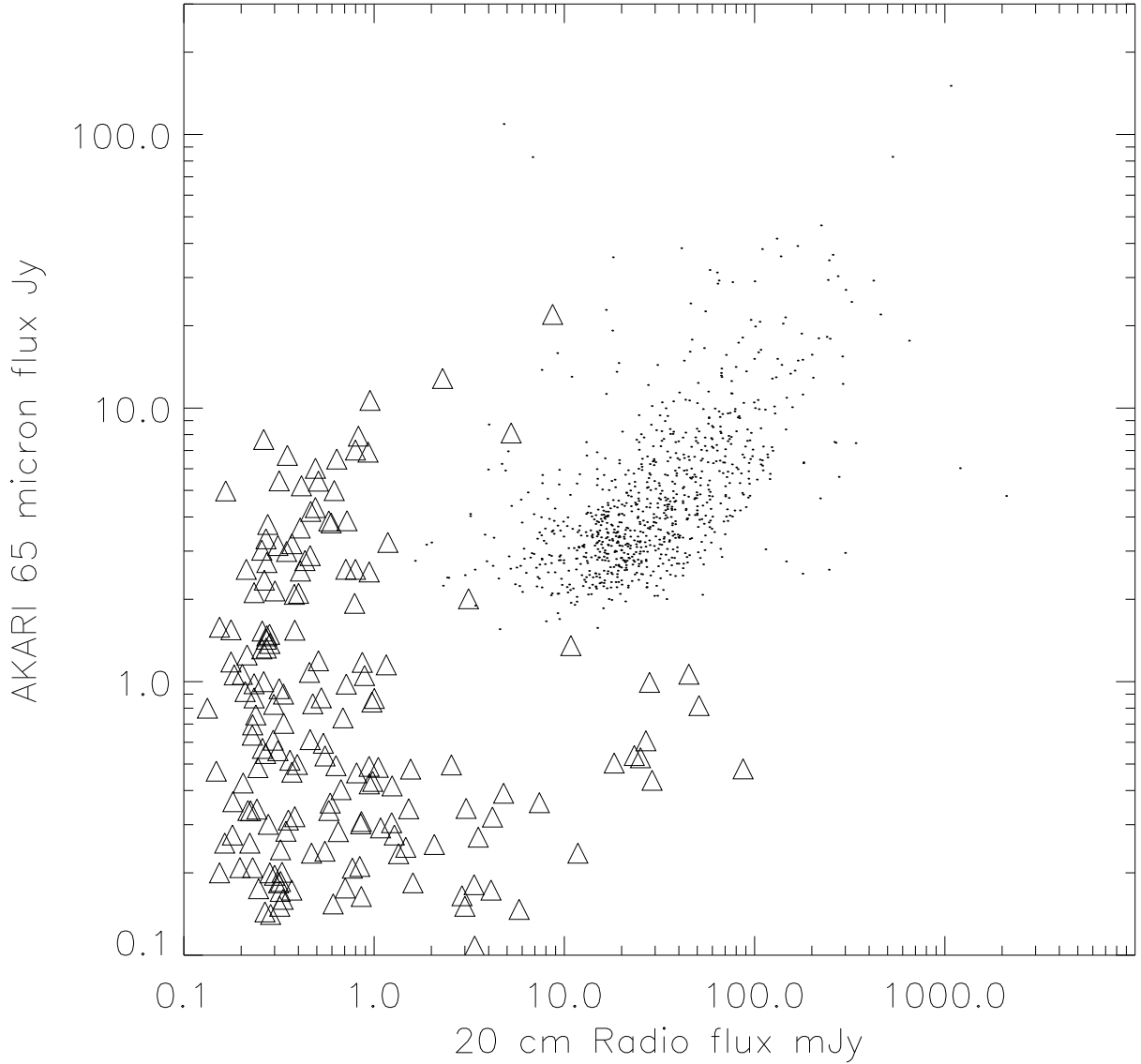
Figure 11. Radio components (shown as triangles) with matching *Spitzer* 24 μm sources within one *Spitzer* pixel. The *Spitzer* fluxes are the point response function fitted fluxes from Scott et al. (2010). The dots are matches between AKARI FIS 65 μm survey detections of bright radio sources taken from Dixon's Master radio catalogue (1970), for confirmed (i.e. quality flag 3) AKARI sources lying more than 10 degrees from the Galactic Plane as described in the caption of Figure 10.

distribution of our sources. The models were derived from the SEDs smoothed by the filter bands, and are overlaid onto the spectral tracks of an ensemble of star-forming galaxies from the models of Efstathiou et al. (2000) with increasing far-infrared luminosity from $L_{IR} > 10^{10}L_\odot$, $10^{11}L_\odot$, $10^{12}L_\odot$, together with the spectral track of an AGN torus from the models of Efstathiou & Rowan-Robinson (1995). From Figure 13 the infrared colours of the ATCA/AKARI population are consistent with those of star-forming galaxies, although there are selection effects (the requirement
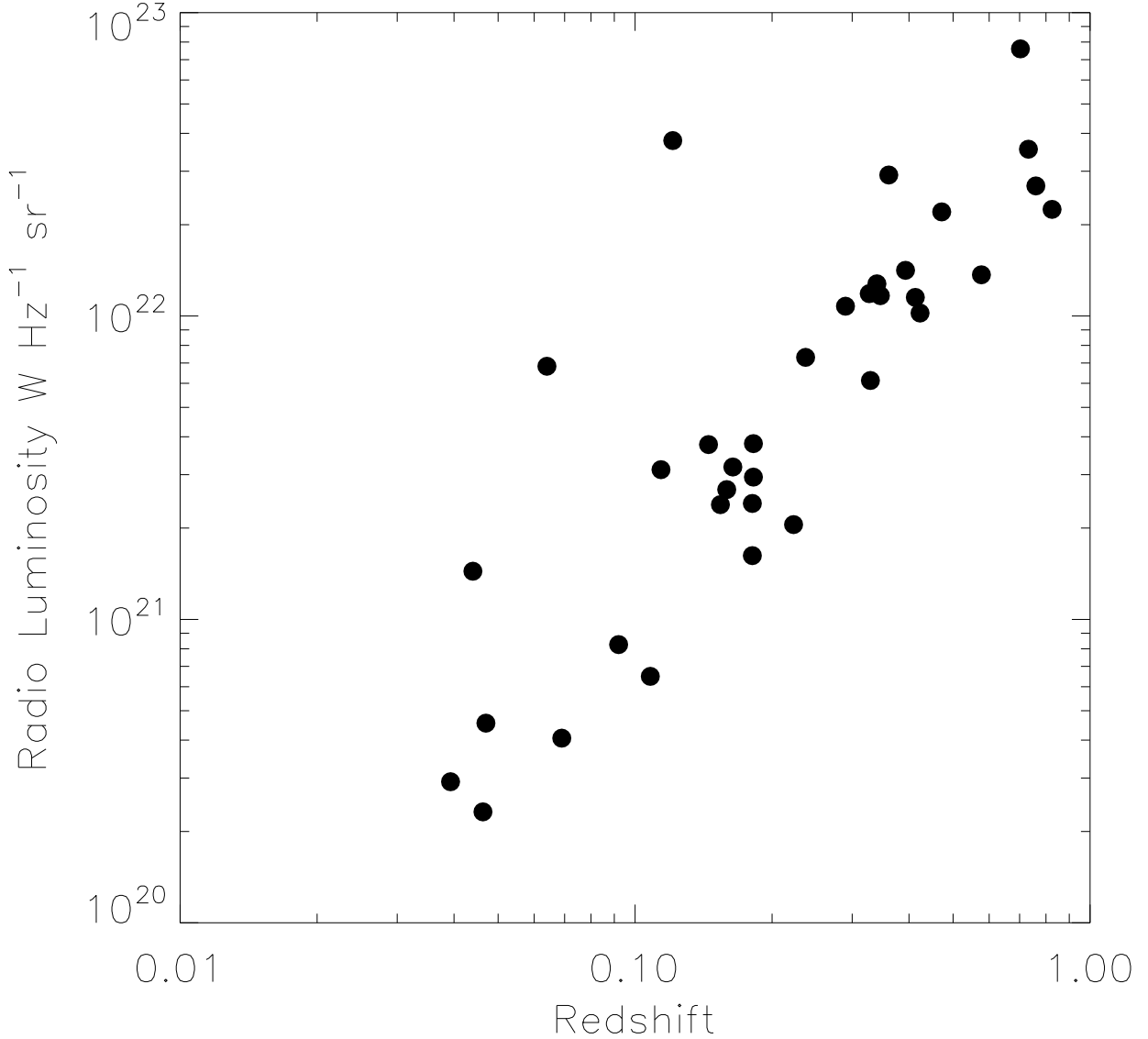
Figure 12. Radio luminosity as a function of the radio sources with measured spectroscopic redshifts listed in Table 5.

to have a 90 μm cross-match) which may bias this, and which would need to be tested with more sensitive infrared observations.

As a further check, the line ratios of [OIII]/H-β (lines at wavelengths of 486.1, 495.8, 500.7nm) and [OIII]/[OII] (OII doublet at 372.7 nm) were checked from the AAOmega spectra for the sources with redshifts >0.1, with the result that only one component (ATCA 302) shows ratios that are close to typical AGN values (Sedgwick et al. *in preparation*). Therefore the radio luminosities (Figure 12), infrared colour-colour plots (Figure 13) and AAOmega spectra all show a consistent picture, suggesting that the ATCA/AKARI cross-identifications predominantly trace a star-bursting population.
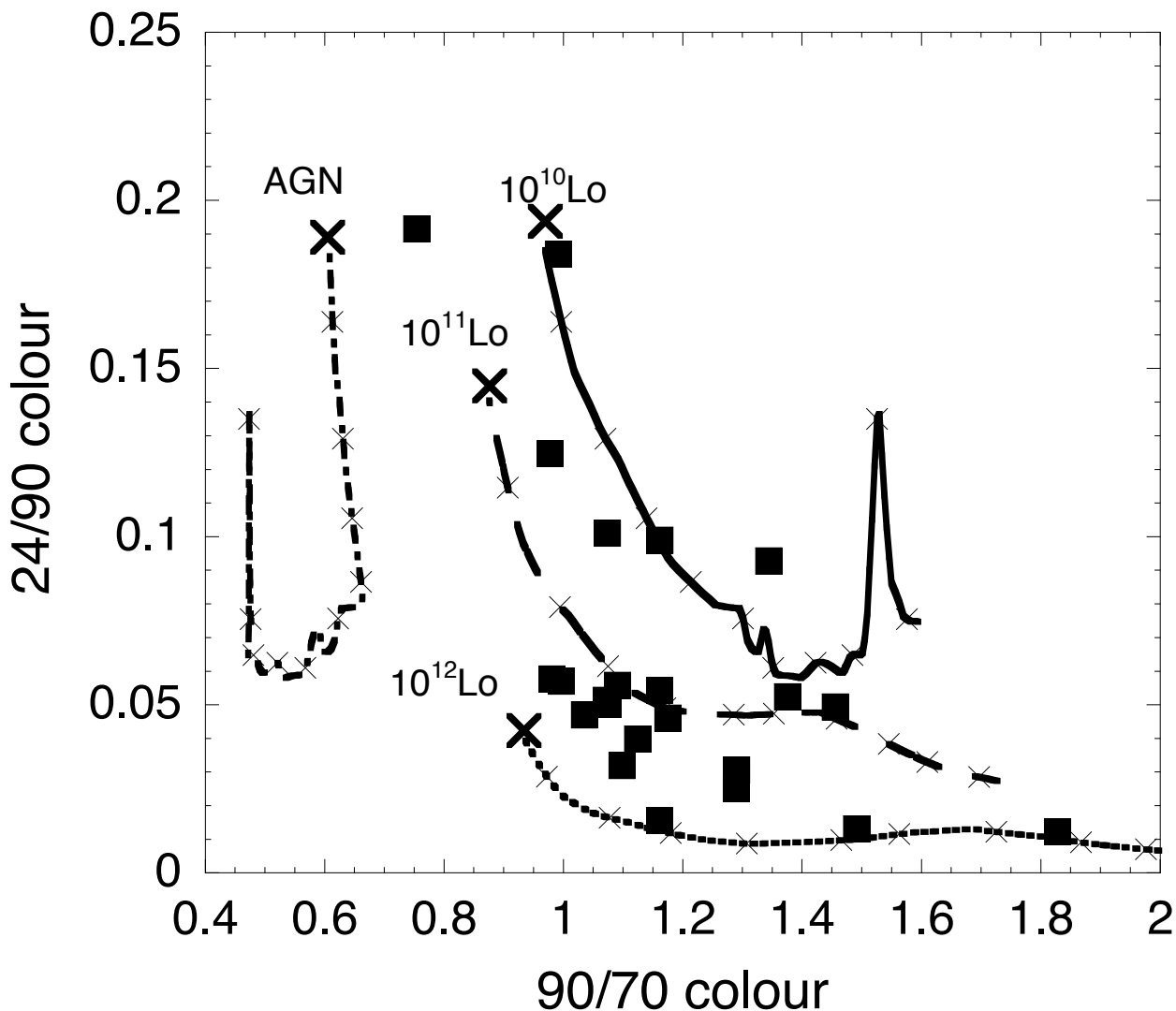
Figure 13. Infrared colours of the sources from our ATCA survey with cross matches in both the AKARI 90 μm and *Spitzer* 24 & 70 μm bands from Table 5. The black squares represent the catalogue sources, with the spectral tracks of an ensemble of star-forming galaxies with increasing far-infrared luminosity from $L_{IR} > 10^{10}L_\odot$, $10^{11}L_\odot$, $10^{12}L_\odot$, and a spectral track from an AGN also plotted. The large crosses show the zero redshift points with the further smaller crosses corresponding to steps in redshift of 0.1.

6.4 Optical identifications

The positions of the components listed in Table 5 were compared with those in the CTIO MOSAIC-II survey (see Table 1), taking a maximum search radius of 1″ (based on the offsets to bright radio sources described in Section 4.3. The number of galaxies as a function of R-magnitude was calculated from the CTIO MOSAIC-II survey, which covers an area of size 1.84×0.64 degrees centred at RA (J2000) = $4^h\ 43^m\ 32.8^s$, Declination (J2000) = $-53°\ 34'51''$. Based on our choice of a radio error box of 1″ search radius, the chance possibility that a 23rd magnitude galaxy (the most numerous in the above plot) should randomly coincide with a radio component is 0.6%. Making an additional correction for the fact that some of the galaxies are extended or saturated, the chance association of a galaxy with a radio component is still $\leq 1\%$.

Postage stamp cutouts for 18″×18″ regions around the sources with CTIO MOSAIC-II matches in Table 5 are shown in Figure 14, where the radio component is located at the centre of each box.

The full radio catalogue (Table 2) was then cross-correlated against the CTIO MOSAIC-II survey, resulting in 95 matches within a search radius of 1″ . To test the false identification rate, arbitrary 60″ offsets were again added to both the RA and Dec coordinates of the radio components, and the cross-match was repeated, resulting in only two galaxies as probably false identifications, which is roughly consistent with out estimate of the likely false detection rate discussed previously. We can therefore be confident to a high degree of the efficacy of our cross identifications. These are shown, along with the (probably false) detections arbitrarily shifting the radio pointing positions, in Figure 15.

The distribution of associated galaxies with magnitude is similar to that found in the CDFS field by Simpson et al. (2006) and Mainieri et al. (2008), with the majority of the number of detections rising from an R-magnitude $\sim$ 17.

6.5 Sub-millimetre cross matches

The ATCA radio catalogue was searched for matches with the ASTE/AzTEC 1.1 mm deep survey (Hatsukade et al. 2011) which contains the locations of 198 potential sub-millimetre galaxies over a $\sim$0.25 degree^2 area. We find one credible match that is consistent with the positional errors, lying 5.5″ from ATCA component 120 with AzTEC J044435.35-534346.6. This has a de-boosted 1.1 mm flux of 2.8±0.5 mJy; a 20 cm radio flux 0.203 mJy; an R-magnitude of 21.4 from our CTIO imaging survey; and is at the highest redshift of 0.825 amongst the ATCA/AKARI detections detected in the AAT AAOmega redshift survey (Sedgwick et al. 2011).

We have also cross-correlated the ATCA catalogue with the BLAST South Ecliptic Pole catalogue (Valiante et al. 2010) finding five cross matched associations within 10″ of a radio position (i.e. searching to one third of the BLAST beam width). These sources, and their 250 μm fluxes are ATCA component numbers 112, 125, 168, 316 and 409 with 250 μm fluxes of 205 mJy, 119 mJy, 177 mJy, 467 mJy and 130 mJy respectively. The first two of these are also listed in Table 5 as having AKARI cross-matches. We have also cross-correlated the ATCA radio sources with the *Herschel*-HerMES Public Data release catalogue, finding 41 cross-matches, the majority confirming our AKARI detections.
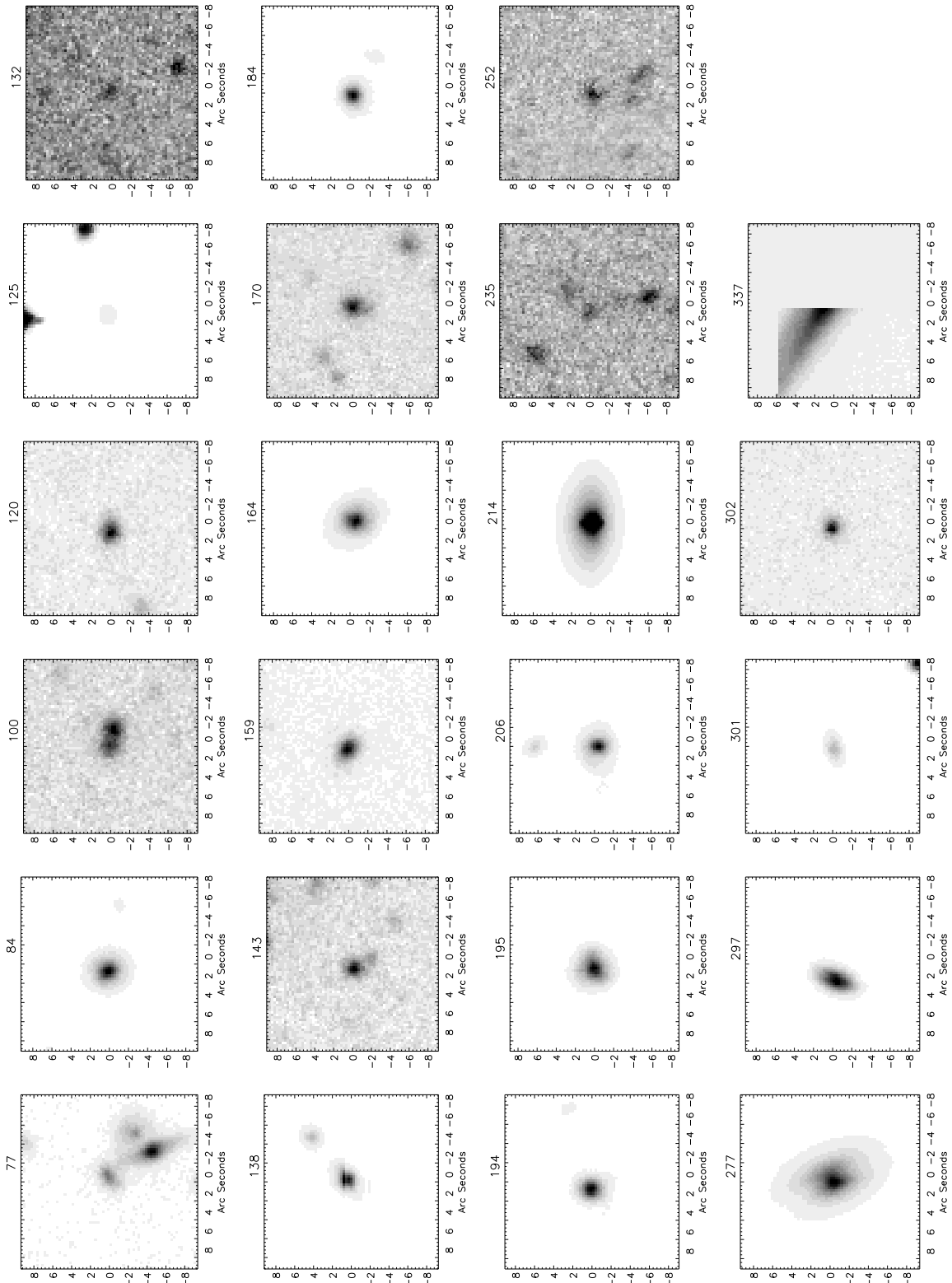
Figure 14. Optically identified radio components from the CTIO MOSAIC-II images. The number on top of each image is the running number of the radio component listed in Table 5. The scaling of each optical image has been adjusted to show the optical galaxy.
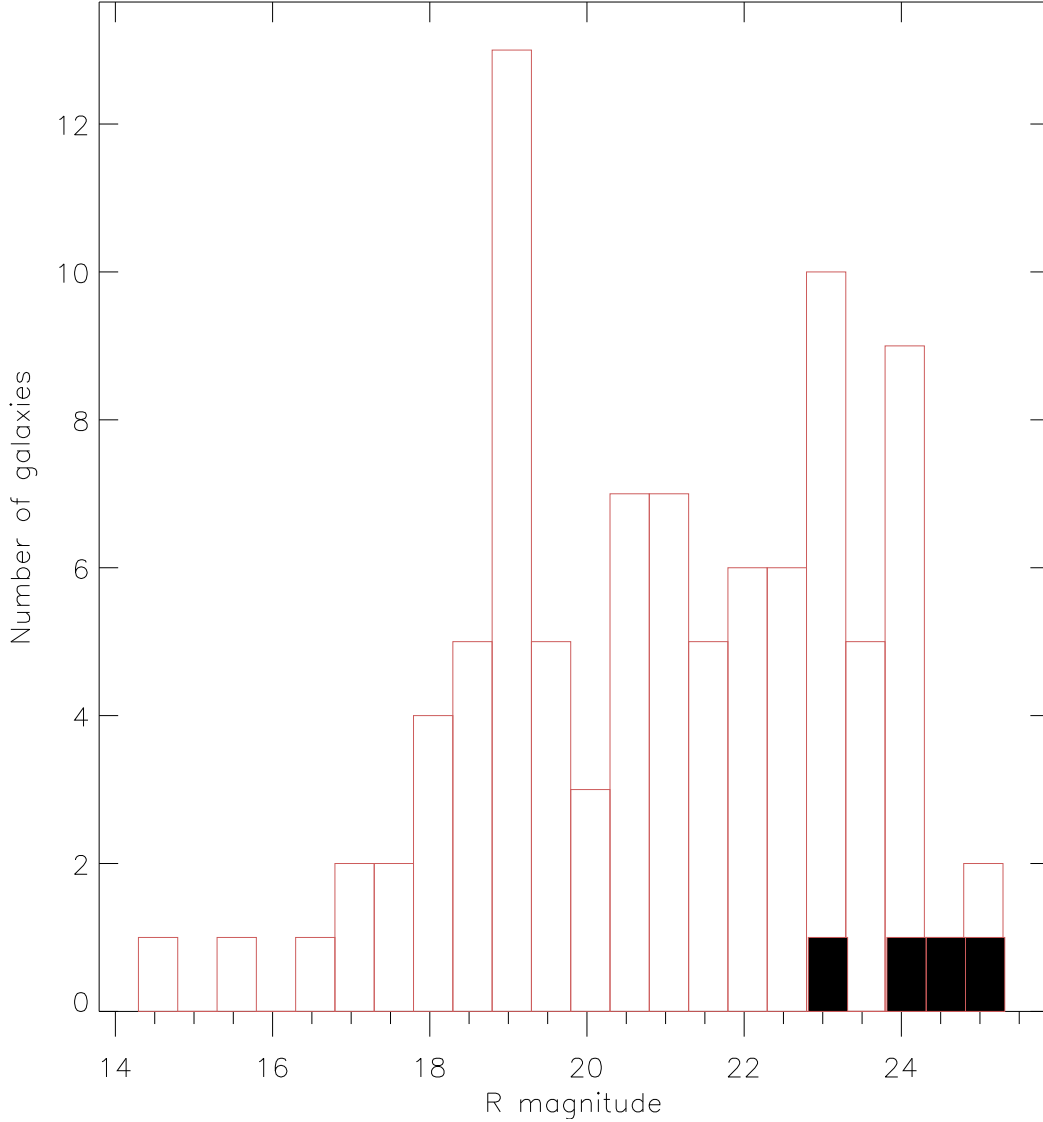
Figure 15. Cross correlation between the ATCA radio components and CTIO MOSAIC-II R-band galaxies within a 1″ search radius. The equivalent counts after arbitrarily shifting the radio coordinates by +60″ in both RA and Dec are shown as the solid filled bars at the bottom right of the Figure, as an indication of the likely false identification rate, which is clearly in line with that expected from the observed density of galaxies in the CTIO MOSAIC-II images.

7 CONCLUSIONS

(i) A deep radio survey has been made of a ~ 1.1 degree^2 area around the ATCA-ADF-S field using the ATCA telescope at 20 cm wavelength, and ~ 2.5 degree^2 to lower sensitivity. The best sensitivity of the survey was 21 μJy beam^{-1}, achieved with a synthesised beam of 6.2″ $\times$ 4.9″. The analysis methodology was carefully chosen to mitigate the various effects that can affect the efficacy of radio synthesis array observations, resulting in a final catalogue of 530 radio components, with the faintest integrated fluxes at about the 100 μJy level. The present catalogue of radio components will form the basis of a further paper reporting cross correlation against extant

AKARI and deep optical imaging. Our derived sub-mJy number counts are consistent with, but lie at the lower end of the emerging picture for the excess in the radio counts below 1 mJy. Fitting an evolving galaxy model to our derived counts, we find a consistent picture of radio-loud dominated sources at bright fluxes and an emerging population of star-forming galaxies at radio flux levels <1 mJy.

(ii) Cross-correlating these with far-infrared sources from AKARI, archival optical photometry, *Spitzer* and BLAST data, we find 51 components lying within $1''$ of a radio position in at least one further catalogue. From optical identifications of a small segment of the radio image, we find 95 cross matches, with most galaxies having R-magnitudes in the range 18-24 magnitudes, similar to that found in other optical deep field identifications. The redshifts of these vary between the local universe and redshifts of up to 0.825. Associating with the *Spitzer* catalogue, we find 173 matches at 24 μm, within one *Spitzer* pixel, of which a small sample are clearly radio loud compared to the bulk of the galaxies.

(iii) The radio luminosity plot suggests that the majority of the radio sources with 90 μm counterparts are luminous star forming galaxies. This conclusion is supported by a comparison of the infrared colours of our matched sources which are well described by the colours expected from star-forming galaxies.

(iv) There is one cross match with an ASTE source, and five cross matches with BLAST sub-millimetre galaxies from the radio sources detected in the present this survey, two of which are also detected also detected at by AKARI at 90 μm, and 41 detections with *Herschel*, of which 12 had not previously been identified by AKARI.

8   ACKNOWLEDGEMENTS

REFERENCES

Appleton, P. N., et al., 2004, ApJS, 154, 147

Bertin E. Arnouts S., 1996, AAS, 117, 393

Bondi, M., Ciliegi, P., Zamorani, G., 2003, A&A, 403, 857

Boyle B.J., Fong R., Shanks T. Peterson, B.A., 1987, MNRAS, 227, 717

Bracco, A., et al., 2011, MNRAS, 412, 1151

Clements, D., Bendo, G., Pearson, C., Khan, Sophia A., Matsuura, S., Shirahata, M., 2011, MN-RAS, 411, 373

Condon, J. J., 1991, in 'The interpretation of modern synthesis observations of spiral galaxies; Proceedings of the Workshop, Albuquerque', ASPC, 115, 1693

Condon, J. J., 1992, ARA&A, 30, 575

Condon, J. J., Cotton, W. D., Greisen, E. W., Yin, Q.F., Perley, R. A.,Taylor, G. B., Broderick, J. J., 1998, AJ, 115, 1693

Condon, J.J., Cotton, W.D., Broderick, J.J., 2002, AJ, 124, 675

Dixon, R.S. 1970, ApJS., 20, 1 (using on-line version 43 from the HEASARC archive `http://heasarc.gsfc.nasa.gov/W3Browse/master-catalog/radio.html`)

Dunlop J.S., Peacock J.A., 1990, MNRAS, 247, 19

Eales, S. et al., 2010, PASP, 122, 499

Efstathiou A., Rowan-Robinson M., Siebenmorgen R., 2000, MNRAS, 313, 734

Efstathiou A., Rowan-Robinson M., 1995, MNRAS, 273, 649

Elvis M., Lockman, F.J., Fassnacht, C., 1994, ApJS, 95, 413

Fomalont, E. B., Kellermann, K. I., Cowie, L. L. Capak, P., Barger, A. J., Partridge, R. B., Windhorst, R. A., Richards, E. A., 2006, ApJS, 167, 103.

Gruppioni, C. et al., 2008, MNRAS, 684, 136

Hajian, A. et al., 2012, ApJ., 744, 40

Hardcastle, M.J., Alexander, P., Pooley, G. G., Riley, J. M., 1998, MNRAS, 296, 445

Hatsukade, B. et al., 2011, MNRAS, 411, 102

Helou G., Soifer T.T., Rowan-Robinson M., 1985, ApJ, 298, 7

Hopkins A.M., Mobasher B., Cram L., Rowan-Robinson, M., 1998, MNRAS, 296, 839

Hopkins, A.M., Miller, C.J., Connolly, A.J., Genovese, C., Nichol, R. C., Wasserman, L., 2002, AJ, 123,1086

Hopkins A.M., Afonso J., Chan B., Cram, L. E., Georgakakis, A., Mobasher, B., 2003, AJ, 125, 465

Hopkins, A. M., 2004, ApJ, 615, 209

Huynh M.T., Jackson C.A., Norris R.P., Prandoni, Isabella., 2005, AJ, 130, 1388

Jarvis, Matt J. et al., 2010, MNRAS, 409, 92

Kawada M., et al., 2007, PASJ, 59, 389

Kollgaard, R.I., Brinkmann, W., Chester, M.M. Margaret Mcmath, Feigelson, Eric D., Hertz, Paul, Reich, Patricia, Wielebinski, Richard., 1994, ApJS, 93, 145

Longair M.S., 1966, MNRAS, 133, 421

Magliocchetti, M., Maddox, S.J., Lahav, O., Wall, J. V., 1998. MNRAS, 300, 257

Mainieri, V., Kellermann, K. I., Fomalont, E. B., Miller, N., 2008, ApJ., 179, 95

Malek, K., Pollo, A., Shirahata, M., Matsuura, S., Kawada, M., Takeuchi, T. T., 2009, 418, 519., AKARI, a Light to Illuminate the Misty Universe ASP Conference Series, Vol. 418, proceedings of a conference held 16-19 February 2009 at the University of Tokyo, Tokyo, Japan. Edited by Takashi Onaka, Glenn J. White, Takao Nakagawa, and Issei Yamamura. San Francisco: Astronomical Society of the Pacific

Malek, K., Pollo, A., Takeuchi, T. T., Bienias, P. Shirahata, M., Matsuura, S., Kawada, M., 2010, A&A, 514, A11

Matsuhara, H. et al., 2006, PASJ, 58, 673

Matsuura, S. et al. 2009, 418, 347., AKARI, a Light to Illuminate the Misty Universe ASP Conference Series, Vol. 418, proceedings of a conference held 16-19 February 2009 at the University of Tokyo, Tokyo, Japan. Edited by Takashi Onaka, Glenn J. White, Takao Nakagawa, and Issei Yamamura. San Francisco: Astronomical Society of the Pacific

Matsuura, S., et al., 2011. ApJ., 737, 2

Mauch,T., Murphy, T., Buttery, H. J., Curran, J., Hunstead, R. W., Piestrzynski, B., Robertson, J. G., Sadler, E. M., 2003. MNRAS, 342, 1117

Mauch, T., Sadler, E., 2007, MNRAS, 375, 931

Middleberg, E., 2006, Pub. Astr. Soc. Australia, 2006, 23, 64

Morganti, R., Garrett, M. A., Chapman, S. Baan, W., Helou, G., Soifer, T., 2004. A&A, 424, 371

Murakami, H., et al., 2007, PASJ, 59, 389

Norris,R.P., et al., 2006, AJ, 132, 2409

Oliver, S. J., Wang, L., Smith, A. J., Altieri, B., 2010. A&A, 518, L21

Owen, F.R. & Morrison, G.E., 2008. AJ, 136, 1889

Oyabu, S., Kawara, K., Tsuzuki, Y., Matsuoka, Y., Sameshima, H., Asami, N., Ohyama, Y., 2009, ApJ., 697, 492

Oyabu, S., et al. 2010. Proc. SPIE 7731, 77312P

Pilbratt, G. L., et al. 2010, A&A, 518, 1

Pearson C.P., 2001, MNRAS, 325, 1511

Pearson C.P., 2005, MNRAS, 358, 1417

Pearson C.P. & Rowan-Robinson M., 1996, MNRAS, 283, 174

Prandoni, I., Gregorini, L., Parma, P. de Ruiter, H. R., Vettolani, G., Wieringa, M. H., Ekers, R. D., 2000a, A&A Suppl, 146, 31

Prandoni, I., Gregorini, L., Parma, P. de Ruiter, H. R., Vettolani, G., Wieringa, M. H., Ekers, R. D., 2000b, A&A Suppl, 146, 41

Rowan-Robinson, M., Phillips, T. G., White, G.J., 1980, MNRAS, 82, 381

Rowan-Robinson M., 1970, MNRAS, 149, 365

Rowan-Robinson, M., Phillips, T. G., White, G.,1980, A&A, 82, 381

Rowan-Robinson M., Benn C.R., Lawrence A. McMahon, R. G., Broadhurst, T. J., 1993, MN-RAS, 263, 123

Sadler,E.M., et al., 2002, MNRAS 329, 227

Sault R.J., Teuben P.J., Wright M.C.H., 1995, *Astronomical Data Analysis Software and Systems IV*, ed. R. Shaw, H.E. Payne, J.J.E. Hayes, ASP Conf. Ser., 77, 433-436

Saunders W., et al., 2000, MNRAS, 317, 55

Schlegel,D.P., Finkbeiner, M., Douglas, P. & Davis, M., 1998, ApJ., 500, 525

Scott, K.S., et al., 2010, ApJS, 191, 212

Sedgwick,C. et al. 2009, 418, 519., AKARI, a Light to Illuminate the Misty Universe ASP Conference Series, Vol. 418, proceedings of a conference held 16-19 February 2009 at the University of Tokyo, Tokyo, Japan. Edited by Takashi Onaka, Glenn J. White, Takao Nakagawa, and Issei Yamamura. San Francisco: Astronomical Society of the Pacific

Sedgwick, C., et al., 2011, MNRAS, 416, 1862

Sedgwick, C. et al. 2012, The Spectral Energy Distribution of Galaxies, Proceedings of the International astronomical Union Symposium, Publishers Cambridge University Press, 284, 289.

Shirahata, M. et al. 2009, 418, 301. AKARI, a Light to Illuminate the Misty Universe ASP Conference Series, Vol. 418, proceedings of a conference held 16-19 February 2009 at the University

of Tokyo, Tokyo, Japan. Edited by Takashi Onaka, Glenn J. White, Takao Nakagawa, and Issei Yamamura. San Francisco: Astronomical Society of the Pacific

Simpson, C., et al., 2006, MNRAS, 372, 741

Swinyard, B.M., Nakagawa, T., Merken, P., Royer, P., et al. 2009, Experimental Astronomy, 23, 193

Valiante, E., et al., 2010, ApJ Suppl, 191, 222

Verdugo, E., et al., 2007, AKARI FIS data user manual, ver. 1.3: (`http://www.sciops.esa.int/SA/ASTROF/docs/FIS\_IDUM\_1.3.pdf`)

Wada, T., et al., 2008, PASJ, 60,517

White, R. L., Becker, R. H., Helfand, D. J., Gregg, Michael D., 1997, ApJ, 475, 479

White, G.J. et al. 2009, 418, 313. AKARI, a Light to Illuminate the Misty Universe ASP Conference Series, Vol. 418, proceedings of a conference held 16-19 February 2009 at the University of Tokyo, Tokyo, Japan. Edited by Takashi Onaka, Glenn J. White, Takao Nakagawa, and Issei Yamamura. San Francisco: Astronomical Society of the Pacific

White, G. J., et al., 2010a, A&A, 517, A54 (Paper 1)

White, G. J., et al., 2010b, CDS source catalogue: J/A+A/517/A54

Windhorst, R.A., Miley G.K., Owen, F.N. Kron, R. G., Koo, D. C., 1985, ApJ, 289, 494

Windhorst R.A., Fomalont E.B., Partridge R.B., Lowenthal, James D., 1993, ApJ, 405, 498

Yamamura, I., Makiuti, S., Ikeda, N., Fukuda, Y, Oyabu, S, Koga, T., White, G. J., 2010, VizieR On-line Data Catalog: 2298, 0.

Yun, M.S., Reddy, N.A., Condon, J.J., 2001, ApJ, 554, 803

Table 7. The complete source catalogue (the full version is available as Supplementary Material in the on line version of this article). The source parameters listed in the catalog are: (1) a short form running number (components that are believed to be parts of multi-component sources are listed with a † sign next to the running number (for example 47†), (2) the source name, referred to in this paper as ATCA-ADFS followed by the RA/Dec encoding (e.g. ATCA-ADFS J045243-533127), (3,4) the source Right Ascension and Declination (J2000) referenced from the self-calibrated reference frame, (5,6) the RA and Dec errors in arc seconds, (7,8) the peak flux density, S_{peak}, and its associated rms error, (9,10) the integrated flux densities, S_{total} and their associated errors, (11, 12, 13) the major and minor axes of the fitted Gaussian source profile and orientation (major and minor axes full width at half maximum, and position angle measured east of north.

No	Source name	RA h:m:s.s	DEC d:m:s.s	ΔRA ″	ΔDEC ″	S_{peak} mJy beam^{-1}	ΔS_{peak} mJy beam^{-1}	S_{total} mJy	ΔS_{total} mJy	θ_{maj} ″	θ_{min} ″	PA °
(1)	(2)	(3)	(4)	(5)	(6)	(7)	(8)	(9)	(10)	(11)	(12)	(13)
1	ATCA-ADFS J044041-534043	4:40:41.5	-53:40:43.5	0.14	0.03	2.951	0.286	7.392	0.368	12.1	2.7	-84.0
2	ATCA-ADFS J044116-532554	4:41:16.4	-53:25:54.0	0.00	0.00	1.498	0.153	4.427	0.206	8.7	6.6	-48.1
3	ATCA-ADFS J044116-531845	4:41:16.9	-53:18:45.8	0.07	0.31	1.568	0.260	5.310	0.317	13.5	3.5	-9.3
4	ATCA-ADFS J044117-531853	4:41:17.9	-53:18:53.5	0.03	0.02	1.866	0.260	2.632	0.274	6.7		-40.6
5	ATCA-ADFS J044120-533214	4:41:20.1	-53:32:14.9	0.03	0.02	1.603	0.116	5.893	0.137	14.1	4.9	-53.8
6	ATCA-ADFS J044120-531626	4:41:20.7	-53:16:26.3	0.79	0.16	1.626	0.260	6.553	0.359	14.8	5.8	-87.5
7	ATCA-ADFS J044121-531637	4:41:21.9	-53:16:37.9	0.17	0.05	1.966	0.260	7.431	0.361	12.6	6.6	-88.1
8	ATCA-ADFS J044122-534349	4:41:22.0	-53:43:49.1	0.01	0.01	0.686	0.096	1.051	0.100			
9	ATCA-ADFS J044123-534402	4:41:23.8	-53:44:02.8	0.07	0.01	0.932	0.096	2.413	0.121	10.3	4.4	-86.0
10	ATCA-ADFS J044124-531600	4:41:24.1	-53:16:00.1	0.32	0.13	1.677	0.260	4.353	0.340	8.6	5.5	86.1
11	ATCA-ADFS J044141-533707	4:41:41.9	-53:37:07.6	0.00	0.00	6.011	0.116	11.775	0.178	7.5	3.6	-80.4
12	ATCA-ADFS J044145-535304	4:41:45.5	-53:53:04.4	0.00	0.00	11.728	0.187	23.327	0.210	8.7	2.0	59.2
13	ATCA-ADFS J044156-531452	4:41:56.5	-53:14:52.4	0.00	0.01	4.390	0.507	10.187	0.521	9.8	2.5	-38.7
14	ATCA-ADFS J044203-534302	4:42:03.9	-53:43:02.1	0.00	0.00	0.639	0.050	0.726	0.050			
15	ATCA-ADFS J044205-533253	4:42:05.0	-53:32:53.3	0.25	0.02	0.356	0.071	1.363	0.074	20.9		-79.4
16	ATCA-ADFS J044208-535941	4:42:08.4	-53:59:41.2	0.41	0.04	0.584	0.080	0.923	0.095	12.2		-73.9
17	ATCA-ADFS J044212-531047	4:42:12.6	-53:10:47.9	0.01	0.03	1.184	0.190	1.974	0.197	6.6		-18.2
18	ATCA-ADFS J044212-535551	4:42:12.6	-53:55:51.6	0.01	0.01	1.374	0.080	2.291	0.087	7.8		47.6
19	ATCA-ADFS J044212-530209	4:42:13.0	-53:02:09.8	0.04	0.11	2.977	0.399	3.947	0.484	6.6		3.7
20	ATCA-ADFS J044213-530802	4:42:13.6	-53:08:02.5	0.06	0.11	1.166	0.190	2.322	0.216	9.4		-23.0
21	ATCA-ADFS J044214-531632	4:42:14.5	-53:16:32.3	0.05	0.06	0.629	0.105	1.949	0.115	11.0	5.0	36.3
22	ATCA-ADFS J044215-530257	4:42:16.0	-53:02:57.8	2.04	0.12	2.132	0.399	10.925	0.505	16.0	7.7	-84.6
23	ATCA-ADFS J044217-530136	4:42:17.5	-53:01:36.7	0.22	0.46	2.491	0.399	8.066	0.500	13.9	3.0	-32.2
24	ATCA-ADFS J044221-533338	4:42:21.4	-53:33:38.5	0.00	0.00	2.091	0.071	3.137	0.081			
25	ATCA-ADFS J044221-535247	4:42:21.6	-53:52:47.8	0.14	0.09	0.381	0.064	0.815	0.074	8.9	2.8	55.9
26	ATCA-ADFS J044222-533800	4:42:22.0	-53:38:00.6	0.01	0.01	0.405	0.062	0.490	0.063			
27	ATCA-ADFS J044226-530145	4:42:26.8	-53:01:45.8	0.00	0.01	2.224	0.399	5.916	0.494	10.8	3.3	-36.8
28	ATCA-ADFS J044231-535716	4:42:31.2	-53:57:16.0	0.07	0.06	0.898	0.080	1.540	0.101	7.5		49.3
29	ATCA-ADFS J044231-533800	4:42:31.2	-53:38:00.8	0.00	0.00	0.276	0.053	0.433	0.054		2.8	-82.2
30	ATCA-ADFS J044232-535228	4:42:32.0	-53:52:28.0	0.08	0.05	0.244	0.058	0.661	0.061	7.7	6.7	69.5
31	ATCA-ADFS J044232-534604	4:42:32.5	-53:46:04.9	0.01	0.01	0.807	0.053	1.278	0.057		2.2	56.2
32	ATCA-ADFS J044241-535307	4:42:41.1	-53:53:07.5	0.00	0.00	0.887	0.080	1.556	0.081	8.4		41.1
33	ATCA-ADFS J044245-533035	4:42:45.7	-53:30:35.6	0.01	0.00	0.485	0.058	0.699	0.059	7.2		-52.6
34	ATCA-ADFS J044245-532957	4:42:45.9	-53:29:57.8	0.07	0.03	0.280	0.056	0.497	0.058		4.1	-87.7
35	ATCA-ADFS J044247-535316	4:42:47.7	-53:53:16.8	0.00	0.01	0.762	0.080	1.052	0.081			
36	ATCA-ADFS J044250-534242	4:42:50.3	-53:42:42.5	0.08	0.04	0.202	0.042	0.383	0.045	7.2	3.3	64.5
37	ATCA-ADFS J044252-533800	4:42:52.6	-53:38:00.9	0.01	0.01	0.253	0.048	0.315	0.049			
38	ATCA-ADFS J044255-540036	4:42:55.8	-54:00:36.9	0.01	0.02	0.990	0.123	1.817	0.124	9.2		28.0
39	ATCA-ADFS J044259-525327	4:42:59.2	-52:53:27.7	0.03	0.03	3.976	0.383	4.167	0.388			
40	ATCA-ADFS J044303-525330	4:43:03.3	-52:53:30.1	0.14	0.20	3.094	0.383	3.274	0.416			
41	ATCA-ADFS J044304-535158	4:43:04.1	-53:51:59.0	0.00	0.01	1.179	0.039	1.466	0.051			
42	ATCA-ADFS J044304-525446	4:43:04.6	-52:54:46.2	0.05	0.43	2.277	0.383	4.691	0.469	12.5		1.4
43	ATCA-ADFS J044305-533538	4:43:05.3	-53:35:38.6	0.00	0.00	2.286	0.060	3.074	0.067			
44	ATCA-ADFS J044305-534634	4:43:05.3	-53:46:34.8	0.00	0.00	1.643	0.039	2.072	0.042			
45	ATCA-ADFS J044305-525549	4:43:05.3	-52:55:49.2	3.32	0.73	4.034	0.383	2.782	0.383			
46	ATCA-ADFS J044308-534105	4:43:08.7	-53:41:05.4	0.00	0.01	0.239	0.033	0.271	0.033			
47†	ATCA-ADFS J044308-533928	4:43:08.8	-53:39:28.1	0.03	0.01	0.532	0.038	0.906	0.043		3.1	-62.1
48	ATCA-ADFS J044308-540537	4:43:08.9	-54:05:37.1	0.01	0.02	1.099	0.123	3.357	0.128	11.9	4.0	31.8
49†	ATCA-ADFS J044309-533931	4:43:09.7	-53:39:31.8	0.07	0.03	0.351	0.038	0.742	0.041	7.6	4.0	-53.9
50	ATCA-ADFS J044313-533458	4:43:13.3	-53:34:58.8	0.00	0.00	63.317	0.060	79.299	0.465			

Table 8. Continuation of the source catalogue

No	Source name	RA h:m:s.s	DEC d:m:s.s	ΔRA ″	ΔDEC ″	S_{peak} mJy beam^{-1}	ΔS_{peak} mJy beam^{-1}	S_{total} mJy	ΔS_{total} mJy	θ_{maj} ″	θ_{min} ″	PA °
(1)	(2)	(3)	(4)	(5)	(6)	(7)	(8)	(9)	(10)	(11)	(12)	(13)
51	ATCA-ADFS J044316-534148	4:43:16.6	-53:41:48.4	0.00	0.00	2.265	0.038	3.040	0.059			
52	ATCA-ADFS J044317-524701	4:43:17.1	-52:47:01.5	0.01	0.01	8.447	1.066	8.516	1.113			
53	ATCA-ADFS J044317-533807	4:43:17.9	-53:38:07.7	0.00	0.00	0.641	0.038	0.851	0.040			
54	ATCA-ADFS J044319-533910	4:43:19.7	-53:39:10.7	0.00	0.00	0.285	0.045	0.352	0.045			
55	ATCA-ADFS J044321-533932	4:43:21.5	-53:39:32.3	0.00	0.00	0.281	0.042	0.317	0.042			
56	ATCA-ADFS J044321-532404	4:43:21.7	-53:24:04.3	0.02	0.02	2.578	0.045	5.960	0.187	7.6	4.7	-23.7
57	ATCA-ADFS J044323-532401	4:43:23.5	-53:24:01.5	0.25	0.04	0.263	0.045	1.325	0.050	14.0	8.6	-72.3
58	ATCA-ADFS J044326-535437	4:43:26.5	-53:54:37.5	0.00	0.00	1.937	0.055	3.137	0.062	6.4		28.2
59	ATCA-ADFS J044327-532350	4:43:27.3	-53:23:50.2	0.04	0.02	1.663	0.045	6.763	0.134	10.7	8.6	-85.0
60	ATCA-ADFS J044330-535405	4:43:30.3	-53:54:05.7	0.01	0.01	0.496	0.055	0.551	0.058			
61	ATCA-ADFS J044331-531822	4:43:31.2	-53:18:22.6	0.04	0.09	0.215	0.060	0.714	0.064	10.7	6.0	9.3
62	ATCA-ADFS J044332-532000	4:43:32.5	-53:20:00.9	0.00	0.01	0.735	0.059	0.962	0.061			
63	ATCA-ADFS J044334-535743	4:43:34.6	-53:57:44.0	0.00	0.00	0.477	0.054	0.335	0.054			
64	ATCA-ADFS J044334-533414	4:43:34.9	-53:34:14.1	0.00	0.00	0.443	0.062	0.459	0.062			
65[†]	ATCA-ADFS J044338-534715	4:43:38.6	-53:47:15.6	0.00	0.00	0.296	0.040	0.344	0.040			
66	ATCA-ADFS J044338-525935	4:43:38.7	-52:59:35.8	0.00	0.00	1.794	0.228	2.174	0.232			
67[†]	ATCA-ADFS J044338-534732	4:43:39.0	-53:47:32.5	0.00	0.00	0.203	0.035	0.177	0.035			
68	ATCA-ADFS J044340-535000	4:43:40.9	-53:50:00.9	0.03	0.06	1.834	0.039	4.059	0.155	9.1	2.3	-29.0
69[†]	ATCA-ADFS J044343-532222	4:43:43.0	-53:22:22.7	0.01	0.03	0.295	0.047	0.511	0.050	8.1		-7.0
70[†]	ATCA-ADFS J044343-532213	4:43:43.7	-53:22:13.6	0.00	0.00	0.398	0.047	0.540	0.047	6.8		-5.3
71	ATCA-ADFS J044344-535722	4:43:44.7	-53:57:22.6	0.02	0.07	0.278	0.041	0.578	0.044	10.0		7.2
72	ATCA-ADFS J044345-533535	4:43:45.4	-53:35:35.3	0.01	0.01	0.201	0.030	0.257	0.031			
73	ATCA-ADFS J044352-524820	4:43:52.2	-52:48:21.0	0.00	0.00	3.735	0.401	2.878	0.402			
74	ATCA-ADFS J044352-525142	4:43:53.0	-52:51:42.5	0.02	0.02	2.607	0.401	4.701	0.416	6.8	2.6	-43.8
75	ATCA-ADFS J044353-530240	4:43:53.6	-53:02:40.2	0.02	0.04	2.697	0.093	9.588	0.176	15.1	3.1	-27.9
76	ATCA-ADFS J044354-533829	4:43:54.2	-53:38:29.4	0.00	0.00	0.259	0.030	0.332	0.030			
77	ATCA-ADFS J044354-532112	4:43:54.9	-53:21:12.8	0.02	0.03	0.277	0.040	0.419	0.043			
78	ATCA-ADFS J044355-534527	4:43:55.2	-53:45:27.8	0.00	0.00	0.195	0.029	0.229	0.029			
79	ATCA-ADFS J044355-531626	4:43:55.3	-53:16:26.1	0.00	0.01	0.433	0.040	0.636	0.041			
80	ATCA-ADFS J044355-535634	4:43:55.7	-53:56:34.1	0.00	0.00	1.577	0.041	2.031	0.049			
81	ATCA-ADFS J044356-524739	4:43:56.0	-52:47:39.5	0.05	0.06	2.453	0.401	4.143	0.434	6.9		-24.4
82	ATCA-ADFS J044356-532307	4:43:56.6	-53:23:07.7	0.00	0.00	0.412	0.040	0.469	0.040			
83	ATCA-ADFS J044357-533739	4:43:57.8	-53:37:39.3	0.01	0.02	0.207	0.030	0.321	0.032			
84	ATCA-ADFS J044359-533034	4:43:59.7	-53:30:34.6	0.02	0.04	0.228	0.031	0.234	0.032			
85	ATCA-ADFS J040440-525110	4:044:0.5	-52:51:10.4	0.00	0.00	44.456	0.401	86.987	0.606	8.5		-36.7
86	ATCA-ADFS J044405-533315	4:44:05.8	-53:33:15.7	0.00	0.00	0.392	0.030	0.396	0.030			
87	ATCA-ADFS J044406-533927	4:44:06.3	-53:39:27.1	0.00	0.00	0.350	0.030	0.394	0.030			
88	ATCA-ADFS J044406-533400	4:44:06.4	-53:34:00.1	0.00	0.01	0.255	0.029	0.144	0.029			
89	ATCA-ADFS J044407-534637	4:44:07.2	-53:46:37.8	0.01	0.02	0.170	0.027	0.208	0.027			
90	ATCA-ADFS J044408-530643	4:44:08.4	-53:06:43.2	0.01	0.01	1.327	0.093	2.691	0.103	9.2		-18.4
91	ATCA-ADFS J044408-534044	4:44:08.7	-53:40:44.1	0.00	0.00	0.448	0.030	0.421	0.030			
92	ATCA-ADFS J044409-532858	4:44:09.5	-53:28:58.2	0.00	0.00	0.260	0.031	0.334	0.031			
93	ATCA-ADFS J044410-533325	4:44:10.3	-53:33:25.5	0.00	0.00	0.293	0.029	0.129	0.029			
94	ATCA-ADFS J044412-533708	4:44:12.8	-53:37:08.9	0.00	0.00	2.848	0.030	3.378	0.041			
95	ATCA-ADFS J044413-525347	4:44:13.0	-52:53:47.8	6.18	2.08	1.617	0.168	1.250	0.169			
96	ATCA-ADFS J044413-534507	4:44:13.9	-53:45:07.8	0.00	0.00	0.319	0.030	0.360	0.030			
97	ATCA-ADFS J044415-530531	4:44:15.5	-53:05:31.0	0.01	0.04	0.884	0.093	1.521	0.109	8.9		-20.0
98	ATCA-ADFS J044417-533833	4:44:17.3	-53:38:33.4	0.00	0.01	0.219	0.030	0.215	0.030			
99[†]	ATCA-ADFS J044417-532435	4:44:17.8	-53:24:35.1	0.02	0.01	2.996	0.031	9.352	0.185	10.5	5.8	-65.8
100	ATCA-ADFS J044418-534632	4:44:18.4	-53:46:32.6	0.00	0.00	0.421	0.030	0.476	0.030			

Table 9. Continuation of the source catalogue

No	Source name	RA h:m:s.s	DEC d:m:s.s	ΔRA ″	ΔDEC ″	S_{peak} mJy beam^{-1}	ΔS_{peak} mJy beam^{-1}	S_{total} mJy	ΔS_{total} mJy	θ_{maj} ″	θ_{min} ″	PA °
(1)	(2)	(3)	(4)	(5)	(6)	(7)	(8)	(9)	(10)	(11)	(12)	(13)
101	ATCA-ADFS J044419-535132	4:44:19.3	-53:51:32.7	0.00	0.01	0.224	0.032	0.239	0.032			
102†	ATCA-ADFS J044419-532442	4:44:19.9	-53:24:42.7	0.07	0.04	2.513	0.031	9.265	0.241	12.9	5.9	-55.1
103	ATCA-ADFS J044420-534032	4:44:20.8	-53:40:32.8	0.01	0.01	0.178	0.030	0.197	0.030			
104	ATCA-ADFS J044421-534006	4:44:21.2	-53:40:06.6	0.09	0.05	0.129	0.030	0.312	0.032	8.8	4.8	-79.0
105	ATCA-ADFS J044421-534135	4:44:21.4	-53:41:35.4	0.02	0.06	0.420	0.030	0.674	0.040	7.7		13.2
106	ATCA-ADFS J044422-531407	4:44:22.1	-53:14:07.1	0.00	0.01	0.553	0.056	0.789	0.057			
107	ATCA-ADFS J044422-534251	4:44:22.2	-53:42:51.6	0.05	0.06	0.144	0.030	0.148	0.032			
108	ATCA-ADFS J044425-533732	4:44:25.9	-53:37:32.2	0.00	0.00	0.193	0.034	0.235	0.034			
109	ATCA-ADFS J044428-534728	4:44:28.4	-53:47:28.5	0.00	0.00	0.208	0.031	0.248	0.031			
110	ATCA-ADFS J044430-540457	4:44:30.9	-54:04:57.5	0.00	0.00	1.971	0.080	3.529	0.090	9.3		-7.0
111	ATCA-ADFS J044431-535420	4:44:32.0	-53:54:20.2	0.00	0.00	0.261	0.034	0.319	0.034			
112	ATCA-ADFS J044432-540544	4:44:32.0	-54:05:44.8	0.02	0.04	0.681	0.083	0.890	0.094			
113	ATCA-ADFS J044432-530604	4:44:32.1	-53:06:04.9	0.00	0.00	0.847	0.093	1.332	0.093	6.2		-19.3
114	ATCA-ADFS J044432-532237	4:44:32.5	-53:22:37.5	0.01	0.02	0.178	0.035	0.197	0.035			
115	ATCA-ADFS J044433-535234	4:44:33.0	-53:52:34.1	0.00	0.00	1.431	0.030	1.600	0.034			
116	ATCA-ADFS J044433-524317	4:44:33.7	-52:43:17.1	0.02	0.04	6.883	1.151	16.162	1.196	10.3		-35.7
117	ATCA-ADFS J044433-535036	4:44:33.7	-53:50:36.8	0.00	0.00	7.727	0.030	9.242	0.095			
118	ATCA-ADFS J044434-535516	4:44:34.5	-53:55:16.2	0.00	0.00	2.096	0.044	2.565	0.049			
119	ATCA-ADFS J044434-534949	4:44:34.6	-53:49:49.5	0.01	0.01	0.160	0.030	0.181	0.030			
120	ATCA-ADFS J044434-534346	4:44:34.7	-53:43:46.3	0.01	0.01	0.213	0.033	0.203	0.033			
121	ATCA-ADFS J044435-530533	4:44:35.2	-53:05:33.5	0.00	0.00	1.169	0.093	2.333	0.098	9.9		-13.1
122†	ATCA-ADFS J044435-533604	4:44:35.6	-53:36:04.3	0.05	0.11	0.449	0.027	0.834	0.043	8.2		10.0
123†	ATCA-ADFS J044436-533558	4:44:36.2	-53:35:58.4	0.05	0.04	0.303	0.027	0.681	0.030	7.5	4.4	21.6
124	ATCA-ADFS J044436-534522	4:44:36.7	-53:45:22.2	0.00	0.00	1.734	0.027	1.638	0.033			
125	ATCA-ADFS J044436-534632	4:44:36.7	-53:46:32.2	0.00	0.00	0.302	0.030	0.415	0.030			
126	ATCA-ADFS J044437-524346	4:44:37.3	-52:43:47.0	0.00	0.00	12.943	1.151	34.043	1.242	11.1	2.6	-29.2
127	ATCA-ADFS J044437-533655	4:44:37.7	-53:36:55.3	0.00	0.00	0.244	0.033	0.230	0.033			
128	ATCA-ADFS J044437-533325	4:44:37.7	-53:33:25.9	0.00	0.00	0.343	0.027	0.365	0.027			
129	ATCA-ADFS J044439-540524	4:44:39.1	-54:05:24.3	0.00	0.01	1.356	0.083	2.549	0.093	10.2		-5.7
130	ATCA-ADFS J044439-530617	4:44:39.7	-53:06:17.3	0.00	0.01	0.510	0.023	0.510	0.023			
131	ATCA-ADFS J044441-530441	4:44:41.3	-53:04:41.3	0.02	0.06	0.459	0.027	0.459	0.027			
132	ATCA-ADFS J044441-532112	4:44:41.9	-53:21:12.7	0.06	0.08	0.289	0.033	0.257	0.033			
133	ATCA-ADFS J044443-533859	4:44:43.3	-53:38:59.3	0.00	0.00	0.126	0.031	0.154	0.031			
134	ATCA-ADFS J044445-533858	4:44:45.8	-53:38:58.0	3.21	0.00	0.130	0.030	0.114	0.030			
135	ATCA-ADFS J044446-532244	4:44:46.0	-53:22:44.4	0.00	0.01	0.160	0.034	0.234	0.034			
136	ATCA-ADFS J044446-524619	4:44:46.3	-52:46:19.9	0.02	0.02	1.612	0.204	2.271	0.207	6.5		-30.5
137	ATCA-ADFS J044450-533856	4:44:50.4	-53:38:56.3	0.00	0.00	2.972	0.027	3.047	0.035			
138	ATCA-ADFS J044451-532713	4:44:51.4	-53:27:13.9	0.00	0.00	0.285	0.028	0.464	0.028	7.3		8.6
139	ATCA-ADFS J044451-535751	4:44:51.6	-53:57:51.3	0.01	0.01	0.329	0.049	0.383	0.050			
140†	ATCA-ADFS J044453-534057	4:44:53.1	-53:40:57.6	0.01	0.00	1.467	0.027	2.338	0.033		3.3	-60.8
141†	ATCA-ADFS J044453-534103	4:44:53.7	-53:41:03.2	0.01	0.02	2.376	0.027	4.611	0.113	8.7		-20.2
142	ATCA-ADFS J044455-531423	4:44:55.2	-53:14:23.4	0.00	0.02	0.183	0.027	0.183	0.027			
143	ATCA-ADFS J044455-533405	4:44:55.4	-53:34:05.7	0.00	0.00	0.285	0.027	0.381	0.027			
144	ATCA-ADFS J044456-532346	4:44:56.1	-53:23:46.9	0.02	0.02	0.139	0.028	0.164	0.029			
145	ATCA-ADFS J044456-532608	4:44:56.3	-53:26:08.1	0.00	0.00	0.255	0.028	0.283	0.028			
146	ATCA-ADFS J044456-531530	4:44:56.8	-53:15:30.7	0.02	0.02	0.199	0.037	0.401	0.038	6.3	4.4	16.2
147	ATCA-ADFS J044457-535549	4:44:57.7	-53:55:49.9	0.00	0.00	0.520	0.044	0.630	0.046			
148	ATCA-ADFS J044459-535457	4:44:59.0	-53:54:57.2	0.00	0.00	0.246	0.036	0.273	0.036			
149	ATCA-ADFS J040450-533449	4:045:0.8	-53:34:49.4	0.00	0.00	1.079	0.027	1.237	0.029			
150	ATCA-ADFS J044503-525332	4:45:03.9	-52:53:32.1	0.01	0.01	1.804	0.204	3.678	0.209	8.6		-20.6

Table 10. Continuation of the source catalogue

No	Source name	RA h:m:s.s	DEC d:m:s.s	ΔRA ″	ΔDEC ″	S_{peak} mJy beam^{-1}	ΔS_{peak} mJy beam^{-1}	S_{total} mJy	ΔS_{total} mJy	θ_{maj} ″	θ_{min} ″	PA °
(1)	(2)	(3)	(4)	(5)	(6)	(7)	(8)	(9)	(10)	(11)	(12)	(13)
151	ATCA-ADFS J044504-531756	4:45:04.6	-53:17:56.5	1.11	0.08	0.211	0.032	0.133	0.032			
152	ATCA-ADFS J044504-525431	4:45:04.9	-52:54:31.9	0.01	0.02	0.629	0.100	1.304	0.103	7.8	2.8	0.3
153	ATCA-ADFS J044506-531726	4:45:06.9	-53:17:26.8	0.00	0.01	0.191	0.032	0.265	0.032	7.5		-4.6
154	ATCA-ADFS J044507-525423	4:45:07.6	-52:54:23.8	0.00	0.00	6.554	0.100	10.806	0.126	6.8		-24.2
155	ATCA-ADFS J044508-541153	4:45:08.1	-54:11:53.3	0.00	0.01	11.230	0.274	25.146	0.396	11.7		-13.0
156	ATCA-ADFS J044508-533835	4:45:08.6	-53:38:35.7	0.00	0.02	0.205	0.027	0.205	0.027			
157	ATCA-ADFS J044508-525818	4:45:08.7	-52:58:18.6	0.01	0.01	1.106	0.100	2.262	0.105	9.2		-25.3
158	ATCA-ADFS J044508-535021	4:45:08.9	-53:50:21.9	0.01	0.04	0.147	0.031	0.271	0.031	9.4		-10.3
159	ATCA-ADFS J044509-533751	4:45:09.7	-53:37:51.4	0.00	0.00	0.156	0.023	0.210	0.023			
160	ATCA-ADFS J044512-540511	4:45:12.6	-54:05:11.4	0.00	0.00	6.211	0.083	10.826	0.161	9.1		-16.7
161	ATCA-ADFS J044513-530633	4:45:13.7	-53:06:33.9	0.00	0.00	0.600	0.063	0.825	0.063			
162	ATCA-ADFS J044516-540332	4:45:16.9	-54:03:32.4	0.05	0.13	0.342	0.080	0.727	0.085	9.2		-3.8
163	ATCA-ADFS J044518-531643	4:45:18.1	-53:16:43.4	0.00	0.00	0.912	0.033	1.099	0.037			
164	ATCA-ADFS J044518-535119	4:45:18.3	-53:51:19.8	0.01	0.01	0.155	0.033	0.258	0.034	7.6		-31.6
165	ATCA-ADFS J044518-540631	4:45:18.5	-54:06:31.1	0.02	0.07	1.650	0.083	2.999	0.137	10.1		-18.4
166[†]	ATCA-ADFS J044518-531231	4:45:18.5	-53:12:31.0	0.00	0.00	0.492	0.042	0.705	0.042	6.3		-1.4
167	ATCA-ADFS J044518-523853	4:45:18.7	-52:38:53.4	0.01	0.01	4.669	0.581	7.379	0.598	8.8		-34.6
168	ATCA-ADFS J044519-531045	4:45:19.5	-53:10:45.6	0.00	0.00	0.215	0.038	0.273	0.038			
169[†]	ATCA-ADFS J044520-531221	4:45:20.0	-53:12:21.4	0.01	0.06	0.178	0.035	0.370	0.036	9.9		-13.2
170	ATCA-ADFS J044520-532010	4:45:20.1	-53:20:10.3	0.01	0.02	0.262	0.033	0.312	0.033			
171[†]	ATCA-ADFS J044521-530918	4:45:21.1	-53:09:18.6	0.01	0.01	0.155	0.041	0.246	0.041	7.0		-14.6
172[†]	ATCA-ADFS J044522-530853	4:45:22.2	-53:08:53.4	0.00	0.00	0.379	0.042	0.588	0.042	6.7		-18.4
173	ATCA-ADFS J044522-532644	4:45:22.8	-53:26:44.5	0.00	0.00	0.164	0.025	0.180	0.025			
174	ATCA-ADFS J044523-530910	4:45:23.1	-53:09:10.4	0.31	0.15	0.160	0.041	0.335	0.046	7.6	4.0	63.2
175[†]	ATCA-ADFS J044523-530430	4:45:23.5	-53:04:30.8	0.00	0.00	0.280	0.053	0.386	0.053			
176	ATCA-ADFS J044523-530914	4:45:23.9	-53:09:14.9	0.00	0.01	0.258	0.041	0.284	0.041			
177	ATCA-ADFS J044524-531844	4:45:24.2	-53:18:44.2	0.00	0.00	0.752	0.033	0.943	0.034			
178	ATCA-ADFS J044524-530609	4:45:24.9	-53:06:09.4	0.00	0.02	0.171	0.026	0.171	0.026			
179[†]	ATCA-ADFS J044525-530509	4:45:25.8	-53:05:10.0	0.00	0.00	0.616	0.063	0.742	0.063			
180[†]	ATCA-ADFS J044526-530607	4:45:26.6	-53:06:07.1	0.00	0.00	0.261	0.056	0.422	0.057	6.3		35.7
181	ATCA-ADFS J044527-535318	4:45:27.3	-53:53:18.5	0.03	0.03	0.253	0.041	0.318	0.044			
182	ATCA-ADFS J044527-531153	4:45:27.6	-53:11:53.7	0.00	0.00	0.388	0.036	0.581	0.036			
183	ATCA-ADFS J044527-533930	4:45:28.0	-53:39:30.3	0.00	0.00	10.459	0.035	15.530	0.194			
184	ATCA-ADFS J044530-532131	4:45:30.4	-53:21:31.5	0.00	0.00	0.307	0.034	0.457	0.034	6.4		-1.2
185	ATCA-ADFS J044531-524044	4:45:31.4	-52:40:45.0	0.10	0.21	2.332	0.392	4.700	0.468	10.1		-23.5
186	ATCA-ADFS J044532-540422	4:45:32.1	-54:04:22.6	0.01	0.03	0.866	0.123	1.551	0.132	8.3		-20.2
187	ATCA-ADFS J044532-540210	4:45:32.6	-54:02:10.1	0.00	0.00	5.219	0.123	8.675	0.159	8.7		-24.9
188	ATCA-ADFS J044533-540429	4:45:33.6	-54:04:29.3	0.01	0.02	1.946	0.123	3.921	0.149	9.5		-27.3
189	ATCA-ADFS J044534-532414	4:45:34.3	-53:24:14.9	0.01	0.01	0.145	0.031	0.247	0.031	6.4	2.9	11.4
190	ATCA-ADFS J044535-533850	4:45:35.7	-53:38:50.3	0.00	0.00	0.176	0.033	0.362	0.033	6.5	4.6	52.4
191	ATCA-ADFS J044536-535557	4:45:36.6	-53:55:57.0	0.01	0.02	0.341	0.058	0.491	0.059	7.3		-32.9
192	ATCA-ADFS J044537-534939	4:45:37.2	-53:49:39.5	0.00	0.00	0.418	0.038	0.552	0.038			
193	ATCA-ADFS J044537-533829	4:45:37.5	-53:38:29.8	0.00	0.00	0.219	0.033	0.296	0.033			
194	ATCA-ADFS J044538-534726	4:45:38.6	-53:47:26.8	0.00	0.00	0.380	0.038	0.510	0.038			
195	ATCA-ADFS J044541-535246	4:45:41.1	-53:52:46.1	0.01	0.02	0.364	0.038	0.492	0.039			
196	ATCA-ADFS J044541-531132	4:45:41.8	-53:11:32.8	0.00	0.01	0.231	0.027	0.304	0.027			
197	ATCA-ADFS J044544-534430	4:45:44.6	-53:44:30.7	0.00	0.00	1.167	0.035	1.428	0.036			
198	ATCA-ADFS J044547-530108	4:45:47.7	-53:01:08.1	0.00	0.00	0.667	0.077	1.158	0.077	6.5	2.0	-23.5
199	ATCA-ADFS J044549-533916	4:45:49.8	-53:39:16.2	0.00	0.00	0.320	0.035	0.402	0.035			
200	ATCA-ADFS J044553-531231	4:45:53.7	-53:12:32.0	0.19	0.48	0.107	0.037	0.609	0.039	18.9	6.4	23.7

Table 11. Continuation of the source catalogue

No	Source name	RA h:m:s.s	DEC d:m:s.s	ΔRA ″	ΔDEC ″	S_{peak} mJy beam^{-1}	ΔS_{peak} mJy beam^{-1}	S_{total} mJy	ΔS_{total} mJy	θ_{maj} ″	θ_{min} ″	PA °
(1)	(2)	(3)	(4)	(5)	(6)	(7)	(8)	(9)	(10)	(11)	(12)	(13)
200	ATCA-ADFS J044553-531231	4:45:53.7	-53:12:32.0	0.19	0.48	0.107	0.037	0.609	0.039	18.9	6.4	23.7
201	ATCA-ADFS J044554-533522	4:45:54.1	-53:35:22.4	0.00	0.00	2.729	0.031	3.294	0.038			
202	ATCA-ADFS J044554-534203	4:45:54.4	-53:42:03.6	0.01	0.01	0.150	0.036	0.293	0.036	7.6	2.7	-45.5
203	ATCA-ADFS J044554-533817	4:45:54.7	-53:38:17.9	0.00	0.00	0.359	0.031	0.361	0.031			
204	ATCA-ADFS J044555-535951	4:45:55.4	-53:59:51.2	0.00	0.00	0.813	0.058	1.091	0.059			
205	ATCA-ADFS J044555-534001	4:45:55.4	-53:40:01.7	0.00	0.03	0.201	0.031	0.201	0.031			
206	ATCA-ADFS J044556-531633	4:45:56.0	-53:16:33.8	0.00	0.00	0.773	0.034	0.952	0.035			
207	ATCA-ADFS J044557-531304	4:45:57.9	-53:13:04.6	0.02	0.05	0.145	0.037	0.395	0.038	10.0	4.1	-14.3
208	ATCA-ADFS J044558-532101	4:45:58.5	-53:21:01.3	0.00	0.00	0.390	0.034	0.505	0.035			
209	ATCA-ADFS J040460-533624	4:046:0.4	-53:36:24.5	0.00	0.00	0.707	0.031	0.841	0.033			
210	ATCA-ADFS J044601-531837	4:46:01.1	-53:18:37.1	0.00	0.02	0.189	0.028	0.172	0.028			
211	ATCA-ADFS J044601-525350	4:46:01.3	-52:53:50.4	0.00	0.00	1.032	0.103	0.541	0.104			
212†	ATCA-ADFS J044602-534438	4:46:02.3	-53:44:38.3	0.02	0.03	0.150	0.036	0.258	0.037		3.4	43.4
213†	ATCA-ADFS J044604-534444	4:46:04.0	-53:44:44.9	0.01	0.01	0.152	0.036	0.211	0.036			
214	ATCA-ADFS J044605-534955	4:46:05.3	-53:49:55.9	0.00	0.00	0.546	0.043	0.276	0.043			
215	ATCA-ADFS J044606-525438	4:46:06.1	-52:54:38.9	0.00	0.00	0.976	0.077	1.373	0.078			
216	ATCA-ADFS J044606-535634	4:46:06.4	-53:56:34.7	0.00	0.01	0.354	0.062	0.506	0.063	6.7		-17.4
217	ATCA-ADFS J044607-530442	4:46:07.9	-53:04:42.0	0.00	0.00	0.443	0.048	0.594	0.048			
218	ATCA-ADFS J044608-535811	4:46:08.8	-53:58:11.8	0.00	0.00	0.588	0.058	0.731	0.058			
219	ATCA-ADFS J044610-533716	4:46:10.0	-53:37:16.9	0.00	0.00	0.400	0.031	0.505	0.031			
220	ATCA-ADFS J044614-530741	4:46:14.2	-53:07:42.0	0.00	0.00	0.195	0.036	0.216	0.036			
221	ATCA-ADFS J044614-532319	4:46:14.3	-53:23:19.1	0.00	0.00	0.905	0.034	0.839	0.036			
222	ATCA-ADFS J044614-535407	4:46:14.8	-53:54:07.3	0.00	0.00	2.780	0.096	5.077	0.102	7.6		-40.5
223†	ATCA-ADFS J044615-533919	4:46:15.8	-53:39:19.6	0.00	0.00	22.492	0.051	45.194	0.652	6.7	4.1	9.6
224†	ATCA-ADFS J044617-533924	4:46:17.3	-53:39:24.2	0.01	0.01	11.846	0.051	22.070	0.562		4.0	-49.5
225	ATCA-ADFS J044617-531156	4:46:17.5	-53:11:56.5	0.00	0.01	0.154	0.029	0.177	0.029			
226	ATCA-ADFS J044617-531919	4:46:18.0	-53:19:19.6	0.00	0.00	0.297	0.041	0.305	0.041			
227†	ATCA-ADFS J044620-525617	4:46:20.0	-52:56:17.5	0.00	0.00	20.759	0.064	40.815	0.559	8.5		-8.1
228†	ATCA-ADFS J044620-525630	4:46:20.5	-52:56:30.1	0.01	0.04	11.333	0.064	24.243	0.693	9.1		-15.6
229	ATCA-ADFS J044621-531244	4:46:21.3	-53:12:44.5	0.01	0.01	0.270	0.032	0.279	0.033			
230	ATCA-ADFS J044621-535001	4:46:21.9	-53:50:01.6	0.01	0.01	0.292	0.049	0.322	0.050			
231	ATCA-ADFS J044622-524104	4:46:22.1	-52:41:04.3	8.27	1.67	2.601	0.324	3.619	0.329	13.9		0.8
232	ATCA-ADFS J044622-532725	4:46:22.7	-53:27:25.7	0.00	0.00	0.571	0.034	0.586	0.035			
233	ATCA-ADFS J044623-532549	4:46:23.2	-53:25:49.5	0.00	0.00	5.402	0.034	7.158	0.081			
234	ATCA-ADFS J044623-535123	4:46:23.4	-53:51:23.3	0.00	0.01	0.450	0.061	0.670	0.062			
235	ATCA-ADFS J044626-534942	4:46:26.6	-53:49:42.9	0.00	0.01	0.572	0.061	0.942	0.062	6.6		-20.9
236	ATCA-ADFS J044629-532004	4:46:29.5	-53:20:04.2	0.00	0.00	27.077	0.042	28.928	0.241			
237	ATCA-ADFS J044630-532854	4:46:30.3	-53:28:54.0	0.00	0.00	0.908	0.034	0.958	0.035			
238†	ATCA-ADFS J044631-534655	4:46:31.6	-53:46:55.4	0.00	0.00	10.910	0.061	20.590	0.249	6.7	3.4	-41.9
239	ATCA-ADFS J044632-530332	4:46:32.5	-53:03:32.6	0.00	0.02	0.197	0.031	0.197	0.031			
240†	ATCA-ADFS J044632-534702	4:46:33.0	-53:47:02.2	0.00	0.00	7.419	0.061	28.037	0.421	14.7	5.1	-68.3
241†	ATCA-ADFS J044633-534704	4:46:33.5	-53:47:05.0	0.02	0.01	10.250	0.061	23.175	0.500	8.0	4.4	-55.2
242	ATCA-ADFS J044634-531115	4:46:34.1	-53:11:15.7	0.00	0.00	0.306	0.033	0.366	0.033			
243	ATCA-ADFS J044637-531026	4:46:37.3	-53:10:26.7	0.00	0.00	3.340	0.033	4.117	0.042			
244	ATCA-ADFS J044638-533251	4:46:38.8	-53:32:51.0	0.00	0.00	0.349	0.040	0.450	0.040			
245	ATCA-ADFS J044639-525544	4:46:39.5	-52:55:44.8	0.00	0.00	0.557	0.064	0.702	0.064			
246	ATCA-ADFS J044641-540925	4:46:41.1	-54:09:25.9	0.01	0.02	12.401	0.564	32.397	0.690	13.7		-33.2
247	ATCA-ADFS J044641-534716	4:46:41.4	-53:47:16.2	0.00	0.00	0.732	0.061	1.002	0.061			
248†	ATCA-ADFS J044642-530146	4:46:42.6	-53:01:46.4	0.00	0.00	4.213	0.037	5.786	0.054			
249	ATCA-ADFS J044642-532614	4:46:42.7	-53:26:14.8	0.00	0.00	0.476	0.034	0.441	0.034			
250†	ATCA-ADFS J044642-531806	4:46:42.9	-53:18:06.9	0.01	0.01	2.176	0.042	3.662	0.106	7.6	2.2	33.8

Table 12. Continuation of the source catalogue

No	Source name	RA h:m:s.s	DEC d:m:s.s	ΔRA ″	ΔDEC ″	S_{peak} mJy beam^{-1}	ΔS_{peak} mJy beam^{-1}	S_{total} mJy	ΔS_{total} mJy	θ_{maj} ″	θ_{min} ″	PA °
(1)	(2)	(3)	(4)	(5)	(6)	(7)	(8)	(9)	(10)	(11)	(12)	(13)
251[†]	ATCA-ADFS J044644-531752	4:46:44.5	-53:17:53.0	0.00	0.01	1.574	0.042	3.007	0.067	8.9		0.9
252	ATCA-ADFS J044646-531642	4:46:46.3	-53:16:42.7	0.00	0.00	0.334	0.041	0.350	0.041			
253[†]	ATCA-ADFS J044649-530014	4:46:49.4	-53:00:14.7	0.00	0.00	7.702	0.064	14.402	0.115		3.7	-1.7
254	ATCA-ADFS J044650-540754	4:46:50.6	-54:07:54.5	0.03	0.04	1.724	0.244	2.488	0.273			
255	ATCA-ADFS J044650-530916	4:46:50.7	-53:09:16.6	0.01	0.01	0.206	0.033	0.295	0.033			
256	ATCA-ADFS J044652-531923	4:46:52.5	-53:19:23.7	0.00	0.00	0.611	0.042	0.573	0.043			
257	ATCA-ADFS J044653-534837	4:46:53.2	-53:48:37.5	0.02	0.02	0.562	0.061	0.940	0.063		3.3	-41.7
258	ATCA-ADFS J044653-533211	4:46:53.8	-53:32:11.0	0.00	0.00	1.721	0.040	1.897	0.045			
259	ATCA-ADFS J044654-524023	4:46:54.2	-52:40:23.1	0.00	0.00	4.845	0.324	2.529	0.326			
260	ATCA-ADFS J044655-535805	4:46:55.0	-53:58:05.4	0.02	0.02	6.558	0.096	46.427	0.438	14.9	12.3	-48.9
261	ATCA-ADFS J044657-535740	4:46:57.3	-53:57:40.3	0.00	0.00	20.375	0.096	85.243	0.622	10.5	9.1	-45.5
262	ATCA-ADFS J044658-532329	4:46:58.7	-53:23:29.9	0.00	0.00	0.255	0.038	0.304	0.038			
263	ATCA-ADFS J044701-531113	4:47:01.5	-53:11:14.0	0.00	0.00	0.578	0.033	0.658	0.033			
264	ATCA-ADFS J044701-534159	4:47:01.6	-53:41:59.2	0.00	0.00	0.463	0.051	0.769	0.051		2.2	-18.5
265[†]	ATCA-ADFS J044702-533537	4:47:02.4	-53:35:37.7	0.00	0.00	10.258	0.040	19.883	0.139		5.5	-85.8
266	ATCA-ADFS J044703-530411	4:47:03.4	-53:04:11.2	0.00	0.00	0.772	0.037	0.929	0.039			
267	ATCA-ADFS J044703-531503	4:47:03.7	-53:15:03.3	0.00	0.00	0.759	0.033	0.790	0.035			
268[†]	ATCA-ADFS J044704-533541	4:47:04.0	-53:35:41.1	0.00	0.01	9.918	0.040	17.532	0.332	6.9	2.5	-3.3
269	ATCA-ADFS J044706-535434	4:47:06.2	-53:54:34.4	0.00	0.00	1.758	0.197	4.192	0.199	9.3	3.1	7.5
270	ATCA-ADFS J044706-532346	4:47:06.4	-53:23:46.0	0.00	0.01	0.203	0.032	0.275	0.032			
271	ATCA-ADFS J044706-532621	4:47:06.5	-53:26:21.5	0.00	0.00	0.624	0.034	0.686	0.034			
272	ATCA-ADFS J044706-534229	4:47:06.6	-53:42:29.4	0.03	0.02	0.378	0.051	0.649	0.056		3.4	51.7
273	ATCA-ADFS J044706-525312	4:47:06.8	-52:53:12.7	0.00	0.00	10.851	0.125	17.523	0.202	7.3		-8.8
274	ATCA-ADFS J044707-525320	4:47:07.8	-52:53:20.5	0.01	0.01	1.128	0.121	2.849	0.123	9.0	4.4	-37.8
275	ATCA-ADFS J044708-530245	4:47:08.4	-53:02:45.2	0.01	0.02	0.161	0.044	0.328	0.045	6.7	4.1	-12.5
276	ATCA-ADFS J044710-533410	4:47:10.1	-53:34:10.2	0.06	1.27	0.400	0.039	0.230	0.039			
277	ATCA-ADFS J044710-534604	4:47:10.5	-53:46:04.8	0.01	0.01	0.685	0.087	0.798	0.090			
278	ATCA-ADFS J044710-532036	4:47:10.8	-53:20:36.6	0.00	0.00	0.275	0.028	0.294	0.028			
279	ATCA-ADFS J044711-524023	4:47:12.0	-52:40:23.1	0.03	0.03	1.955	0.314	3.973	0.334	8.9		-38.6
280	ATCA-ADFS J044712-530247	4:47:12.0	-53:02:47.7	0.00	0.00	1.288	0.037	1.592	0.038			
281	ATCA-ADFS J044712-530352	4:47:12.8	-53:03:52.9	0.00	0.00	0.459	0.037	0.648	0.037			
282	ATCA-ADFS J044715-525406	4:47:15.2	-52:54:06.4	0.32	0.69	0.261	0.059	2.223	0.070	21.2	10.1	-8.2
283	ATCA-ADFS J044715-531130	4:47:15.9	-53:11:30.4	0.00	0.00	0.251	0.030	0.300	0.030			
284[†]	ATCA-ADFS J044716-525919	4:47:16.0	-52:59:19.8	0.01	0.01	0.295	0.049	0.594	0.050	6.5	4.1	16.5
285	ATCA-ADFS J044716-532643	4:47:16.1	-53:26:43.9	0.00	0.00	0.779	0.032	0.941	0.034			
286[†]	ATCA-ADFS J044716-525935	4:47:16.5	-52:59:35.9	0.01	0.01	0.216	0.049	0.341	0.049		3.2	-75.2
287	ATCA-ADFS J044716-525730	4:47:16.5	-52:57:30.5	0.00	0.00	0.535	0.059	0.665	0.059			
288	ATCA-ADFS J044717-525635	4:47:17.1	-52:56:35.7	0.01	0.02	0.461	0.059	0.757	0.063	7.8		-2.0
289	ATCA-ADFS J044718-531543	4:47:18.8	-53:15:43.1	0.00	0.01	0.194	0.025	0.242	0.025			
290	ATCA-ADFS J044719-533423	4:47:20.0	-53:34:23.0	0.00	0.00	1.080	0.039	1.182	0.041			
291	ATCA-ADFS J044719-525035	4:47:20.0	-52:50:35.8	0.00	0.00	2.818	0.121	4.792	0.135	7.8		-11.2
292	ATCA-ADFS J044720-530829	4:47:20.7	-53:08:29.9	0.00	0.00	1.536	0.037	2.246	0.047			
293	ATCA-ADFS J044723-532141	4:47:23.2	-53:21:41.2	0.00	0.00	0.309	0.028	0.332	0.028			
294	ATCA-ADFS J044723-534824	4:47:23.3	-53:48:24.6	0.11	0.09	0.496	0.069	0.361	0.069			
295	ATCA-ADFS J044724-531411	4:47:24.4	-53:14:11.8	0.00	0.00	0.581	0.028	0.627	0.029			
296	ATCA-ADFS J044725-532855	4:47:25.3	-53:28:55.4	0.01	0.01	0.266	0.032	0.323	0.033			
297	ATCA-ADFS J044725-533406	4:47:25.3	-53:34:06.2	0.00	0.00	0.466	0.039	0.270	0.039			
298	ATCA-ADFS J044726-532554	4:47:26.1	-53:25:54.3	0.01	0.01	0.173	0.032	0.205	0.032			
299	ATCA-ADFS J044726-530030	4:47:26.9	-53:00:30.1	0.04	0.25	0.176	0.040	0.496	0.041	12.7		-13.3
300	ATCA-ADFS J044727-523923	4:47:27.0	-52:39:23.7	0.16	0.12	1.822	0.314	8.875	0.364	13.1	8.9	85.3

Table 13. Continuation of the source catalogue

No	Source name	RA h:m:s.s	DEC d:m:s.s	ΔRA ″	ΔDEC ″	S_{peak} mJy beam^{-1}	ΔS_{peak} mJy beam^{-1}	S_{total} mJy	ΔS_{total} mJy	θ_{maj} ″	θ_{min} ″	PA °
(1)	(2)	(3)	(4)	(5)	(6)	(7)	(8)	(9)	(10)	(11)	(12)	(13)
301	ATCA-ADFS J044727-532626	4:47:27.3	-53:26:26.6	0.00	0.00	0.304	0.032	0.154	0.032			
302	ATCA-ADFS J044728-532955	4:47:28.4	-53:29:55.9	0.01	0.01	0.281	0.034	0.273	0.035			
303	ATCA-ADFS J044730-530654	4:47:30.7	-53:06:54.7	0.10	0.41	0.076	0.025	0.230	0.027	12.6	2.8	4.8
304	ATCA-ADFS J044731-531828	4:47:31.8	-53:18:28.3	0.00	0.00	0.208	0.025	0.224	0.025			
305†	ATCA-ADFS J044731-532018	4:47:31.9	-53:20:18.3	0.00	0.00	0.370	0.028	0.452	0.028			
306†	ATCA-ADFS J044732-532027	4:47:32.5	-53:20:27.3	0.00	0.00	0.454	0.028	0.550	0.029			
307	ATCA-ADFS J044732-530121	4:47:33.0	-53:01:21.9	0.00	0.00	1.015	0.059	1.306	0.060			
308	ATCA-ADFS J044733-531409	4:47:33.5	-53:14:09.4	0.00	0.00	0.223	0.028	0.327	0.028			
309	ATCA-ADFS J044734-530621	4:47:34.0	-53:06:21.8	0.01	0.01	0.139	0.025	0.215	0.025		2.2	25.3
310	ATCA-ADFS J044734-530543	4:47:34.5	-53:05:43.9	0.03	0.03	0.101	0.025	0.133	0.025			
311	ATCA-ADFS J044735-530416	4:47:35.5	-53:04:16.2	0.00	0.01	0.274	0.037	0.351	0.038			
312	ATCA-ADFS J044736-534457	4:47:36.1	-53:44:57.3	0.01	0.01	0.314	0.057	0.457	0.057			
313	ATCA-ADFS J044736-523953	4:47:36.3	-52:39:53.9	0.06	0.06	2.132	0.314	4.857	0.355	9.5	2.6	-40.5
314	ATCA-ADFS J044738-533904	4:47:38.3	-53:39:04.9	0.00	0.02	0.259	0.028	0.259	0.028			
315	ATCA-ADFS J044741-533316	4:47:41.6	-53:33:16.7	0.00	0.00	0.402	0.039	0.473	0.039			
316	ATCA-ADFS J044742-531923	4:47:42.2	-53:19:23.7	0.00	0.00	1.308	0.028	1.344	0.033			
317	ATCA-ADFS J044742-524002	4:47:42.2	-52:40:02.2	0.06	0.12	1.598	0.314	4.906	0.338	11.4	4.5	26.7
318†	ATCA-ADFS J044743-531028	4:47:43.5	-53:10:28.9	0.01	0.03	1.502	0.028	2.907	0.097	9.0		-10.7
319	ATCA-ADFS J044744-530526	4:47:44.1	-53:05:26.5	0.00	0.00	0.268	0.035	0.365	0.035			
320†	ATCA-ADFS J044744-531045	4:47:44.6	-53:10:45.9	0.09	0.06	0.286	0.028	0.864	0.036	10.0	5.8	-51.5
321	ATCA-ADFS J044745-533401	4:47:45.1	-53:34:01.5	0.00	0.00	0.285	0.037	0.322	0.037			
322	ATCA-ADFS J044745-530343	4:47:46.0	-53:03:43.2	0.01	0.02	0.161	0.034	0.286	0.035	6.3	2.6	-12.3
323	ATCA-ADFS J044750-532343	4:47:50.7	-53:23:43.7	0.01	0.00	0.171	0.027	0.224	0.027			
324	ATCA-ADFS J044750-540516	4:47:50.9	-54:05:16.1	0.17	0.09	4.030	0.590	4.886	0.728			
325	ATCA-ADFS J044751-540037	4:47:51.6	-54:00:37.4	0.10	0.07	1.514	0.197	2.510	0.219	9.6		-52.1
326	ATCA-ADFS J044752-530706	4:47:52.1	-53:07:06.3	0.00	0.00	1.970	0.037	2.405	0.038			
327	ATCA-ADFS J044752-533309	4:47:52.9	-53:33:09.8	0.00	0.00	0.762	0.039	0.967	0.039			
328	ATCA-ADFS J044753-534808	4:47:53.3	-53:48:08.9	0.00	0.00	1.142	0.087	1.457	0.087			
329	ATCA-ADFS J044756-532424	4:47:56.5	-53:24:24.4	0.00	0.00	0.279	0.032	0.341	0.032			
330	ATCA-ADFS J044756-531334	4:47:56.8	-53:13:34.6	0.00	0.00	0.167	0.028	0.263	0.028		2.1	18.1
331	ATCA-ADFS J044757-533032	4:47:57.5	-53:30:32.9	0.00	0.00	1.034	0.031	1.243	0.032			
332	ATCA-ADFS J044758-533605	4:47:58.8	-53:36:05.4	0.00	0.00	0.789	0.039	0.983	0.041			
333	ATCA-ADFS J044759-533140	4:47:59.4	-53:31:40.2	0.00	0.00	0.175	0.030	0.184	0.030			
334	ATCA-ADFS J044759-530504	4:47:59.4	-53:05:04.9	0.00	0.00	0.187	0.032	0.217	0.032			
335	ATCA-ADFS J044759-530003	4:47:59.5	-53:00:03.4	0.00	0.00	0.643	0.055	0.328	0.055			
336†	ATCA-ADFS J044802-532611	4:48:02.4	-53:26:11.7	0.03	0.07	0.143	0.029	0.301	0.030	10.1		-6.4
337†	ATCA-ADFS J044802-532617	4:48:02.7	-53:26:17.4	0.02	0.04	0.176	0.029	0.334	0.030	10.8		-39.1
338	ATCA-ADFS J044804-533855	4:48:04.3	-53:38:55.2	0.12	0.34	0.699	0.061	0.421	0.061			
339	ATCA-ADFS J044805-532010	4:48:05.2	-53:20:10.8	0.00	0.00	0.949	0.029	1.082	0.030			
340	ATCA-ADFS J044805-531658	4:48:05.4	-53:16:58.4	0.01	0.03	0.424	0.029	0.856	0.035	10.2		-18.2
341	ATCA-ADFS J044808-532540	4:48:08.3	-53:25:40.4	0.35	2.75	0.266	0.028	0.166	0.028			
342	ATCA-ADFS J044808-531128	4:48:08.4	-53:11:28.9	0.00	0.00	0.820	0.030	0.974	0.032			
343	ATCA-ADFS J044810-532450	4:48:10.9	-53:24:50.7	0.00	0.00	0.475	0.031	0.530	0.031			
344	ATCA-ADFS J044812-531629	4:48:12.1	-53:16:29.1	0.00	0.00	0.705	0.029	0.809	0.031			
345	ATCA-ADFS J044812-531745	4:48:12.2	-53:17:45.2	0.00	0.00	0.471	0.029	0.213	0.029			
346	ATCA-ADFS J044813-531927	4:48:13.8	-53:19:27.2	0.00	0.00	0.191	0.029	0.269	0.029			
347	ATCA-ADFS J044813-533804	4:48:13.9	-53:38:04.3	0.00	0.00	0.374	0.039	0.470	0.039			
348	ATCA-ADFS J044817-530733	4:48:17.5	-53:07:33.1	0.00	0.01	0.316	0.037	0.687	0.037	6.7	5.1	56.0
349	ATCA-ADFS J044818-533753	4:48:18.7	-53:37:53.1	0.00	0.00	0.350	0.039	0.283	0.039			
350	ATCA-ADFS J044820-531012	4:48:20.2	-53:10:12.5	0.00	0.00	0.200	0.028	0.282	0.028			

Table 14. Continuation of the source catalogue

No	Source name	RA h:m:s.s	DEC d:m:s.s	ΔRA ″	ΔDEC ″	S_{peak} mJy beam^{-1}	ΔS_{peak} mJy beam^{-1}	S_{total} mJy	ΔS_{total} mJy	θ_{maj} ″	θ_{min} ″	PA °
(1)	(2)	(3)	(4)	(5)	(6)	(7)	(8)	(9)	(10)	(11)	(12)	(13)
351	ATCA-ADFS J044823-532144	4:48:23.7	-53:21:44.9	0.00	0.00	0.962	0.029	1.088	0.032			
352	ATCA-ADFS J044823-534125	4:48:23.8	-53:41:25.6	0.04	0.04	0.414	0.061	0.670	0.069		2.8	38.4
353	ATCA-ADFS J044824-531440	4:48:24.0	-53:14:40.0	0.00	0.00	0.860	0.030	0.946	0.033			
354	ATCA-ADFS J044826-530138	4:48:26.6	-53:01:38.1	0.00	0.00	0.676	0.037	0.857	0.037			
355	ATCA-ADFS J044827-530547	4:48:27.8	-53:05:47.9	0.00	0.01	0.176	0.035	0.197	0.035			
356	ATCA-ADFS J044828-534600	4:48:28.3	-53:46:00.8	0.01	0.01	0.592	0.061	0.827	0.065			
357	ATCA-ADFS J044828-531924	4:48:28.4	-53:19:25.0	0.00	0.01	0.152	0.029	0.196	0.029			
358	ATCA-ADFS J044830-530157	4:48:30.6	-53:01:57.8	0.00	0.00	0.635	0.037	0.798	0.039			
359	ATCA-ADFS J044831-530730	4:48:31.0	-53:07:30.9	0.02	0.01	0.242	0.034	0.297	0.036			
360	ATCA-ADFS J044831-530801	4:48:31.3	-53:08:02.0	0.01	0.02	0.334	0.037	0.466	0.040			
361	ATCA-ADFS J044832-524111	4:48:32.6	-52:41:11.5	0.00	0.00	145.708	0.478	304.702	1.858	9.6		0.8
362	ATCA-ADFS J044833-524107	4:48:33.5	-52:41:07.7	0.00	0.02	305.631	0.478	625.248	14.080	9.4		6.7
363	ATCA-ADFS J044833-530610	4:48:33.5	-53:06:11.0	0.01	0.01	0.147	0.036	0.230	0.036			
364	ATCA-ADFS J044833-530820	4:48:33.5	-53:08:20.9	0.00	0.00	0.168	0.034	0.237	0.034			
365	ATCA-ADFS J044835-532718	4:48:35.0	-53:27:18.8	0.00	0.00	0.170	0.029	0.229	0.029			
366	ATCA-ADFS J044836-532613	4:48:36.6	-53:26:13.8	0.02	0.04	0.203	0.031	0.317	0.034			
367	ATCA-ADFS J044836-531927	4:48:36.7	-53:19:27.5	0.00	0.00	0.442	0.029	0.528	0.030			
368	ATCA-ADFS J044837-530812	4:48:37.0	-53:08:12.8	0.13	0.33	0.101	0.034	0.370	0.036	14.1	4.2	-19.0
369	ATCA-ADFS J044837-533516	4:48:37.1	-53:35:16.9	0.01	0.02	0.254	0.039	0.461	0.041	7.1		-14.5
370	ATCA-ADFS J044837-533104	4:48:37.2	-53:31:04.2	0.00	0.00	0.212	0.033	0.267	0.033			
371†	ATCA-ADFS J044838-525935	4:48:38.9	-52:59:35.8	0.00	0.00	0.373	0.054	0.414	0.055			
372	ATCA-ADFS J044842-533108	4:48:42.1	-53:31:08.7	0.00	0.00	0.446	0.031	0.530	0.031			
373†	ATCA-ADFS J044842-525927	4:48:42.4	-52:59:27.2	0.18	0.25	0.214	0.054	0.659	0.058	11.2	4.7	-41.8
374	ATCA-ADFS J044842-532346	4:48:42.9	-53:23:46.0	0.00	0.00	0.523	0.029	0.775	0.030	6.3		-2.6
375	ATCA-ADFS J044842-525142	4:48:42.9	-52:51:42.4	0.00	0.01	6.732	0.127	22.240	0.273	15.9		4.2
376	ATCA-ADFS J044842-530008	4:48:42.9	-53:00:08.2	0.01	0.01	1.262	0.059	2.103	0.070		3.1	17.3
377	ATCA-ADFS J044845-532532	4:48:45.1	-53:25:32.6	0.00	0.00	0.246	0.033	0.354	0.033			
378†	ATCA-ADFS J044845-530004	4:48:45.7	-53:00:04.9	0.07	0.07	0.292	0.052	0.831	0.055	9.6	5.5	51.4
379†	ATCA-ADFS J044846-530001	4:48:46.1	-53:00:01.2	0.05	0.06	0.261	0.052	0.778	0.055	9.3	6.0	9.9
380†	ATCA-ADFS J044848-532555	4:48:48.2	-53:25:55.5	0.00	0.00	0.213	0.033	0.278	0.033	6.3		5.2
381	ATCA-ADFS J044848-533317	4:48:48.6	-53:33:17.5	0.00	0.01	0.325	0.043	0.410	0.043			
382	ATCA-ADFS J044848-533317	4:48:48.6	-53:31:09.6	0.00	0.00	0.143	0.048	0.168	0.038			
383	ATCA-ADFS J044852-531641	4:48:52.9	-53:16:41.3	0.00	0.00	0.156	0.030	0.179	0.030			
384	ATCA-ADFS J044853-534031	4:48:53.7	-53:40:31.9	0.01	0.01	0.553	0.078	0.720	0.080			
385	ATCA-ADFS J044854-532141	4:48:54.7	-53:21:41.1	0.00	0.00	0.521	0.034	0.637	0.035			
386	ATCA-ADFS J044855-530133	4:48:55.5	-53:01:33.5	0.01	0.01	0.224	0.051	0.360	0.051	8.6		34.9
387	ATCA-ADFS J044857-530649	4:48:57.8	-53:06:49.8	0.02	0.06	0.204	0.042	0.245	0.045			
388	ATCA-ADFS J044858-531600	4:48:58.0	-53:16:01.0	0.05	0.03	0.124	0.031	0.222	0.032		3.7	-67.9
389	ATCA-ADFS J040490-532535	4:049:0.6	-53:25:35.5	0.00	0.00	5.268	0.038	7.699	0.072			
390	ATCA-ADFS J044901-534111	4:49:01.4	-53:41:11.7	0.00	0.00	0.603	0.078	0.866	0.078			
391	ATCA-ADFS J044903-532723	4:49:03.3	-53:27:23.0	0.03	0.10	0.187	0.035	0.636	0.038	13.5	3.8	17.1
392	ATCA-ADFS J044903-535225	4:49:03.6	-53:52:25.1	0.00	0.00	1.553	0.160	1.472	0.160			
393	ATCA-ADFS J044905-531733	4:49:05.6	-53:17:33.0	0.00	0.00	0.427	0.034	0.477	0.034			
394	ATCA-ADFS J044905-525234	4:49:06.0	-52:52:34.8	0.01	0.04	1.097	0.179	2.782	0.184	12.1		-18.5
395	ATCA-ADFS J044906-525247	4:49:06.0	-52:52:47.1	0.00	0.01	2.099	0.179	4.169	0.186	7.9		2.0
396	ATCA-ADFS J044906-531643	4:49:06.4	-53:16:43.8	0.00	0.00	0.219	0.034	0.285	0.034			
397	ATCA-ADFS J044910-534052	4:49:10.9	-53:40:52.0	0.00	0.00	1.538	0.078	3.720	0.089	8.6	4.4	-37.9
398	ATCA-ADFS J044913-530936	4:49:13.2	-53:09:36.5	0.00	0.01	0.521	0.035	0.976	0.037	7.0	2.4	14.5
399	ATCA-ADFS J044913-524926	4:49:13.3	-52:49:26.6	0.00	0.02	1.400	0.179	3.291	0.188	11.4		12.2
400	ATCA-ADFS J044914-530221	4:49:14.3	-53:02:21.6	0.02	0.01	3.942	0.046	12.607	0.201	11.6	5.4	74.7

Table 15. Continuation of the source catalogue

No	Source name	RA h:m:s.s	DEC d:m:s.s	ΔRA ″	ΔDEC ″	S_{peak} mJy beam^{-1}	ΔS_{peak} mJy beam^{-1}	S_{total} mJy	ΔS_{total} mJy	θ_{maj} ″	θ_{min} ″	PA °
(1)	(2)	(3)	(4)	(5)	(6)	(7)	(8)	(9)	(10)	(11)	(12)	(13)
401	ATCA-ADFS J044914-530716	4:49:14.7	-53:07:16.9	0.00	0.00	0.560	0.046	0.710	0.047			
402	ATCA-ADFS J044917-532530	4:49:17.4	-53:25:30.5	0.00	0.00	0.215	0.034	0.247	0.034			
403	ATCA-ADFS J044920-531748	4:49:20.2	-53:17:48.7	0.04	0.06	0.123	0.029	0.263	0.031	7.7	3.4	-18.5
404	ATCA-ADFS J044921-524710	4:49:21.0	-52:47:10.6	0.00	0.00	1.517	0.179	1.646	0.179			
405	ATCA-ADFS J044921-531144	4:49:21.1	-53:11:44.6	0.01	0.01	0.178	0.039	0.257	0.039	6.7		-12.8
406	ATCA-ADFS J044922-532122	4:49:22.3	-53:21:22.4	0.01	0.01	0.545	0.034	0.234	0.034			
407	ATCA-ADFS J044922-532500	4:49:22.7	-53:25:00.3	0.00	0.00	0.208	0.033	0.266	0.033			
408	ATCA-ADFS J044923-532431	4:49:23.1	-53:24:31.0	0.04	0.06	0.116	0.033	0.224	0.034	9.1		-34.0
409	ATCA-ADFS J044924-531127	4:49:24.3	-53:11:27.4	0.00	0.00	0.412	0.035	0.578	0.036			
410†	ATCA-ADFS J044928-532600	4:49:28.3	-53:26:00.0	0.08	0.09	0.146	0.036	0.301	0.038	6.3	5.0	-67.9
411†	ATCA-ADFS J044928-532610	4:49:28.7	-53:26:10.1	0.00	0.00	0.215	0.036	0.271	0.036			
412	ATCA-ADFS J044928-532045	4:49:28.8	-53:20:45.6	0.00	0.00	0.349	0.034	0.433	0.034			
413	ATCA-ADFS J044929-530814	4:49:29.7	-53:08:14.0	0.06	0.09	0.179	0.044	0.576	0.045	11.7	4.9	37.9
414	ATCA-ADFS J044930-531646	4:49:30.6	-53:16:46.8	0.00	0.00	0.546	0.034	0.705	0.034			
415	ATCA-ADFS J044931-532335	4:49:31.5	-53:23:35.3	0.00	0.00	0.347	0.034	0.417	0.034			
416	ATCA-ADFS J044932-533156	4:49:32.8	-53:31:56.9	0.06	0.02	0.229	0.046	0.461	0.049	8.4	3.2	81.3
417	ATCA-ADFS J044933-525830	4:49:33.5	-52:58:30.1	0.01	0.01	0.511	0.074	0.903	0.077	7.2		9.2
418	ATCA-ADFS J044935-524810	4:49:35.6	-52:48:10.2	0.00	0.00	2.011	0.179	2.896	0.181	6.4		13.0
419	ATCA-ADFS J044939-533420	4:49:39.3	-53:34:20.2	0.00	0.00	0.309	0.055	0.409	0.055			
420	ATCA-ADFS J044944-532145	4:49:44.6	-53:21:45.7	1.26	1.86	0.500	0.046	0.320	0.046			
421	ATCA-ADFS J044947-530555	4:49:47.9	-53:05:55.7	0.00	0.00	0.379	0.058	0.617	0.058		3.6	76.4
422	ATCA-ADFS J044950-532540	4:49:51.0	-53:25:40.2	0.01	0.01	0.234	0.045	0.347	0.046			
423	ATCA-ADFS J044951-530621	4:49:51.3	-53:06:21.2	0.00	0.00	0.545	0.066	0.764	0.066			
424	ATCA-ADFS J044952-534449	4:49:52.2	-53:44:49.8	0.00	0.01	1.030	0.112	1.697	0.114	7.8		-23.0
425†	ATCA-ADFS J044952-531205	4:49:52.4	-53:12:05.6	0.00	0.00	0.831	0.054	0.369	0.054			
426	ATCA-ADFS J044952-533619	4:49:52.7	-53:36:19.2	0.00	8.84	0.491	0.069	0.370	0.069			
427	ATCA-ADFS J044953-525737	4:49:53.8	-52:57:38.0	0.00	0.00	3.114	0.106	4.553	0.112			
428†	ATCA-ADFS J044955-531159	4:49:55.0	-53:11:59.4	0.00	0.00	0.339	0.049	0.485	0.049			
429	ATCA-ADFS J044956-532432	4:49:56.7	-53:24:32.4	0.12	0.12	0.525	0.050	3.381	0.070	13.1	12.6	62.9
430	ATCA-ADFS J044956-532430	4:49:56.7	-53:24:30.1	0.01	0.12	0.375	0.050	5.870	0.056	30.8	14.2	-49.7
431	ATCA-ADFS J044958-531509	4:49:58.4	-53:15:09.6	0.09	0.02	0.206	0.049	0.509	0.051	10.9	3.4	79.6
432	ATCA-ADFS J045005-533411	4:50:05.4	-53:34:11.0	0.00	0.00	2.742	0.067	4.189	0.075			
433	ATCA-ADFS J045011-531753	4:50:11.4	-53:17:53.7	0.00	0.00	0.859	0.046	1.160	0.047			
434†	ATCA-ADFS J045013-532517	4:50:13.9	-53:25:17.1	0.03	0.09	0.659	0.050	3.225	0.073	15.0	7.1	4.1
435	ATCA-ADFS J045014-531207	4:50:14.3	-53:12:07.0	0.00	0.00	0.379	0.050	0.438	0.050			
43†6	ATCA-ADFS J045015-532459	4:50:15.6	-53:24:59.9	0.01	0.03	0.860	0.050	3.274	0.067	13.0	5.6	15.8
437	ATCA-ADFS J045016-531549	4:50:16.1	-53:15:49.3	0.00	0.00	1.638	0.050	2.503	0.056			
438	ATCA-ADFS J045016-532748	4:50:16.2	-53:27:48.3	0.00	0.00	0.972	0.050	2.177	0.055	9.0	3.6	-65.9
439	ATCA-ADFS J045024-525706	4:50:24.6	-52:57:06.6	0.09	0.30	0.559	0.106	3.073	0.125	16.0	7.8	13.8
440	ATCA-ADFS J045024-534620	4:50:24.7	-53:46:20.4	0.01	0.01	2.627	0.254	9.443	0.272	10.7	7.1	-33.8
441	ATCA-ADFS J045025-524653	4:50:25.1	-52:46:53.0	0.83	0.30	0.930	0.212	6.239	0.257	16.7	10.2	-47.4
442	ATCA-ADFS J045025-524630	4:50:25.7	-52:46:30.4	0.01	0.03	1.705	0.212	2.204	0.215			
443	ATCA-ADFS J045026-534552	4:50:26.6	-53:45:52.4	0.02	0.01	0.702	0.112	1.105	0.117	6.5		-59.1
444	ATCA-ADFS J045027-535220	4:50:27.2	-53:52:20.5	0.01	0.02	2.002	0.254	2.206	0.265			
445	ATCA-ADFS J045028-531005	4:50:28.1	-53:10:05.2	0.00	0.00	1.071	0.089	1.485	0.091			
446	ATCA-ADFS J045029-534648	4:50:29.0	-53:46:48.1	0.00	0.00	23.575	0.519	45.099	0.628	8.4		-27.9
447	ATCA-ADFS J045032-531844	4:50:32.8	-53:18:45.0	0.00	0.00	8.557	0.079	13.048	0.108			
448	ATCA-ADFS J045048-534600	4:50:48.9	-53:46:00.0	0.00	0.00	13.588	0.519	26.833	0.545	8.5		-35.9
449	ATCA-ADFS J045049-524627	4:50:49.8	-52:46:27.9	0.03	0.13	2.529	0.418	5.703	0.460	9.8		9.4
450	ATCA-ADFS J045051-531455	4:50:51.1	-53:14:55.4	0.00	0.00	0.519	0.086	0.867	0.087		3.9	-71.9

Table 16. Continuation of the source catalogue

No	Source name	RA h:m:s.s	DEC d:m:s.s	ΔRA ″	ΔDEC ″	S_{peak} mJy beam^{-1}	ΔS_{peak} mJy beam^{-1}	S_{total} mJy	ΔS_{total} mJy	θ_{maj} ″	θ_{min} ″	PA °
(1)	(2)	(3)	(4)	(5)	(6)	(7)	(8)	(9)	(10)	(11)	(12)	(13)
451	ATCA-ADFS J045052-531120	4:50:52.7	-53:11:20.5	0.01	0.01	0.566	0.086	0.820	0.086			
452	ATCA-ADFS J045055-531247	4:50:55.6	-53:12:47.5	0.00	0.00	0.823	0.104	0.578	0.104			
453	ATCA-ADFS J045102-524726	4:51:02.5	-52:47:26.6	0.00	0.00	3.847	0.418	2.931	0.420			
454	ATCA-ADFS J045105-524135	4:51:05.6	-52:41:35.2	1.03	2.02	11.977	1.313	12.258	1.329			
455	ATCA-ADFS J045105-524011	4:51:05.8	-52:40:11.7	0.00	0.00	12.550	1.313	10.169	1.327			
456	ATCA-ADFS J045107-535122	4:51:07.5	-53:51:22.1	0.03	0.02	3.763	0.519	5.997	0.570		3.0	-66.1
457	ATCA-ADFS J045108-524056	4:51:08.2	-52:40:56.1	0.01	0.02	9.444	1.313	14.216	1.359	8.5		8.2
458	ATCA-ADFS J045111-531005	4:51:11.7	-53:10:05.0	0.00	0.00	27.098	0.089	51.014	0.301		4.3	68.1
459	ATCA-ADFS J045112-525420	4:51:12.5	-52:54:20.8	0.05	0.19	1.005	0.185	4.226	0.216	14.4	5.7	5.2
460	ATCA-ADFS J045112-530950	4:51:12.8	-53:09:50.4	0.01	0.02	0.580	0.089	0.906	0.093	6.5		-28.2
461	ATCA-ADFS J045113-524901	4:51:13.5	-52:49:01.6	0.09	0.22	2.282	0.418	8.169	0.505	13.1	4.7	-1.8
462	ATCA-ADFS J045114-535300	4:51:14.6	-53:53:00.2	0.00	0.00	8.905	0.519	4.259	0.531			
463	ATCA-ADFS J045115-525405	4:51:15.1	-52:54:05.1	0.10	0.04	1.235	0.185	2.346	0.219	6.8	4.0	-87.7
464	ATCA-ADFS J045115-535313	4:51:15.7	-53:53:13.4	0.23	0.26	8.194	0.519	4.318	0.520			
465	ATCA-ADFS J045116-535237	4:51:16.4	-53:52:37.1	2.77	0.15	3.641	0.519	7.347	0.673	9.1	2.7	-86.2
466	ATCA-ADFS J045117-534428	4:51:17.3	-53:44:28.2	0.02	0.01	1.370	0.205	1.558	0.213			
467	ATCA-ADFS J045118-524727	4:51:18.2	-52:47:27.1	0.03	0.02	7.084	1.169	17.688	1.225	9.7	3.9	48.2
468	ATCA-ADFS J045118-535307	4:51:18.6	-53:53:07.8	0.01	0.01	8.692	0.519	9.380	0.536			
469	ATCA-ADFS J045119-535211	4:51:19.5	-53:52:11.2	0.05	0.38	3.267	0.519	7.113	0.640	12.6		-7.6
470	ATCA-ADFS J045128-532220	4:51:28.7	-53:22:20.5	0.03	0.03	3.748	0.168	13.261	0.322	8.8	8.6	82.4
471	ATCA-ADFS J045136-524710	4:51:36.6	-52:47:10.4	0.00	0.00	6.921	1.169	23.498	1.434	12.0	5.8	89.0
472	ATCA-ADFS J045138-524650	4:51:39.0	-52:46:50.6	0.01	0.01	9.279	1.169	13.088	1.207			
473	ATCA-ADFS J045149-524645	4:51:49.2	-52:46:45.4	0.25	2.63	6.273	1.169	26.447	1.436	17.0	3.8	13.4
474	ATCA-ADFS J045149-530138	4:51:49.8	-53:01:38.8	0.05	0.12	2.542	0.283	8.676	0.353	11.4	5.7	2.2
475	ATCA-ADFS J045149-524827	4:51:49.8	-52:48:27.4	0.17	0.26	5.931	1.169	17.767	1.439	10.6	4.8	26.3
476	ATCA-ADFS J045149-524617	4:51:49.9	-52:46:17.8	1.33	0.12	6.887	1.169	27.034	1.273	13.0	6.7	85.5
477	ATCA-ADFS J045150-524635	4:51:50.5	-52:46:35.7	0.00	0.00	17.132	1.169	8.993	1.181			
478	ATCA-ADFS J045150-525038	4:51:50.5	-52:50:38.3	0.11	0.36	5.820	1.169	16.062	1.370	13.0		4.6
479	ATCA-ADFS J045151-524633	4:51:51.5	-52:46:33.1	0.04	0.01	8.867	1.169	10.264	1.179			
480	ATCA-ADFS J045151-524724	4:51:51.6	-52:47:24.1	0.00	0.00	11.761	1.169	14.152	1.195			
481	ATCA-ADFS J045151-524646	4:51:51.7	-52:46:46.7	0.03	0.26	8.903	1.169	15.664	1.458	10.2		-6.6
482	ATCA-ADFS J045151-532021	4:51:51.7	-53:20:21.4	0.01	0.01	1.850	0.168	3.386	0.177	6.6	3.4	-63.1
483	ATCA-ADFS J045151-524842	4:51:51.7	-52:48:42.4	0.04	0.10	7.938	1.169	25.015	1.386	11.9	4.1	5.2
484	ATCA-ADFS J045151-525438	4:51:51.9	-52:54:38.7	0.01	0.00	4.121	0.485	4.216	0.486			
485	ATCA-ADFS J045152-525502	4:51:52.5	-52:55:02.5	0.29	0.19	2.875	0.485	12.804	0.601	12.2	8.3	14.2
486	ATCA-ADFS J045154-524724	4:51:54.9	-52:47:24.4	0.14	0.65	9.557	1.169	16.203	1.417	9.7		-24.5
487	ATCA-ADFS J045155-530311	4:51:55.2	-53:03:11.5	0.08	0.03	2.268	0.283	5.249	0.348	8.7	4.1	67.5
488	ATCA-ADFS J045156-534525	4:51:56.6	-53:45:25.5	0.05	0.03	3.238	0.512	6.335	0.557		5.0	-78.6
489	ATCA-ADFS J045156-525400	4:51:56.9	-52:54:00.7	0.08	0.28	3.240	0.485	8.096	0.629	11.2		-1.7
490	ATCA-ADFS J045158-534542	4:51:58.5	-53:45:42.8	1.98	1.28	2.648	0.512	9.577	0.777	13.8	5.1	62.5
491	ATCA-ADFS J045159-524900	4:51:59.1	-52:49:00.2	0.00	0.00	10.178	1.169	14.682	1.170			
492	ATCA-ADFS J045159-525648	4:51:59.8	-52:56:48.3	0.04	0.40	2.870	0.485	10.141	0.596	17.8		-4.5
493	ATCA-ADFS J045159-525543	4:51:59.9	-52:55:43.6	0.01	0.01	3.313	0.485	4.881	0.506		2.2	58.6
494	ATCA-ADFS J040520-524812	4:052:0.1	-52:48:12.9	0.06	0.13	7.704	1.169	18.748	1.324	11.0		24.1
495	ATCA-ADFS J040520-531317	4:052:0.3	-53:13:17.5	0.12	0.03	1.227	0.199	2.815	0.219	11.1	2.3	74.3
496	ATCA-ADFS J040520-533002	4:052:0.6	-53:30:02.9	0.02	0.02	1.322	0.194	2.057	0.204			
497	ATCA-ADFS J040520-530852	4:052:0.6	-53:08:52.2	0.00	0.00	2.270	0.199	1.585	0.199			
498	ATCA-ADFS J040520-524942	4:052:0.7	-52:49:43.0	0.01	0.04	8.448	1.169	12.124	1.244	6.6		-2.9
499	ATCA-ADFS J040520-525530	4:052:0.9	-52:55:30.7	0.01	0.02	3.826	0.485	5.604	0.491			
500	ATCA-ADFS J045201-524832	4:52:01.8	-52:48:32.6	0.19	0.24	6.804	1.169	13.808	1.309	8.8		35.2

Table 17. Continuation of the source catalogue

No	Source name	RA h:m:s.s	DEC d:m:s.s	ΔRA ″	ΔDEC ″	S_{peak} mJy beam^{-1}	ΔS_{peak} mJy beam^{-1}	S_{total} mJy	ΔS_{total} mJy	θ_{maj} ″	θ_{min} ″	PA °
(1)	(2)	(3)	(4)	(5)	(6)	(7)	(8)	(9)	(10)	(11)	(12)	(13)
501	ATCA-ADFS J045202-524914	4:52:02.2	-52:49:14.8	0.02	0.03	7.654	1.169	18.004	1.257	7.2	5.4	3.1
502	ATCA-ADFS J045203-525035	4:52:03.1	-52:50:35.2	0.00	0.00	15.911	1.169	9.492	1.184			
503	ATCA-ADFS J045203-525347	4:52:03.2	-52:53:47.6	0.04	0.10	3.673	0.485	5.336	0.556	7.8		22.8
504	ATCA-ADFS J045203-525647	4:52:03.7	-52:56:47.0	0.01	0.02	3.972	0.485	4.655	0.504			
505	ATCA-ADFS J045203-525429	4:52:03.9	-52:54:29.1	0.32	0.46	14.003	0.485	6.400	0.525			
506	ATCA-ADFS J045203-524959	4:52:04.0	-52:49:59.9	0.00	0.00	14.626	1.169	19.753	1.254	18.4		-0.1
507	ATCA-ADFS J045204-534456	4:52:04.4	-53:44:56.3	0.00	0.00	6.034	0.512	4.865	0.523			
508	ATCA-ADFS J045204-533750	4:52:04.7	-53:37:50.4	0.00	0.00	2.550	0.264	2.467	0.264			
509	ATCA-ADFS J045205-525442	4:52:05.3	-52:54:42.0	0.05	0.04	3.959	0.485	5.402	0.572	6.8		48.9
510	ATCA-ADFS J045205-525422	4:52:05.4	-52:54:22.2	0.41	0.03	2.996	0.485	9.247	0.515	11.0	5.5	-77.8
511	ATCA-ADFS J045205-530208	4:52:05.8	-53:02:09.0	0.00	0.00	2.563	0.283	1.913	0.289			
512	ATCA-ADFS J045205-534448	4:52:05.9	-53:44:48.4	0.01	0.04	3.722	0.512	6.822	0.535	11.3		9.2
513	ATCA-ADFS J045205-533724	4:52:05.9	-53:37:24.5	0.12	0.41	1.728	0.264	3.676	0.308	13.6		-21.9
514	ATCA-ADFS J045206-534418	4:52:06.7	-53:44:18.2	0.04	0.03	4.627	0.512	8.802	0.539	8.2		37.8
515	ATCA-ADFS J045206-534449	4:52:06.8	-53:44:49.5	0.01	0.16	3.419	0.512	5.640	0.549	11.6		3.9
516	ATCA-ADFS J045206-533804	4:52:07.0	-53:38:04.0	0.00	0.00	3.112	0.264	1.544	0.267			
517	ATCA-ADFS J045207-532938	4:52:07.3	-53:29:38.5	0.39	0.03	1.101	0.194	2.354	0.223	12.0		-88.5
518	ATCA-ADFS J045207-531730	4:52:07.5	-53:17:30.1	0.00	0.00	5.073	0.168	18.320	0.209	10.7	7.2	-57.9
519	ATCA-ADFS J045208-534433	4:52:08.3	-53:44:33.3	0.09	0.51	3.130	0.512	9.209	0.654	13.8		-19.0
520	ATCA-ADFS J045208-531740	4:52:08.5	-53:17:41.0	0.02	0.01	3.071	0.579	10.839	0.593	10.4	7.3	-87.1
521	ATCA-ADFS J045208-533736	4:52:08.6	-53:37:36.8	0.03	0.02	1.982	0.264	3.515	0.274	7.8		38.9
522	ATCA-ADFS J045209-534512	4:52:09.4	-53:45:12.3	2.19	4.54	7.233	0.512	4.924	0.540			
523	ATCA-ADFS J045209-534441	4:52:09.5	-53:44:41.9	0.66	1.02	3.376	0.512	9.260	0.705	15.2		35.0
524	ATCA-ADFS J045227-530208	4:52:27.4	-53:02:08.5	0.03	0.06	5.782	0.916	10.416	0.996	7.2		-17.6
525	ATCA-ADFS J045227-534005	4:52:27.8	-53:40:05.5	0.05	0.06	11.733	1.362	37.255	1.712	10.5	5.8	-38.8
526	ATCA-ADFS J045229-525651	4:52:29.8	-52:56:51.2	0.10	0.07	8.503	1.502	18.082	1.666	7.7	4.0	57.5
527	ATCA-ADFS J045232-530216	4:52:32.4	-53:02:16.4	0.02	0.01	7.840	0.916	9.879	0.941			
528	ATCA-ADFS J045236-530120	4:52:36.7	-53:01:20.2	0.00	0.00	9.904	0.916	11.882	0.920			
529	ATCA-ADFS J045239-530219	4:52:39.0	-53:02:19.5	0.20	0.07	6.015	0.916	8.138	1.123	6.3		75.7
530	ATCA-ADFS J045240-531548	4:52:40.6	-53:15:48.7	0.02	0.02	5.478	0.672	18.272	0.761	9.7	7.0	39.5